Obtaining potential energy surfaces of an der waals molecules

Howson, Joanna M. M.

Obtaining potential energy surfaces of Van der Waals molecules.

Joanna M. M. Howson

Ph.D Thesis

Chemistry Department

University of Durham

October 1999

Abstract of Ph.D Thesis

'Obtaining potential energy surfaces of Van der Waals molecules.'

Joanna M. M. Howson, University of Durham, 1999

Two different methods were used to obtain a potential energy surface for the ArCO molecule. One involved choosing a functional form for the repulsion and dispersion energies whose parameters were determined by a fit to experimental data. A physically justified potential that agreed with experiment could not be obtained. The other method was based on calculating *ab initio* interaction energies at different configurations of the molecule and interpolating between them. The resulting surface was scaled in the energy and the co-ordinates. Improved agreement was achieved for most observed bound states. Errors in the surface may have been due to an inadequate density of *ab initio* energies. So, how the molecular configurations chosen for interaction energy calculations affected the potential obtained was investigated. Both the co-ordinate system and the interpolation scheme also significantly affected the quality of surface obtained. The best compromise between accuracy and number of configurations, was points distributed on a regular grid in elliptic co-ordinates with Gauss-Legendre quadrature points in the angular co-ordinate. This information was employed to obtain a potential energy surface for the weakly bound HeOCS molecule which was in close agreement with experiment. A co-ordinate and energy scaling, guided by experiment, was applied to the *ab initio* surface. Only three scaling parameters were required due to the high quality of the initial surface.

Vater

Acknowledgments

I would like to thank my supervisor, Prof. Jeremy Hutson, for his guidance over the last three years. I would also like to thank the EPSRC for funding and BP for a Graduate Scholarship.

There are a number of other people to whom I owe a debt of gratitude, the Hutson group for providing an interesting environment in which to work; Dr Lydia Heck for invaluable assistance with all matters computational.

I am also exceedingly grateful to Dr Nicholas Wright who's support, encouragement and scientific discussions have been outstanding over the past three years.

My parents support has been invaluable to me and is lovingly acknowledged.

Finally I should like to say 'thankyou' to all my teammates at DCWRFC for keeping me sane.

Statement

No part of this thesis has been previously submitted by me for a degree to any university. Every effort has been made to ensure that all work which is not original to the author has been properly credited. I place no restriction upon access to, or copying of, this thesis.

CONTENTS

CHAPTER

1

Introduction

Since they were first observed, Van der Waals molecules have been recognized as a tool to aid in the study of intermolecular forces. These molecules consist of two or more chemically stable species, are loosely bound and often exhibit large amplitude motion. Much work therefore has been done on modeling the interaction potentials of Van der Waals molecules [1,2].

Intermolecular forces are of interest as they have a role to play in many areas of science [3]. A few examples are phase behaviour, reaction kinetics, atmospheric chemistry and crystal structures. An ultimate goal in the study of intermolecular forces must be to accurately model molecules in the bulk. Calculations are possible on large clusters that find, for example, the minimum energy configurations using methods such as simulated annealing. Experiments have been performed which involve putting molecules in or on the surface of liquid helium droplets that consist of more than 10^3 helium atoms. The rotational constants of molecules placed in these droplets are reduced for a reason which is not fully understood and therefore models of the 'bulk' processes are

needed.

In this thesis, the systems considered consist of a rare gas atom with a linear molecule. As well as being of interest in their own right, the systems serve as prototypes to test and develop methods of obtaining potential energy surfaces. The study of small molecules can aid the development of models for bigger systems such as the helium droplet case; the potentials can be used to rationalise the changes in behaviour observed in the droplets [4].

In the present work potentials of spectroscopic accuracy are sought. To simplify the problem the linear molecule is not allowed to vibrate. This approximation is appropriate because monomer vibration is a lot faster than Van der Waals motions. The potential obtained is therefore only dependent on a distance and an angle. If the linear molecule were allowed to vibrate, the potential surface would be a function of many co-ordinates which would increase the complexity of the problem.

1.1 Experimental methods

Measurement of deviations from perfect gas behaviour, transport properties [5] and scattering data [6,7] can all be used to assess the quality of a potential energy surface. High resolution spectroscopy of Van der Waals molecules [8,9] perhaps gives the most useful information, and so are frequently used to aid in the construction as well as assess the quality of a potential [1].

1.1.1 Gas imperfections

The earliest of the experiments mentioned above, the measurement of gas imperfections, were performed in the bulk. The deviation from perfect gas behaviour can be represented by the virial expansion,

$$\frac{pV}{RT} = 1 + \frac{B(T)}{V} + \frac{C(T)}{V^2} + \cdots, \tag{1.1}$$

where p is pressure, V is the molar volume, T is temperature, $B(T)$ is the second and $C(T)$ the third virial coefficients. The expansion has been truncated at the third term. The coefficients are measured at a number of different temperatures. Normally the second virial coefficient, which can be directly related to

the intermolecular potential [10], is measured. For instance the second virial coefficient for a diatomic molecule interacting with a rare gas atom is,

$$B(T) = \pi N_A \int_0^\infty \int_0^\pi [1 - \exp(-V/kT)] \sin\theta \, d\theta R^2 \, dR. \tag{1.2}$$

N_A is Avogadros constant, $V = V(R, \theta)$ is the intermolecular potential energy surface and k is Boltzmanns constant. The second virial coefficients of many rare gas-linear molecule dimers have been measured e.g. Rg/O_2, Rg/N_2, Rg/CO, Rg/CO_2 mixtures [11, 12]. By themselves, virial coefficients are insufficient to determine a potential as they only give angle-averaged information. If however information on the potential anisotropy is available they do serve as a test of the well depth. Second virial coefficients have also been combined with scattering data to test and develop potentials [13]

Details of experimental methods can be found in Refs. [5, 12].

1.1.2 Transport properties

Transportation of momentum (viscosity), of energy (thermal conductivity) and of particles (diffusion) are considered here. Each transport coefficient is expressed in terms of a collision integral that is temperature dependent but averaged. Like virial coefficients, transport properties are measured in the bulk and mostly give information on the angle-averaged potential surface, principally on the repulsive wall. Although they do not serve as a sensitive probe of a potential [14, 15] they can be used in conjunction with other experimental data to test a potential [16–19].

An account of experimental methods used to measure transport property coefficients can be found in Ref [5].

1.1.3 Molecular scattering

Many systems have been studied using scattering techniques and the information used to test or modify potential energy surfaces [20–23]. In contrast to transport properties and second virial coefficients, scattering data can give information on the potential anisotropy.

Consider a two particle collision. At long range the attractive forces dominate the interaction. As the distance between the particles is reduced the repulsive forces begin to have an effect and at some point cause the particles to move apart again. The encounter may be elastic (the particles do not exchange energy) or inelastic (they do exchange energy). Alternatively a reaction may take place in which the scattered particles are chemically different to the pre-scattered particles. Although a number of reactions have been studied using scattering techniques [24–27] the focus of this discussion are elastic and inelastic collisions.

In practice single collisions cannot be measured easily, so many scattering events are recorded at the same time. The most common experiment is crossed molecular beam scattering. The ratio of the number of scattered particles at a given scattering angle (per unit time) to the number of incident particles (per unit time per unit area) is known as the differential cross section. Integral cross sections are reported occasionally in which case the scattered species are detected at all angles. These cross sections can be used to test or modify potentials.

Elastic scattering gives information predominantly on isotropic interactions. Atom-atom interaction potentials are obtained from scattering data by inversion of well resolved cross sections [28,29]. Differential and integral cross sections have been used in combination with viscosity measurements to obtain rare gas dimer potential curves [30]. The viscosity coefficients gave information on the repulsive wall region while the low energy differential cross sections gave information on the lower repulsive and attractive regions. The resulting potentials were thought to be better in the repulsive wall region than previous potentials.

Large-angle scattering is dominated by repulsion. Attractive forces have a greater role to play in small-angle scattering. So integral cross sections and small-angle differential cross sections can be used to give information on the long range part of the potential. For Ar and He interacting with NO, CO, CO_2 and N_2, large-angle differential cross sections have been employed to assess *ab initio* and empirical potential energy surfaces [31]. It was found that the *ab initio* potentials were subject to systematic errors on the repulsive wall. However

this is not too surprising as the potentials were extrapolated out in this region.

Quantum effects are observed in scattering experiments. In atom-atom scattering, rainbow structure gives the well depth. However in atom-molecule scattering the rainbow structure is damped. This damping is sensitive to the anisotropy of the well depth [32]. Calculation of the damping of the rainbow structure can serve as a test of the anisotropy of a potential [20, 33]. An analogous effect is seen with diffraction oscillations. In atom-atom scattering diffraction oscillations give the position of the potential well, while in atom-molecule collisions the diffraction structure is damped giving information on the anisotropy of the well position [32]. Again this information serves as a useful test of a potential [15]. Glory oscillations in total integral cross sections also give information on the attractive potential but are difficult to measure and so are rarely reported.

Inelastic scattering experiments are thought to provide the most detailed information on the potential anisotropy of all the experimental data discussed so far [34]. Vibrationally inelastic scattering data can make a useful test of a potential that includes monomer vibration. However only rigid rotor potentials are considered in this work making rotationally inelastic scattering data more useful. Information on the potential anisotropy can be obtained from rotationally inelastic cross sections. Combining this with diffraction oscillations in the total differential cross sections serve as a fair test of a potential surface in the repulsive region. Beneventi *et al.* used this combination of data to show that their He–CO_2 potential was superior to an earlier one [14]. They found the anisotropy of their $HeCO_2$ potential in the repulsive region estimated from damped diffraction oscillations was in agreement with the anisotropy obtained from inelastic scattering data [14]. No inelastic integral cross sections were available, so no assessment was made of the attractive region. Later, Weida *et al.* tested the potential against their high resolution spectra for $HeCO_2$ [35] which was sensitive to the attractive region. They found the potential to be too isotropic around the minimum.

Helium-molecule systems are loosely bound so it was thought that the spectra of such systems was difficult and therefore unlikely to be measured [36]. Hence scattering data was a valuable source of information. Much work

has been done on He scattering off small molecules which provided useful information on the interaction potential [14,36–38].

Experiments with molecular hydrogen scattering off small molecules have also been performed and the information used to test semi-empirical potential surfaces for these systems [22,23]. Metal atom scattering off gases have also been studied [39] although systems with much larger scattering partners are more difficult to study.

An account of the experimental techniques used for scattering studies can be found in Refs. [40,41] and a good introductory text concerning the theory of collisions can be found in Ref [42].

A significant problem with scattering data other than atom-atom scattering is the lack of a direct relation between the data and the potential energy surface. This means that scattering data is not easily incorporated in a least squares fitting routine. So if a surface is to be modified using scattering data a trial and error procedure tends to be adopted.

1.1.4 Spectroscopy of Van der Waals complexes

The spectroscopy of Van der Waals molecules give detailed information on the anisotropy of the forces between the constituent monomers [8,9]. Unlike the bulk gas properties and the scattering data where there is a complex dependence on the potential, spectroscopic constants can be related directly to the interaction potential. Spectroscopic data are easily incorporated into a least squares potential fit which is more desirable than the trial and error methods usually used to invert scattering data.

Just a few bound states are required to characterise the potential surface of a loosely bound system. Rotational constants give information on the moment of inertia and can be measured in either the microwave or the infrared region. Excitations of Van der Waals and monomer vibrations and their rotational constants are also measured in the infra-red and give information on both the radial and angular dependence of the potential surface in the well region.

Spectroscopic data thus give more detailed information on the potential

well region than any of the experiments discussed above and is a good aid in developing a potential. Surfaces that are in close agreement with spectroscopy will often reproduce transport property and virial coefficient data even if this data is not used in the fitting procedure. For example, spectroscopic data and second virial coefficients were used in a least squares fit of a systematic potential form to obtain two empirical potentials for $ArCO_2$ by Hutson *et al.* [43]. In a later paper the group tested the potential against pressure broadening data, transport and relaxation cross sections. The properties calculated with the potentials gave reasonable agreement with experiment [44].

Spectroscopic data are often used to test *ab initio* potentials as they are a sensitive probe of the well region. For example, a SAPT potential energy surface was recently obtained for $ArCH_4$ [45]. Rotationally inelastic integral cross sections and total differential cross sections were calculated from this potential [45, 46]. Good agreement with experiment was obtained for both cross sections. Yet, the near infrared spectrum calculated with the potential was not in quantitative agreement with experiment [47, 48]. This illustrates the quality of the spectroscopic data, although cross sections were reproduced the spectroscopy was not, highlighting inaccuracies in the potential well.

One disadvantage of spectroscopy is that it only gives information on the regions sampled by the probed states. So for strongly bound systems many states need to be measured before the whole surface can be characterised. The systems studied in this thesis are loosely bound and so large regions of the potential surface are characterised by just a few bound states.

Spectroscopy of linear molecule-atom systems

The systems discussed in this work consist of a rare gas atom and a small linear molecule and have a global minimum close to a T-shaped configuration. Some similarities exist in the information gained from the spectroscopy of these systems.

Each energy level is distinguished by a set of quantum numbers. Which quantum numbers are appropriate depend on the dynamics of the system. The total orbital angular momentum is labelled J and its projection onto the intermolecular axis is labelled K. The projections of the orbital angular momentum

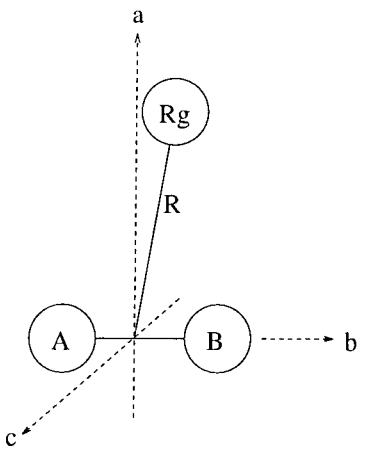

Figure 1.1: Inertial axes of a rare gas (Rg)-linear molecule (AB) Van der Waals complex.

onto the a, b, and c inertial axes are labeled K_a, K_b and K_c respectively.

For the systems considered in this thesis the a-inertial axis lies approximately along the intermolecular vector **R** and the b-inertial axis along the linear molecule, see Figure 1.1. The A rotational constant therefore gives information on the deviation of θ_{min} from 90° while the B-rotational constant gives information on the position of R_{min}.

Measurement of the bending and stretching frequencies in the infrared gives information on the force constants for these motions and so provide information directly on the anisotropy. Rotational constants measured in the infrared correspond to stretching and bending vibrations give information on the change in equilibrium distance as the molecule is bent and stretched.

These are general features of the potential which can be obtained from spectroscopy. The dynamics of the HeOCS and ArCO molecules however are quite different and so are discussed in greater detail in the relevant chapters.

1.1.5 Line broadening

The widths of lines measured in a spectrum vary for a number of different reasons. They may be broadened due to radiation damping although this occurs mainly during transitions between electronic states and so is not relevant here. Broadening of spectral lines can also be attributed to the Doppler effect. However, pressure broadening probably provides the most useful information on

intermolecular forces. A molecule only stays in a particular rotational state for a finite period of time. During collisions energy is exchanged causing broadening of the spectral lines. Energy is transfered more frequently between low j-states than higher j-states as they are more closely spaced. Consequently broadening of spectral lines can be thought of as a measure of the rate of inelastic collisions.

Much work has been done on developing methods of calculating line broadening from potentials [49,50]. Pressure broadened infrared lines were used in conjunction with spectroscopic data to test $ArCO_2$ potentials [51]. Only one of the potentials reproduced the pressure broadening data adequately. This potential failed however to reproduce the spectroscopic data, revealing a need for a new $ArCO_2$ surface. A new potential was calculated that did reproduce line broadening and the Van der Waals spectra [43, 44]. Similar calculations have been performed with other systems. Good agreement between theory and experiment was found for the majority of pressure broadened lines of HeC_2H_2 [37].

With such high quality information obtained about potentials from spectroscopy, there is little wonder that many of the models used to obtain potentials in recent years have been based on information gained from spectroscopic experiments [1,43,52].

1.2 Empirical potentials

Empirical methods involve fitting a potential function to available experimental data. The discussion here is predominantly related to atom-linear molecule complexes with the internal co-ordinates of the linear molecule fixed, but the systems studied can be viewed as prototypes. So, functional forms are developed with a view to extending them to higher dimensions to allow for monomer vibration which become important when calculating red shifts or vibrationally inelastic collisions.

The difficulty with the empirical approach is in finding a functional form that does not require many parameters to be determined in the least squares fit and that accurately reproduces all the potential features. The success of the

function will depend on the parameters chosen to be fitted. The parameters must make the function sufficiently flexible that the potential can be obtained but not so flexible that the parameters cannot be determined by the experimental data.

For Rg–H_2 systems the potential can be expanded in terms of Legendre polynomials whose coefficients are determined in a least-squares fit. The number of polynomials and the number of parameters to be fitted increase with increasingly anisotropic systems. Devising a functional form that requires fewer parameters is clearly advantageous. A potential expanded in terms of Legendre polynomials cannot be decomposed into individual potential contributions. So, generally, potential functions are constructed as a sum of functions representing the main components of the potential. The information from such a decomposition can be used to relate monomer properties to interaction energy contributions; to determine the anisotropy of each component; to aid understanding of the nature of the intermolecular interaction and may also serve as a guide to the construction of semi-empirical potentials of larger systems.

1.2.1 Short range

Short range interactions are dominated by repulsion which arises from the charge cloud of one monomer not occupying the space of the other. They are modeled with an exponential type function. A judicious choice is made, guided by the experimental data available, as to which parameters to fit. An alternative to determining the parameters from experiment is to fit them to *ab initio* interaction energies or to dimer charge density overlap at a sufficient number of different molecular configurations to cover the surface. The charge density overlap of the two monomers has been shown to be proportional to the repulsion energy [53] and can be calculated from *ab initio* monomer charge densities. The proportionality constant is determined in a fit to experimental data. This is a promising approach as it cuts down the number of parameters to be determined by experiment.

1.2.2 Electrostatics

Electrostatic interactions arise from the permanent non-uniform charge distributions of two molecules. They can be attractive or repulsive interactions but, in the multipole approximation, are zero for atom-molecule systems as atoms do not have permanent multipole moments. They are sometimes included in the functional form used for the repulsion and will not be considered here.

1.2.3 Dispersion

Dispersion is an attractive force caused by correlated fluctuations in the monomer charge clouds. The usual model adopted for the dispersion in an empirical potential is based on an expansion of the form,

$$V_{\text{disp}} = -\sum_n C_n(\theta) D_n(R) R^{-n} \tag{1.3}$$

where $C_n(\theta)$ are dispersion coefficients, $D_n(R)$ is a damping function. The form of the damping function varies but it is equal to zero at $R = 0$, in order to remove the singularity, and to unity for large values of R. The dispersion coefficients $C_n(\theta)$ are expanded in Legendre polynomials and can be calculated either from pseudo-dipole oscillator strength distributions [54] or from *ab initio* dipole-dipole and dipole-quadrupole polarisabilities at imaginary frequencies [55].

1.2.4 Induction

Induction arises from the induced multipole moments of one monomer interacting with the permanent moments of the other. It is an attractive force which is modeled using expansions involving the multipole moments of the molecule.

1.2.5 Regions not probed by experiment

For a surface of spectroscopic accuracy to be obtained, the experimental data available is important. If the system contains a hydrogen or helium atom, most regions of the potential are sampled by a few bound states [56]. For

larger systems more bound states are needed although information on large regions of the potential can be gained by measuring just a few bound states. Consequently the potential function should have the correct behaviour in regions not sampled by experiment. Physical insight can be applied or *ab initio* computations used for poorly determined regions. A failure to chose an appropriate functional form however leads to a surface that is not physically justified. Spectroscopically accurate potentials have been obtained for a number of systems with the empirical approach [57–59]. When new spectroscopic measurements are made empirical potentials can be refined further.

1.3 *Ab initio* potentials

With advances in computer technology potentials based on *ab initio* computations have become increasingly popular [2, 60, 61], although at present high quality potentials can only be computed for small molecules.

1.3.1 The supermolecular approach

The supermolecular approach is based on calculating the energy of the complex , E_{AB}, and subtracting the energy of the monomers, E_A and E_B. The interaction energy must be calculated at many different molecular configurations due to the large amplitude of motion which Van der Waals molecules exhibit. The energies obtained are subject to basis set superposition error (BSSE), an artefact of using an incomplete basis set for each monomer. BSSE causes an artificial lowering of the interaction energy although this can be corrected [62].

Semi-empirical methods

Ten years ago *ab initio* computations that included electron correlation for dimers which did not contain at least one light atom were not feasible. Hartree-Fock plus damped dispersion (HFD) combines SCF energies with an empirical form of the dispersion, that corrects for the lack of electron correlation in the SCF theory, to compute potentials. As well as repulsion energy, some induction contributions are also incorporated in the SCF calculation. An exponential

plus induction function (if induction is present) are fitted to the energies. The correction term is based on the perturbation expansion of the dispersion energy as discussed above. Many of the potentials tested against scattering data were based on HFD models. Scaling the dispersion coefficients of the HFD potential can lead to improved agreement with experiment [63,64].

HFD is highly dependent on the quality of the calculated SCF energies and dispersion coefficients. Many supermolecular SCF computations have to be performed if a global potential is to be obtained. These computations are significantly more expensive than the monomer *ab initio* charge densities used to compute charge density overlaps discussed in Section 1.2. However this was a popular method of calculating a potential to be tested against scattering data.

Theoretical methods

Ab initio potentials that include correlation can be computed for small Van der Waals dimers. Two popular approaches are Møller-Plesset perturbation theory, MP, and coupled cluster methods, CC [65,66].

The coupled cluster singles, doubles and non-iterative triples (CCSD(T)) method uses the higher level of correlation treatment of the two approaches and so recovers the greater amount of dispersion. The method is generally applied to systems containing first-row atoms [67–69] as it is computationally expensive. Møller-Plesset perturbation theory recovers much of the dispersion contribution to the potential and has been used for many systems [70–72].

Both coupled cluster and MP methods are size consistent to any order. This essentially means that the amount of electron correlation included on both the individual monomers and the dimer is the same. Both MP and CCSD are widely available in computational packages. The disadvantage of this approach is that little insight into the constituent interactions is possible.

1.3.2 The SAPT approach

Symmetry-adapted perturbation theory, SAPT, offers insight into the constituent interactions as it partitions the potential into electrostatic, exchange, induction and dispersion contributions [61]. The components are computed directly

without the need for supermolecular calculations. Therefore SAPT is not subject to BSSE and is computationally less expensive than the supermolecular approach. The surfaces obtained from such computations are of comparable quality to those from Møller-Plesset computations as was illustrated for the NeCO system [73,74]. This method has been used extensively to obtain potentials for dimer systems [75–77].

SAPT is prone to convergence problems so comparison with MP or CC potentials is useful and sometimes necessary when deciding where to truncate the expansion. In some instances arbitrary approximations have to be made. SAPT is consequently not as straightforward to use as MP or CC methods and is not widely available in standard quantum mechanical packages.

1.3.3 Obtaining the smooth potential

To convert the interaction energies (MP, CC or SAPT) into a smooth potential either a functional form is fitted to the potential data [69,71,75,78] or an interpolation scheme employed. Generally a functional form is fitted to each component of the SAPT energy whereas for MP or CC potentials either interpolation or fitting may be employed.

Fitting a functional form to *ab initio* data is subject to similar constraints as described above for the empirical approach. The functional form and parameters chosen must be appropriate for the system being studied. A functional form will not go through all the *ab initio* energies exactly, but by applying a weighting function, an improved fit can be achieved in specific regions of the potential. The function should also be chosen such that the potential is smooth and the correct asymptotic behaviour is achieved even outside the limits of the data. Therefore fewer *ab initio* points may be needed when a function is used as opposed to interpolation.

Interpolation schemes specifically designed for potential energy surfaces and that incorporate some physical knowledge have been developed [79–81], although potentials of reasonable quality can be obtained with splines [67,82]. Interpolation can only be used inside the limits of the data therefore points need to be calculated at long range if the correct asymptotic behaviour is to be

achieved. A second disadvantage of the interpolation method is that unphysical oscillations occur if insufficient points are computed, particularly in regions with a large energy gradient between consecutive points and so an unphysical potential can be produced.

Both methods of obtaining an analytical potential form are dependent on the quality of the *ab initio* points, *i.e.* the level of correlation treatment and basis set size, and the distribution of points in configuration space. Spectroscopic measurements can be useful for testing *ab initio* surfaces. Methods of using spectroscopic measurements to scale potentials are also being developed [83].

1.4 Comparing empirical and *ab initio* methods

The supermolecular approach, particularly if a big basis set is used, demands large amounts of memory and CPU time; however, a sufficiently dense grid of points for small atom-molecule systems is now computationally affordable. Empirical methods are based on comparatively inexpensive computations. The *ab initio* approach remains computationally prohibitive for much larger systems. Most of the potentials published in the literature for small Rg-molecule systems are now based on these methods. The quality of surface obtained from empirical methods are generally in closer agreement with experiment than those obtained from *ab initio* computations.

This discussion has centred around atom-molecule systems with fixed internal co-ordinates; however these systems are thought of as prototypes and being able to extend the application to larger systems is important. Typically around 100 *ab initio* interaction energies are required for a two dimensional problem. The number is nearer 1000 if monomer vibration is allowed. To go to much higher dimensions results in a prohibitive number of computations even for a method like MP2 with a large basis set. The potentials can be scaled or extrapolated at large inter-monomer distances to reduce the number of computations although empirically based methods are more easily extended to higher dimensions. Information gained from *ab initio* surfaces about the shape of the potential and monomers can aid the construction of functions for higher dimensional potentials.

1.5 Work presented here

In this thesis, both an empirical and a combined supermolecular semi-empirical approach are used to obtain a potential energy surface for ArCO. As spectroscopic data provide very detailed information on the potential surface and can, unlike scattering data, easily be incorporated into a least squares potential fit, spectroscopic data is used to refine both potentials. Second virial coefficients were used in combination with the spectroscopic measurements to determine the well depth. Potentials of spectroscopic precision are sought, that is to say the difference between theory and experiment should be less than experimental uncertainty so as to be able to predict other as yet unmeasured parts of the spectrum. One clear disadvantage of the supermolecular approach is the number of points that need to be calculated in order to obtain a potential. To date there has not been a study published in the literature on the choice of *ab initio* points, so to optimise computation of the *ab initio* surface, the distribution of points in configuration space is explored in Chapter 4. The information on the distribution of points and the co-ordinate system to use is implemented in the supermolecular approach to obtain a potential for HeOCS.

CHAPTER

2

The Ar–CO Potential: systematic model

2.1 Introduction

Since the first spectroscopic experiment on ArCO was performed 10 years ago [84], a lot of effort has been devoted to understanding the system. ArCO is one of the simplest Van der Waals molecules consisting entirely of heavy atoms, *i.e.* not involving H, D, or He, in which anisotropic intermolecular forces play a significant role. It is therefore of interest to spectroscopists and theoreticians alike.

A wealth of both rotational [85–89] and vibrational [90–95] spectroscopic quantities have been measured for ArCO. These are shown schematically in Figure 2.1. The quantum numbers chosen by Xu and McKellar [94] to label the energy levels will be used here. They are (v_{CO}, v_2, v_3, K), where v_{CO} corresponds to excitation of the CO monomer; v_2 to excitation of the bending

vibration and v_3 to the Van der Waals stretching vibration; j to the angular momentum of the CO monomer; J to the total orbital angular momentum and K (or K_a) to its projection onto the a inertial axis. For rotational transitions the projection of the orbital angular momentum onto the b and c inertial axes are labeled K_b and K_c respectively.

McKellar *et al.* [90] measured six $\Delta K = \pm 1$ perpendicular transitions. They suggested that the complex was an approximately T-shaped near-prolate asymmetric rotor. This was confirmed later by microwave and millimetre wave experiments [85,86], in which nine a-type ($\Delta J = +1$, $\Delta K_a = 0$, $\Delta K_c = +1$) and two b-type ($\Delta K_a = \pm 1$) transitions were measured.

The first probe of the Van der Waals bending motion was by Havenith *et al.* [91] who detected the in plane bend. Later, the same group also observed the $K = 1$ levels for this state [92] which corresponded to the simultaneous excitation of the in plane and out of plane bends. One component was found to be strongly coupled, through Coriolis interactions, to an at that time unknown $K = 0$ state, later found to be the $K = 0$ Van der Waals stretch [94]. These were both for the $v_{\mathrm{CO}} = 1$ state. The Havenith group also identified the most recent Van der Waals state to be observed as the $K = 1$ level for this stretching motion [95]. Comprehensive analysis of the ArCO spectra was carried out by McKellar *et al.* [89,94], who also measured the $v_{\mathrm{CO}} = 0, K = 0$ bending and stretching frequencies, but did not include the $K = 1$ stretching mode as it had not been published at that time.

Few scattering experiments have been performed with ArCO. Early elastic scattering experiments were in the energy range 215 to 1245 eV and performed at room temperature [96] while more recently elastic differential cross sections were recorded for energies as low as 100 eV [31]. During the last few years some work has been done on line broadening and rotational energy transfer [97–99].

Several attempts have been made to obtain the ArCO potential energy surface for use in the assignment of energy levels with limited success [67,100–105]. None of the potentials accurately reproduce all of the bound states measured thus far. The recent *ab initio* studies by Shin *et al.* [67], Jansen [104] and Chałasiński *et al.* [106] use the highest levels of correlation treatment and

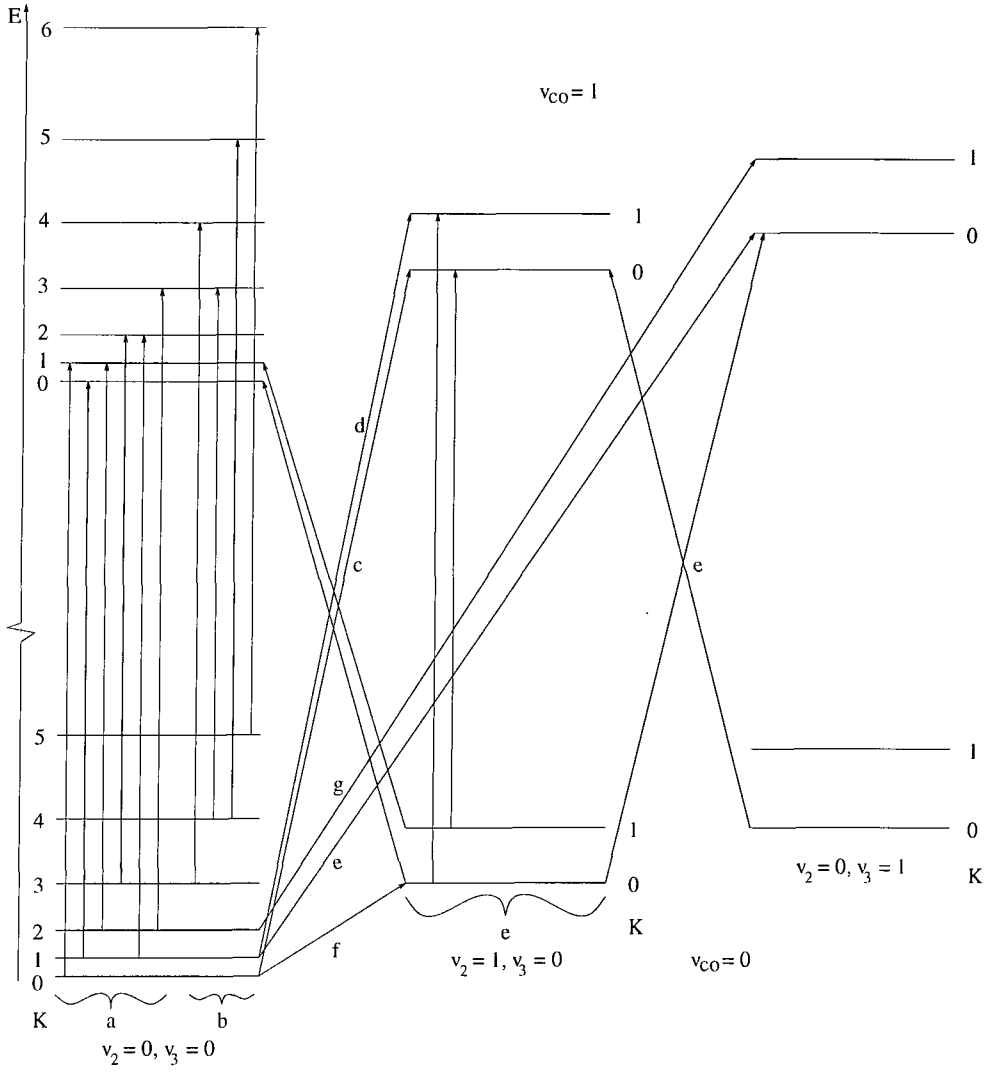

Figure 2.1: Energy level diagram showing the experimentally observed transitions for ArCO. Asymmetry splittings and rotational structure, measured by Ogata *et al.* [85], Jäger and Gerry [86] and Hepp *et al.* [87] are omitted for simplicity. (a.) IR transitions measured by McKellar *et al.* [90]. (b.) IR transitions measured by McKellar, Havenith *et al.* [93]. (c.) Van der Waals bend measured by Havenith *et al.* [91]. (d.) Doubly excited Van der Waals bending state, Havenith *et al.* [92]. (e.) IR transitions measured by McKellar *et al.* [94]. (f.) Millimetre-wave measurements by McKellar *et al.* [88]. (g.) Doubly excited Van der Waals stretching state measured by König and Havenith [95].

largest basis sets and so are the ones considered here. The surfaces by Shin *et al.* [67] and Jansen [104] are the ones that achieve closest agreement with experiment.

Symmetry-adapted perturbation theory was combined with Møller-Plesset perturbation theory by Chałasiński *et al.* [106] to calculate the potential energy surface of ArCO. They found the surface had a minimum of 108.9 cm^{-1} close to a T-shaped configuration. Their computation of the surface did not cover a large enough region of configuration space to be able to do bound state computations, so no comparison with spectroscopic data was possible.

Shin *et al.* [67] calculated interaction energies on a grid of 77 points, 11 radial and 7 angular, using the MP4 method with a basis set consisting of both, bond and atom-centred functions. The potential was projected out in Legendre polynomials and a cubic spline interpolated between the projection coefficients in order to obtain an continuous potential form. Bound state computations in which Coriolis interactions were neglected were performed and qualitative agreement with experiment obtained. The potential was thought however to be globally too shallow [67].

Jansen [104] obtained a potential surface from an irregular grid of 70 interaction energies, at 5 angular points and 14 radial points, calculated using coupled-pair functionals with atom-centred basis sets. In order to project out the potential in Legendre polynomials a cubic spline in the angular co-ordinate was performed to generate interaction energies at 19 Gauss-Legendre quadrature points. Cubic splines were adopted in the radial co-ordinate to generate a continuous potential form within the limits of the data set, while an extrapolation scheme was used beyond the limits of the *ab initio* data. Improved agreement with experiment was obtained with most states except the $K = 1$ stretching state when an anisotropic scaling was applied.

Despite the volume of work on ArCO, the need remains for a potential energy surface that agrees with all the experimentally observed states which can be used to predict other, as yet unobserved states and properties of ArCO. In the present work, the systematic potential model, developed by Wheatley and Price [107], is applied to the ArCO system. This model partitions the potential into physically meaningful pieces (repulsion, dispersion and induction) and

avoids the computational expense of supermolecular *ab initio* calculations. The resulting potential is then refined to gain closer agreement with the available experimental data. Physical insight can be incorporated into the construction of each part of the potential; this is particularly advantageous in regions that are not probed by experiment. It was thought that the model can be applied to many systems with only small adjustments in the initial functional form [108]. Since many bound states of ArCO have been measured experimentally, and the systematic model was used successfully for $ArCO_2$ by Hutson *et al.* [43], the same approach is adopted here for ArCO.

2.2 Methods

2.2.1 Co-ordinate system

The Jacobi co-ordinate system will be used a number of times in this thesis and so is illustrated in Figure 2.2 for the general atom-linear molecule case. The

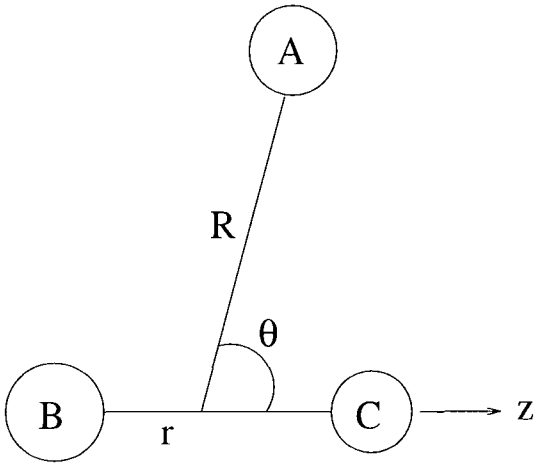

Figure 2.2: The Jacobi co-ordinate system for an atom linear molecule system.

linear molecule is placed along the z-axis with the centre of mass at the origin and the atom furthest away from the centre of mass placed in the positive z-direction. The distance from the centre of mass of the molecule to the atom is represented by the vector $\mathbf{R}$ and the angle formed between $\mathbf{R}$ and the z axis is denoted θ.

For ArCO, $\theta = 0°$ corresponds to argon at the carbon end and $\theta = 180°$ to argon at the oxygen end. This convention is also followed by Shin *et al.* [67]

but the opposite convention is used by Jansen [104] and Chałasiński *et al.* [106].

2.2.2 Systematic model

The systematic model represents the potential as a summation of repulsion, dispersion and induction energies,

$$V(R,\theta) = V_{\text{rep}}(R,\theta) + V_{\text{disp}}(R,\theta) + V_{\text{ind}}(R,\theta). \tag{2.1}$$

The principal force of attraction in ArCO is dispersion. Induction contributions to the energy are small. Therefore only dispersion and repulsion interactions are considered here. Although induction effects are not considered explicitly, they are included implicitly via the parameters floated in the least squares fit.

High-quality experimental data, that probe different regions of the potential surface, are a particularly useful aid in the construction of potential energy surfaces. The data can be used both to assess the quality of a surface and to refine the surface to achieve improved agreement with experiment. Agreement with experiment is unlikely if individual contributions to the energy are poorly represented because the surface will be far from the 'true' potential which makes refinement difficult. Therefore physical insight should be built into the functional forms used to model the individual contributions to the potential.

2.2.3 Repulsion

The spectroscopic data available for ArCO sample only the well region of the potential. If a global potential is to be computed, that can be used for scattering calculations as well as to help with spectroscopic analysis, a good model for the repulsive wall is essential. Hence physical insight has to be incorporated into the construction of the model of the repulsion energy component of the potential. As shown empirically by Kita [53], the charge density overlap of the two monomers is proportional to the repulsion energy such that

$$V_{\text{rep}}(R,\theta) = K_\rho S_\rho(R,\theta) \tag{2.2}$$

where K_ρ is the repulsion factor and

$$S_\rho(R,\theta) = \int \rho_{\text{Ar}}\rho_{\text{CO}}\, d\tau. \tag{2.3}$$

The argon and carbon monoxide charge densities are denoted ρ_{Ar} and ρ_{CO} and $S_\rho(R,\theta)$ denotes the charge density overlap of the monomers. The scaling factor K_ρ, controls the repulsion contributed to $V(R,\theta)$. Its optimal value however is unknown and so is determined by the method of least-squares as will be described in section 2.6.

Monomer charge densities were calculated using second-order Møller-Plesset perturbation theory (MP2), with an [8s6p3d] basis set taken from the inbuilt basis sets in CADPAC [109] on both C and O, and an uncontracted (14s10p4d) basis set on argon [110] using Gaussian 94 [111]. The CO bond length was fixed at $2.132a_0$.

MP2 monomer charge densities, for both monomers, were converted into gaussian multipoles which were then moved to the nearest nucleus using the GMUL program [112,113]. The charge density overlap, S_ρ was also determined using GMUL at a grid of 8 evenly spaced distances in R between 5.0 a_0 and 8.5 a_0 and 19 Gauss-Legendre quadrature points in θ. These charge density overlaps were then fitted to the function used by Atkins and Hutson [114] for HeHCN,

$$S(R,\theta) = \exp(-\beta(\theta)(R - R_w(\theta))), \tag{2.4}$$

where $\beta(\theta)$ and $R_w(\theta)$ are expanded in terms of Legendre polynomials,

$$\beta(\theta) = \sum_\lambda \beta_\lambda P_\lambda(\cos\theta) \tag{2.5}$$

and

$$R_w(\theta) = \sum_\lambda R_{w,\lambda} P_\lambda(\cos\theta). \tag{2.6}$$

The individual β_λ and $R_{w,\lambda}$ were determined, using the NAG least-squares fitting routine E04FDF, from the charge density overlap data generated with GMUL. A gaussian weighting function in $\ln S_\rho$ with a width of 1.5 a.u. centred around repulsion energies of 300 cm^{-1} ensured a good fit in the lower part of the potential wall. The β_λ and $R_{w,\lambda}$ parameters are given in Table 2.1. The functional form used for the charge density overlap differs from that used by Hutson *et al.* [43] for the $ArCO_2$ case because the anisotropy in ArCO is smaller than in $ArCO_2$.

λ	$R_{w,\lambda}$ / a_0	β_λ / a_0^{-1}
0	2.56519	2.00488
1	0.16269	−0.11181
2	0.68410	0.01603
3	0.08688	0.03505
4	−0.05489	0.00973
5	−0.02692	−0.00975
6	0.00381	−0.00486
7	0.00857	0.00333
8	0.00133	0.00190
9	−0.00274	−0.00113

Table 2.1: The parameters of the S_ρ function found by the method of least-squares.

An expansion to $\lambda_{\max} = 9$ in Legendre polynomials gave adequate convergence of the series.

2.2.4 Dispersion

Both a single-site and a two-site representation of the dispersion interaction are investigated. In the case of $ArCO_2$, the best model of the dispersion was a two-site expansion on the CO_2 monomer [43]. A single-site expansion was found to be poorly convergent due to the size of CO_2. For HeHCN, two different potential models were used, one employing a central dispersion and the other a two-site dispersion model [114]. The different potentials gave equally good agreement with the experimental data. Carbon monoxide is smaller than CO_2 and HCN, so the dispersion might be adequately described by a single-site expansion.

Single-site dispersion expansion

The dispersion expansion used was,

$$V_{\text{disp}}(R,\theta) = -\sum_{n=6,8,10,\ldots}\sum_{\lambda=0,2,4,\ldots}\frac{C_n^\lambda D(R)}{R^n}P_\lambda(\cos\theta), \tag{2.7}$$

with dispersion coefficients C_n^λ, Legendre polynomials $P_\lambda(\cos\theta)$, and a damping function $D(R)$. The dispersion was placed at the centre of polarisability where $C_7^1 + C_7^3 = 0.0$ so odd-order terms in the expansion were neglected. The C_7 coefficients are related to C_6^0 by dipole-dipole polarisabilities and dipole-quadrupole polarisabilities,

$$C_7^1 = \frac{4A_\perp}{\bar{\alpha}} C_6^0, \qquad C_7^3 = \frac{2(3A_\parallel - 4A_\perp)}{3\bar{\alpha}} C_6^0, \tag{2.8}$$

where

$$\bar{\alpha} = \frac{1}{3}(\alpha_\parallel + 2\alpha_\perp). \tag{2.9}$$

Dipole-quadrupole polarisabilities are origin dependent and were calculated relative to the centre of mass [115]. The equations

$$A'_\parallel = A_\parallel - 2r\alpha_\parallel \quad \text{and} \quad A'_\perp = A_\perp - \frac{3}{2} r\alpha_\perp \tag{2.10}$$

which come from the work by Buckingham [116], were used to displace the dipole-quadrupole polarisabilities. The prime marks the dipole-quadrupole polarisability that has been displaced by an amount r along the z-axis. These equations with $A_\parallel = 13.92\ e^2 a_0^3 E_h^{-1}$ and $A_\perp = 15.01\ e^2 a_0^3 E_h^{-1}$ [115], the centre of polarisability was found to be $0.559\ a_0$ closer to carbon. Using the expression for a centro-symmetric molecule however is an approximation.

The pseudo-dipole oscillator strength distributions (pseudo-DOSDs) of Meath *et al.* [117] were used to evaluate $C_6^0 = 71.66\ E_h a_0^6$. Dipole-dipole polarisabilities, α, calculated by Maroulis [118] were used to evaluate,

$$\frac{C_6^2}{C_6^0} = \frac{\alpha_\parallel - \alpha_\perp}{\alpha_\parallel + 2\alpha_\perp} = 0.092. \tag{2.11}$$

The ratio used by Hutson *et al.* [43] for the relationship between C_6^λ coefficients and higher dispersion terms,

$$\gamma = \frac{C_8^\lambda}{C_6^\lambda}, \tag{2.12}$$

and the ratio from Thakkar and Smith [119],

$$\frac{C_{10}^\lambda}{C_8^\lambda} = \frac{49 C_8^\lambda}{40 C_6^\lambda} \tag{2.13}$$

were employed. The C_8 ratio, γ, controls the amount of C_8 dispersion contributed to the potential without affecting C_6 and is determined in the least-squares fit to experimental data.

The final term in equation 2.7 to be considered is the damping function. This was taken from the work of Meath *et al.* [117,120],

$$\begin{aligned} D(R) &= 1 & R &\geq R^d, \\ D(R) &= \exp[-0.4((R^d/R)-1)^2] & R &< R^d, \end{aligned} \tag{2.14}$$

where R^d is the damping distance. For two interacting hydrogen atoms, the damping distance is $10.01a_0$. R^d for ArCO was chosen to correspond to a distance from the centre of mass of CO, $9.09a_0$, where the electron density was approximately equal to the electron density of the hydrogen system at $10.01a_0$.

Two-site dispersion expansion

The approach adopted to partition the dispersion between two sites is an extension of the work of Douketis *et al.* [64], who showed how to partition the dispersion interaction between the centre of mass and a second site in the molecule chosen on physical grounds. In this work, a dispersion expansion centred at the centre of mass of the CO monomer (chosen because $A_{\|}$ and $A_{\perp}$ are calculated relative to this point) is divided between two sites along the CO bond. A single dispersion expansion centred at the centre of mass for CO–Ar is,

$$V_{\text{disp}}(R,\theta) = -\sum_{n=6,8,10,\ldots} \frac{C_n(\theta)D(R)}{R^n}, \tag{2.15}$$

with

$$C_6(\theta) = C_6^0 + C_6^2 P_2(\cos\theta) + C_7^1 R^{-1}\cos\theta + C_7^3 R^{-1}\cos^3\theta \tag{2.16}$$

the first term in the expansion. Note that this includes C_7 terms. However this central expansion is partitioned into two centro-symmetric segments which do not involve C_7 terms.

The two-site dispersion expansion is,

$$V_{\text{disp}}(R,\theta) = -\sum_i \sum_{n=6,8,10} \sum_{\lambda=0,2} \frac{C_{n,i}^{\lambda} D(R_i)}{R_i^{-n}} P_\lambda(\cos\theta_i), \tag{2.17}$$

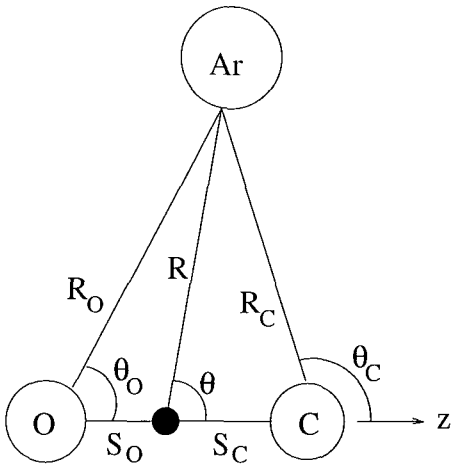

Figure 2.3: The co-ordinate system for the two-site dispersion. For illustrative purposes the dispersion sites are placed on the atomic centres although this may not be the optimum place for the sites. The black dot marks the centre of mass.

where the sum over i represents the sum over the two dispersion expansions. The dispersion is moved from the centre of mass toward carbon and oxygen but the exact location of the dispersion expansions and how much dispersion should be located there needs careful consideration.

The partitioned dispersion coefficients were expanded,

$$\begin{aligned} C_{n,\mathrm{C}}(\theta) &= C^0_{n,\mathrm{C}} + C^2_{n,\mathrm{C}} P_2(\cos\theta) \quad \text{and} \\ C_{n,\mathrm{O}}(\theta) &= C^0_{n,\mathrm{O}} + C^2_{n,\mathrm{O}} P_2(\cos\theta), \end{aligned} \tag{2.18}$$

where the subscripts C and O denote the nucleus, carbon or oxygen, the expansion site is closest to. The co-ordinate system for the dispersion expansion is given in Figure 2.3. R_O and R_C represent the distances from argon to the expansion site closest to oxygen and to carbon respectively, and S_O and S_C the distances from the centre of mass to the dispersion sites. At long range ($R_\mathrm{O} \gg S_\mathrm{O}$ and $R_\mathrm{C} \gg S_\mathrm{C}$),

$$C_n(\theta)R^{-n} = C_{n,\mathrm{C}}(\theta_\mathrm{C})R_\mathrm{C}^{-n} + C_{n,\mathrm{O}}(\theta_\mathrm{O})R_\mathrm{O}^{-n}. \tag{2.19}$$

R_C^{-n} and R_O^{-n} were expressed in terms of R, and the anisotropic dispersion terms $C_{n,\mathrm{C}}(\theta_\mathrm{C})$ and $C_{n,\mathrm{O}}(\theta_\mathrm{O})$ in terms of $\cos\theta$ using the Maclaurin expansion. The resulting equation, which when one site is placed at the centre of mass simplifies to equation (16) in the work of Douketis *et al.* [64], is

$$C_n(\theta)R^{-n} = ((C^0_{n,\mathrm{O}} + C^0_{n,\mathrm{C}})R^{-n} + (C^2_{n,\mathrm{O}} + C^2_{n,\mathrm{C}})R^{-n}P_2(\cos\theta)$$

$$+ \quad \cos\theta R^{-(n+1)}[n(S_O C^0_{n,O} + S_C C^0_{n,C}) - (3 + \frac{n}{2})(S_O C^2_{n,O} + S_C C^2_{n,C})]$$
$$+ \quad 3\cos^3\theta R^{-(n+1)}(S_O C^2_{n,O} + S_C C^2_{n,C})(1 + \frac{n}{2}) + \ldots. \qquad (2.20)$$

For $n = 6$, the lowest-order dispersion coefficient required in the series expansion for neutral interacting species,

$$\begin{aligned} C_6(\theta)R^{-6} &= C^0_6 R^{-6} + C^2_6 P_2(\cos\theta) \\ &+ 6\cos\theta R^{-7}(S_O C^0_{6,O} + S_C C^0_{6,C} - S_O C^2_{6,O} - S_C C^2_{6,C}) \\ &+ 12\cos^3\theta R^{-7}(S_O C^2_{6,O} + S_C C^2_{6,C}). \end{aligned} \qquad (2.21)$$

Equating $C_6(\theta)$ from the central expansion and the partitioned expansion gives,

$$\begin{aligned} C^1_7 &= 6(S_O C^0_{6,O} + S_C C^0_{6,C} - S_O C^2_{6,O} - S_C C^2_{6,C}) \quad \text{and} \\ C^3_7 &= 12(S_O C^2_{6,O} + S_C C^2_{6,C}). \end{aligned} \qquad (2.22)$$

So, using equation 2.8,

$$\frac{S_O C^0_{6,O} + S_C C^0_{6,C}}{C^0_6} = \frac{3A_\parallel + 8A_\perp}{18\alpha} \qquad (2.23)$$

and

$$\frac{S_O C^2_{6,O} + S_C C^2_{6,C}}{C^0_6} = \frac{3A_\parallel - 4A_\perp}{18\alpha}. \qquad (2.24)$$

These equations relate the partitioned dispersion coefficients and their locations to the central C^0_6 coefficient and monomer electrical properties. Higher order dispersion expansion coefficients on the individual sites were evaluated using the ratios given in equations 2.12 and 2.13.

For the purposes of the least-squares fit a parameterized form of the positions of the dispersion sites is required. Physical quantities that can be related to and determined by the experimental data are needed. The positions of the two dispersion sites relative to the centre of mass are related by

$$S_O = S_1 + aS, \qquad S_C = S_1 + (1 + a)S, \qquad (2.25)$$

where S_1 is the distance from the centre of mass to the centre of polarisability; S is the distance between the two dispersion sites and a dictates how much dispersion is moved toward oxygen and how much is moved toward carbon. Substituting 2.25 into 2.23 and 2.24 gives,

$$S_1 + aS + S\frac{C^{0,C}_6}{C^0_6} = \frac{3A_\parallel + 8A_\perp}{18\bar{\alpha}} \quad \text{and}$$

$$(S_1 + aS)\frac{C_6^2}{C_6^0} + S\frac{C_6^{2,C}}{C_6^0} = \frac{3A_{\|} - 4A_{\perp}}{18\bar{\alpha}}. \quad (2.26)$$

Thus by using this parameterisation some quantities can be chosen on physical grounds.

The position of the two dispersion sites will be determined by the experimental data in the least-squares fit because the optimum position of the dispersion sites is unclear. A small displacement from the centre of mass might be required or alternatively it may be appropriate to place them as far apart as the nuclei.

2.3 Experimental data

As discussed in the introduction, many experimental transitions have been observed for the ArCO system; these are shown schematically in Figure 2.1. Not all of the available experimental data however will be used in the fit. The data selected give information about different features of the potential. Some energy levels are excluded from the fit to avoid duplication of information.

All the energy levels are calculated from the spectroscopic parameters of Xu and McKellar [94] with the exception of the most recently observed $(1, 0, 1, 1)$ state [95] which had not been measured at that time. Xu and McKellar [94] used all existing IR, millimetre and microwave transitions in a fit to the energy level expressions given in equations 2.27 and 2.29 to determine spectroscopic parameters for the ArCO complex. As the $(1, 0, 1, 1)$ state has only been measured for $v_{CO} = 1$, all the transitions used will be for the $v_{CO} = 1$ state. The potential surface is thought to change little upon excitation of the CO monomer.

Xu and McKellar [94] adopted the following expression for the rotational energy levels of ArCO,

$$\begin{aligned} E_{\text{total}}(J,K) = E_0 &+ B(J(J+1) - K^2) - D(J(J+1) - K^2)^2 \\ &+ H(J(J+1) - K^2)^3 + L(J(J+1) - K^2)^4 \\ \pm\frac{1}{2}\Big(&bJ(J+1) + d(J(J+1))^2 + h(J(J+1))^3 + l(J(J+1))^4\Big). \end{aligned} \quad (2.27)$$

Unless otherwise stated in the following $J = K$. The following energy level differences were calculated from Equation 2.27 and used in the least-squares

fit of the systematic potential,

$$(1,0,0,1^-) \leftarrow (1,0,0,0) = 2.464\ \mathrm{cm}^{-1} \quad \text{and}$$
$$(1,0,0,2^-) \leftarrow (1,0,0,1^-) = 6.726\ \mathrm{cm}^{-1},$$

along with the corresponding asymmetry splittings,

$$(1,0,0,1^+) \leftarrow (1,0,0,1^-) = -129.946\ \mathrm{MHz} \quad \text{and}$$
$$(1,0,0,2^+) \leftarrow (1,0,0,2^-) = -873.153\ \mathrm{MHz},$$

where the superscripts + and − refer to parity. The information gained from these transitions is essentially the A rotational constant and is a measure of the deviation of the global minimum from $\theta = 90°$ while the information gained from the asymmetry splittings is on the amplitude of motion.

By taking combination differences of energy levels, and discarding higher order terms, quantities approximately proportional to the rotational and centrifugal distortion constants can be evaluated. With $K = 0$ equation 2.27 becomes, for the lowest values of J,

$$E(0,0) = E_0, \quad E(1,0) \approx E_0 + 2B - 4D, \quad E(2,0) \approx E_0 + 6B - 36D, \tag{2.28}$$

where terms higher than D have been discarded. The quantity $E(1,0) - E(0,0) = 4143.520\ \mathrm{MHz} \approx 2B$ is used in the least squares fit. It gives information on the radial position of the global minimum. In contrast, the centrifugal distortion constant is a measure of the force constant for the Van der Waals stretching motion, so it gives information on the radial curvature of the potential around the minimum. It can also give an indication of the well depth. The expression used in the least squares fit is

$$(E(2,0) - E(1,0)) - 2(E(1,0) - E(0,0)) = -1.522\ \mathrm{MHz} \approx -24D.$$

The same expressions can be used for the rotational and centrifugal distortion constants of the $(1,1,0,0)$ state. Rather than fitting to both the rotational constants, the ground state rotational constant is used and the difference between the ground state rotational constant and the $K = 0$ excited bending state rotational constant. The difference between the two rotational constants is 229.376 MHz and $-24D \approx -1.190$ MHz for the excited state.

In addition to these low-lying rotational transitions, the higher energy levels corresponding to the Van der Waals motions were also included.

The $(1,0,1,0)$ stretching state and the $(1,1,0,1^-)$ doubly excited bending states are highly mixed due to Coriolis interactions. Hence the rotational energy level expression of equation 2.27 did not adequately reproduce the transitions. The expression given in equation 2.29 was found to be more satisfactory,

$$E_{\text{total}}(J,K) = \frac{E_1 + E_2}{2} \pm \sqrt{W^2 + \left(\frac{E_1 + E_2}{2}\right)^2}, \tag{2.29}$$

where

$$\begin{aligned} E_i &= E_0 + B(J(J+1) - K^2) - D(J(J+1) - K^2)^2 \quad \text{and} \\ W &= C\sqrt{J(J+1)}. \end{aligned}$$

Thus the energy differences calculated from the above expression,

$$\begin{aligned} (1,1,0,1^-) \leftarrow (1,1,0,0) &= 5.183\ \text{cm}^{-1}, \\ (1,0,1,0) \leftarrow (1,0,0,0) &= 18.097\ \text{cm}^{-1}, \\ (1,1,0,1^+) \leftarrow (1,1,0,1^-) &= -995.221\ \text{MHz}, \end{aligned}$$

were used in the least-squares fit. The stretching state gives information on the radial amplitude of motion. Furthermore, the last of these transitions is an asymmetry splitting which should serve as a sensitive test of the potential.

In the most recent work on Ar–CO by Havenith *et al.* [95], the doubly excited stretching state was observed for the $v_{\text{CO}} = 1$ state. Therefore, the transition $(1,0,1,1^-) \leftarrow (1,0,1,0) = 8.163\ \text{cm}^{-1}$ was put into the least-squares fit along with the asymmetry splitting $(1,0,1,1^-) \leftarrow (1,0,1,1^+) = -47.613$ MHz. This gives information quite high up the potential and is the highest Van der Waals state yet observed. These energy levels combine to ensure that both the lower and upper parts of the potential well are correct.

In addition to the spectroscopic data, second virial coefficients, measured by Schramm *et al.* [11], were added to the least-squares fit to give information on the well volume. They have values $B = -11.9$, -2.1, $+5.2$ and $+9.3$ cm^3/mole, at $296.15, 353.15, 413.15$ and 463.15 K respectively. In combination with the spectroscopic data the virial coefficients can help to determine the well depth.

Given the quantity of information obtained about the potential from spectroscopic data and virial coefficients, no other data were required to fit the parameters.

Weights used in the least-squares fit represent the desired accuracy of the calculated potential fit. Their values were guided by the experimental uncertainties and are reported with the results in section 2.6.

2.4 Bound states calculations

In order to compare the rovibrational levels for the two-site potential with those from experiment, coupled channel equations were solved using the BOUND program [121]. The CO rotational constant for $v_{CO} = 1$ was taken as $b_{CO} = 1.9050253$ cm^{-1} [122], with basis functions up to $j = 14$. The reduced mass of the complex was $16.46244844 m_u$ and the coupled equations propagated from $R_{min} = 2.4$ to $R_{max} = 6.5$ Å. This gives convergence to better than 1×10^{-6} cm^{-1} for the eigenvalues and 1×10^{-4} MHz for the rotational constants.

2.5 Unfitted surface

As discussed in the introduction, the *ab initio* potentials computed by Shin *et al.* [67] and Jansen [104] gave reasonably good agreement with experiment. Hence the general shape of these potentials must be close to the shape of the 'true' potential. The best calculation of the global minimum however was by Chałasiński *et al.* [106] who used the highest level of correlation treatment and the largest basis sets in their *ab initio* computations. In order to determine a good starting point from which to fit to experiment, the potentials resulting from the one-site and two-site models were compared with the *ab initio* potentials of Shin *et al.* [67], Jansen [104] and Chałasiński *et al.* [106]. Qualitative rather than quantitative agreement was sought but deviations from the *ab initio* surfaces greater than approximately 10 cm^{-1} in absolute energies and 0.1 Å in absolute position were interpreted as errors in the systematic potential. Comparison with experiment is also made. Calculated transitions that agree with experiment to within approximately 2 cm^{-1}, and rotational constants reported

in MHz that agree to within approximately 5% of the experimental value are sought as a starting point before a fit to experiment is likely to be successful.

The key features of the *ab initio* potentials used for the comparison are given in Table 2.2.

2.5.1 Single-site dispersion model

It will be illustrated below that the shape of the potential resulting from the single site approach is not very satisfactory and is significantly different to the *ab initio* potentials in the literature.

Initially, the repulsion factor, K_ρ and the dispersion ratio, γ were set to 4.5 and 30.0 respectively, the values found to be optimal for $ArCO_2$ [43]. The resulting surface is given in Figure 2.4 and the key features in Table 2.3.

Comparison of the potential features quoted in Tables 2.2 and the column of Table 2.3 with $K_\rho = 4.5$, $\gamma = 30.0\ a_0^2$, reveals that the one-site systematic potential is too shallow at the oxygen end, too deep at the global minimum but approximately correct at the carbon end. A number of differences between the systematic potential and the *ab initio* potentials can be observed.

1. The systematic potential, like the *ab initio* potentials, has a global minimum close to an approximately T-shaped geometry with $\theta = 85°$. This places argon slightly closer to carbon than to oxygen, which is the inverse of the *ab initio* surfaces. The global minimum is close to 145 cm^{-1} deeper than the potentials obtained by Jansen [104] and Chałasiński *et al.* [106]. The excessive depth of the potential in this region suggests that the repulsion contribution to the energy should be increased, $K_\rho = 4.5$ is too small. It may also be true that $\gamma = 30.0\ a_0^2$ is too large.

2. The difference in energy between the saddle points at 0° and 180° is 24.9 cm^{-1} for the single-site model compared to -6.1 cm^{-1} and -14.4 cm^{-1} for the *ab initio* surfaces. As well as the difference in energy being too great, the relative well depths at the two ends are the wrong way around. As mentioned above, the systematic potential is in reasonably close agreement with the *ab initio* potentials at the carbon end. The discrepancy lies at the oxygen end where the systematic potential is approximately

Feature	Jansen (1996) [104]	Chałasiński *et al.* [106]	Shin *et al.* [67]
Ar – CO	82.6 cm^{-1}	not	68.3 cm^{-1}
Saddle point	0°	available	4.58 Å, 0°
Global	108.6 cm^{-1}	108.9 cm^{-1}	96.3 cm^{-1}
minimum	3.68 Å, 97°	3.70 Å, 110°	3.74 Å, 98°
CO – Ar	88.7 cm^{-1}	not	82.7 cm^{-1}
Saddle point	180°	available	4.04 Å, 180°

Table 2.2: Potential features of the most recent *ab initio* potentials in the literature. The top figure of each row of the table is the depth of the feature and the bottom is its position. Note the position of the global minimum in Ref. 106 is reported as (3.70 Å, 80°), for comparison purposes this has been changed to agree with the sign convention adopted in this work. Ar–CO and CO–Ar refer to the saddle points at the carbon and oxygen ends respectively.

Feature	$K_\rho = 4.5$ $\gamma = 30.0\ a_0^2$	$K_\rho = 10.0$ $\gamma = 30.0\ a_0^2$	$K_\rho = 4.5$ $\gamma = 15.0\ a_0^2$
Ar–CO	68.69 cm^{-1}	37.92 cm^{-1}	42.92 cm^{-1}
$(R/$ Å$, \theta/°)$	$(4.48, 0)$	$(4.91, 0)$	$(4.66, 0)$
Global min	253.55 cm^{-1}	104.07 cm^{-1}	103.97 cm^{-1}
$(R/$ Å$, \theta/°)$	$(3.30, 85)$	$(3.82, 87)$	$(3.65, 86)$
CO–Ar	43.81 cm^{-1}	27.71 cm^{-1}	30.02 cm^{-1}
$(R/$ Å$, \theta/°)$	$(4.21, 180)$	$(4.34, 180)$	$(4.34, 180)$
Difference	24.88 cm^{-1}	10.21 cm^{-1}	12.90 cm^{-1}
(Ar–CO)–(CO–Ar)	0.27 Å	0.57 Å	0.41 Å

Table 2.3: Key features of the potential resulting from the single dispersion site model. The values of K_ρ and γ are given for each column. The top number of each row is the energy and the bottom the position of the feature. Ar–CO and CO–Ar refer to the saddle points at the carbon and oxygen ends respectively. The bottom row of the table gives the difference in the depth of the saddle point at the carbon and oxygen end and the difference in the interaction distance, R.

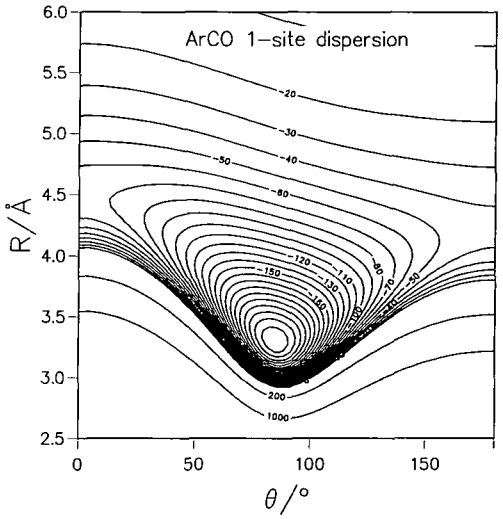

Figure 2.4: The single-site dispersion model of the ArCO potential with $K_\rho = 4.5$ and $\gamma = 30.0\ a_0^2$. Contours are labeled in cm^{-1}.

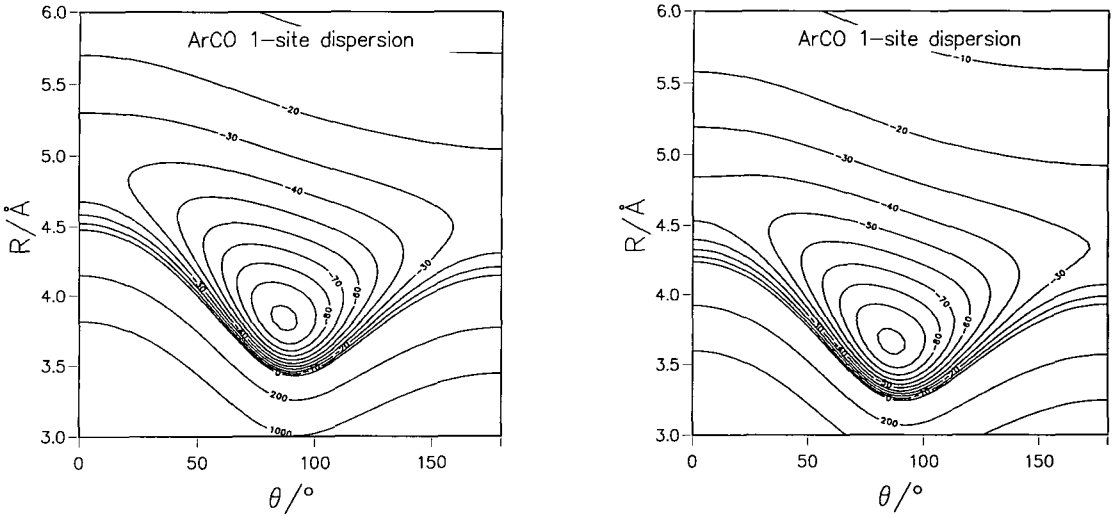

Figure 2.5: The single-site dispersion model of the ArCO potential. The plot on the left is with $K_\rho = 10.0$ and $\gamma = 30.0\ a_0^2$ and the one on the right $K_\rho = 4.5$ and $\gamma = 15.0\ a_0^2$. Contours are labeled in cm^{-1}.

39 cm^{-1} too shallow compared with Ref. 67 and 45 cm^{-1} too shallow compared with Ref. 104.

3. The difference in the value of R for the saddle point at the carbon end compared to that at the oxygen end is 0.27 Å. The potential by Shin *et al.* [67] has a difference of 0.54 Å between the values of R.

Item 1 suggests that the potential needs more repulsion and less dispersion in the well region whereas item 2 suggests that more dispersion is needed at the oxygen end. At this stage the difference between the potentials is too great to even consider performing a least-squares fit to experimental data.

There are two parameters, K_ρ and γ, which can be used to try to reduce the differences outlined in items 1 to 3 above. First consider the effect of K_ρ on the potential. The surface resulting from $K_\rho = 10.0$ and $\gamma = 30.0\ a_0^2$ is plotted in Figure 2.5 and the key features given in Table 2.3. By increasing the value of K_ρ, the repulsion contribution to the potential has increased. Therefore the well depth has decreased and the radial distance, R, at the saddle points and the global minimum has also increased.

As can be seen from a comparison of the quantities quoted in Table 2.2 and 2.3, the global minimum for the systematic model now lies in the range of those quoted in Table 2.2 for the *ab initio* surfaces. However the potential is too shallow at both the oxygen and carbon ends.

The other parameter which can be varied is γ. Decreasing γ decreases the depth of the potential at the global minimum and the saddle points while increasing the radial distance, R, at these features. The potential with $K_\rho = 4.5$ and $\gamma = 15.0\ a_0^2$ is plotted in Figure 2.5.

By comparing the quantities quoted in Table 2.3 for $K_\rho = 4.5$ $\gamma = 15\ a_0^2$ with those in Table 2.2, it is seen that the global minimum from the systematic potential is within the range of the *ab initio* potentials; the saddle points at the carbon and oxygen ends are shallower than the *ab initio* potentials. The smallest discrepancy is at the carbon end.

To further assess the shape of the potential, some key spectroscopic quantities calculated from the potential with $K_\rho = 4.5$ and $\gamma = 15.0\ a_0^2$ are given in Table 2.4. The calculated $(1,0,0,1^-) \leftarrow (1,0,0,0)$ energy difference and

Quantity	Experiment	1-site potential	(Obs - calc)
$(1,0,0,1^-)$ $\leftarrow (1,0,0,0)$	2.4640 ± 0.01 cm^{-1}	2.1320 cm^{-1}	0.3320 cm^{-1}
$2B(v_2 = 0)$	4143.5196 ± 1 MHz	4164.2171 MHz	-20.6975 MHz
$(1,1,0,0)$ $\leftarrow (1,0,0,0)$	11.912 ± 0.02 cm^{-1}	21.0704 cm^{-1}	-9.1584 cm^{-1}
$-24D(v_2 = 0)$	-1.5222 MHz	-1.6261 MHz	0.1039 MHz

Table 2.4: Key experimental spectroscopic quantities and those calculated from the 1-site dispersion potential with $K_\rho = 4.5$ and $\gamma = 15.0\ a_0^2$. Uncertainties in the experimental values are given.

B-rotational constant, although not within experimental uncertainty, indicate that the radial and angular position of the global minimum is close enough for the start of a least squares fit. Most noticeable however is the difference in energy between the $(1,1,0,0)$ (the first excited bending vibration) and $(1,0,0,0)$. The error is almost twice as large as the actual transition energy thus indicating that the anisotropy of the potential is far from correct. This can be attributed to the barriers to rotation around both the carbon and oxygens ends being too large.

Despite analysing potentials using many different values of the two parameters, qualitative agreement could not be achieved between the global minimum and saddle points of the single site systematic potential and the *ab initio* potentials. The deficit of dispersion at the ends of the CO monomer could not be rectified. A least squares fit of the one site potential to experiment went in an unphysical direction as the potential was too far from the 'true' potential and there was not a parameter in the fit which could lower the barriers to rotation. The best agreement was achieved with $K_\rho = 4.5$ and $\gamma = 15.0\ a_0^2$, but as discussed above this is not a good potential from which to commence a fit to experimental data as the first excited bending state is far from the experimental value.

The formulation of the repulsion used here worked well for $ArCO_2$ therefore it is most probable that the dispersion is in error. Additionally a two-site

Feature	Ar–CO	Global minimum	CO–Ar
Energy / cm^{-1}	61.09	93.36	74.44
Position (R/ Å, θ/°)	(4.52, 0)	(3.73, 80)	(4.02, 180)

Table 2.5: Key features of the potential resulting from the two-site dispersion model with $K_\rho = 4.5$ and $\gamma = 15.0\ a_0^2$. Ar–CO and CO–Ar refer to the saddle point at the carbon end and the minimum at the oxygen end respectively.

expansion of the dispersion was required for $ArCO_2$ and so it is realistic to have one for ArCO also.

2.5.2 Two-site dispersion model

A number of different combinations of values for S, a, S_1, γ and K_ρ were investigated. As the single site dispersion model was centred at the centre of polarisability, S_1 is used to move the dispersion expansion to the centre of polarisability and is set equal to $0.559\ a_0$. The optimum position of the partitioned dispersion sites is not clear. Perhaps the most obvious choice would be the nuclei so $S = 2.132\ a_0$, the CO bond length and $a = -0.690650$. Again a repulsion factor of $K_\rho = 4.5$ and a dispersion ratio of $\gamma = 30.0\ a_0^2$, which were appropriate for the $ArCO_2$ complex, were found to give a potential that was too deep compared to the *ab initio* potentials. The best single site model was obtained with $K_\rho = 4.5$ and $\gamma = 15.0\ a_0^2$ so these are adopted initially for the two site model also. For both sites the ratio γ is constrained to have the same value. This gives,

$$\begin{aligned} C_6^{0,C} &= 53.83\ E_h a_0^6, \qquad C_6^{0,O} = 17.84\ E_h a_0^6 \\ C_6^{2,C} &= 0.22\ E_h a_0^6 \quad \text{and} \quad C_6^{2,O} = 6.38\ E_h a_0^6 \end{aligned} \tag{2.30}$$

as the partitioned dispersion coefficients. The resulting potential is plotted in Figure 2.6 and the key features given in Table 2.5.

Comparing the values given in Table 2.5 with those in Table 2.2 reveals that closer qualitative agreement with the *ab initio* potentials is achieved with the two site model compared with the single-site potential model.

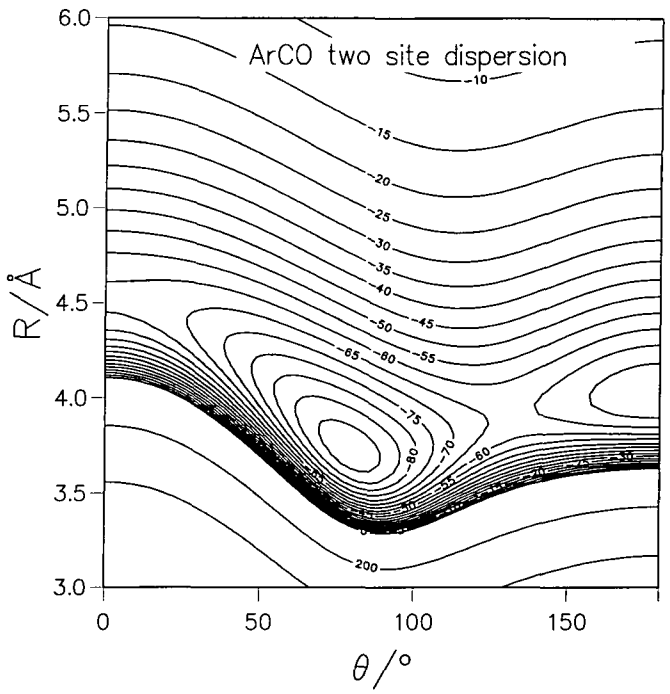

Figure 2.6: The two-site dispersion model of the ArCO potential with $K_\rho = 4.5$ and $\gamma = 15.0\ a_0^2$ and the dispersion sites on the carbon and oxygen nuclei. Contours are labeled in cm^{-1}.

1. The global minimum corresponds to an approximately T-shaped geometry. It is however shallower than the *ab initio* potentials given in Table 2.2 although well within the 10 cm^{-1} error bars required. The radial distance at the global minimum is between the values from the *ab initio* potentials.

2. The saddle point at the carbon end is a shallower than the *ab initio* potentials but only 7 cm^{-1} shallower than Ref. 67. So the barrier to rotation around the carbon end is 4 cm^{-1} greater than Ref. 67 and 6 cm^{-1} greater than Ref. 104. The radial distance here is also in good agreement with the *ab initio* potentials.

3. The minimum energy at $\theta = 180°$ is 8 cm^{-1} less than that of Ref. 67. The corresponding radial distance at the global minimum is in good agreement with the *ab initio* potentials. The difference in energy between the global minimum and the minimum at 180° is 18.9 cm^{-1} which compares well with the 19.9 cm^{-1} and 13.6 cm^{-1} from the *ab initio* potentials. How-

ever the two-site potential has a secondary minimum at the oxygen end which none of the *ab initio* potentials have.

4. The difference in energy between the saddle point at 0° and the secondary minimum at 180° is approximately -13 cm^{-1} for the two-site potential, which compares well with the -14.4 cm^{-1} and -6.1 cm^{-1} for the potentials calculated by Shin *et al.* [67] and the Jansen [104] respectively. Note that, unlike the single site potentials, the relative depth of the saddle points are the same way around as the *ab initio* potentials with the oxygen end deeper than the carbon.

5. The difference in R corresponding to the minimum energy at 0° and the minimum energy at 180° is 0.5 Å which again is in qualitative agreement with, 0.54 Å from the potential obtained by Shin *et al.* [67].

The secondary minimum at the oxygen end of the two-site potential suggests that the dispersion site placed on the oxygen nucleus was displaced a little too far from the centre of polarisability, creating a 'hole' due to an excess of dispersion compared to repulsion. This secondary minimum should be removed quite easily in the least-squares fit by moving the dispersion site at the oxygen nucleus toward the centre of mass slightly. Conversely the barrier to rotation around the carbon end is a little too high suggesting that a little extra dispersion is needed at the carbon end.

The same key spectroscopic quantities used to assess the quality of the single-site potential are given in Table 2.6 for the two-site potential. Although the B-rotational constant has deteriorated relative to the single-site model the $K = 0$ bending state has improved significantly with a 1.8 cm^{-1} discrepancy between experiment and theory.

The two-site potential agreed qualitatively with the *ab initio* potentials; the energies at the key features were within 10 cm^{-1} and the radial distances within 0.1 Å. Improved agreement was also achieved with the $K = 0$ bending state. Therefore I believed this was a good potential from which to commence a fit to experimental data.

Quantity	Experiment	2-site potential	(Obs - calc)
$(1,0,0,1^-)$ $\leftarrow (1,0,0,0)$	2.4640 ± 0.01 cm^{-1}	2.3319 cm^{-1}	0.1321 cm^{-1}
$2B \approx$ $E(1,0) - E(0,0)$	4143.5196 ± 1 MHz	4005.2453 MHz	138.2743 MHz
$(1,1,0,0)$ $\leftarrow (1,0,0,0)$	11.912 ± 0.02 cm^{-1}	13.7387 cm^{-1}	-1.8267 cm^{-1}
$-24D \approx (E(2,0)-$ $E(1,0)) - 2B$	-1.5222 MHz	-2.0743 MHz	0.5521 MHz

Table 2.6: Key experimental spectroscopic quantities and those calculated from the 2-site dispersion potential with $K_\rho = 4.5$ and $\gamma = 15.0\ a_0^2$. Uncertainties in the experimental values are given.

2.6 The fitting procedure

2.6.1 The least-squares fit

The I-NoLLS program [123,124] was employed to fit the potential to the experimental data. I-NoLLS is an interactive nonlinear least-squares fitting program which allows the user to apply physical insight to guide a fit. To this end the user can choose which observables and parameters to include in the fit and alter them at each step if desired.

The goal of obtaining a potential energy surface for the ArCO complex using the systematic model approach, described above, that agrees with experiment has not been realised. Many different approaches to the determination of the potential parameters from the experimental data using the method of least-squares were adopted. None of these approaches worked. While improved agreement with experiment was possible for some states, a deterioration in agreement with other states was observed. Some of the approaches to the problem are outlined below with problems encountered and action taken to overcome them. Many more problems were encountered and approaches attempted than will be discussed below.

The two-site dispersion potential with $K_\rho = 4.5, \gamma = 15.0\ a_0^2$, $S = 2.132$

a_0, $a = -0.690650$ and $S_1 = 0.559\ a_0$ was used as the starting point. Following comparison of the two-site dispersion potential and the *ab initio* potentials given in Section 2.5.2, the amount of dispersion moved toward the oxygen and carbon nuclei was thought to be approximately correct and should need only small adjustments. Therefore initially only K_ρ and γ were allowed to vary in the fit. Recall that γ controls how much C_8 dispersion there is at each site without changing C_6; K_ρ controls the amount of repulsion.

The best potential resulting from such a fit is plotted in Figure 2.7. The global minimum is located at $R = 3.66$ Å $\theta = 79°$ and $\epsilon = -92.73$ cm^{-1}. This is shallower than the unfitted surface or the *ab initio* surfaces. The barrier to rotation around the carbon end has been reduced to 30 cm^{-1}. The secondary minimum at the oxygen end has become shallower with a difference in energy between the global and secondary minimum of 19.23 cm^{-1}. This is in close agreement with the 19.9 cm^{-1} obtained by Jansen [104].

The spectroscopic quantities which provide the most information about the potential are given in Table 2.7. A small improvement was seen in the energy of the $K = 0$ bending state. A significant improvement was also seen in the ground state B-rotational constant. The centrifugal distortion constants are too large, probably because of the secondary minimum at $\theta = 180°$. Before doing the fit it was not clear whether the secondary minimum would be a problem or not. However from looking at the spectroscopic quantities quoted in Table 2.7, it is clear that the potential is unphysical. So to remove the secondary minimum, S, the distance between the dispersion sites, was allowed to be determined by the data.

A fit involving K_ρ, γ and S with a held constant, invariably tried to increase S. From the *ab initio* potentials and the above spectroscopic data it is clear that the secondary minimum needs to be removed. This necessitates a reduction of S. Excluding the $K = 0$ bending state from the fit allows S to be reduced. However this leads to a marked deterioration in the bending frequency which when introduced into the fit causes S to be increased again.

The potential with the dispersion sites placed on the nuclei of the CO monomer, was thought to be a good starting potential for a fit to experiment. I thought that the secondary minimum would be removed easily which was not

Energy difference	Experiment	$K_\rho = 3.134$ and $\gamma = 8.538\ a_0^2$	(Obs−Calc)
$(1,0,0,1^-)$ $\leftarrow (1,0,0,0)$	2.4640 ± 0.01 cm^{-1}	2.3714 cm^{-1}	0.0926 cm^{-1}
$(1,0,0,1^+)$ $\leftarrow (1,0,0,1^-)$	-129.9460 ± 6.0 MHz	-112.6637 MHz	-17.2823 MHz
$(1,1,0,0)$ $\leftarrow (1,0,0,0)$	11.9120 ± 0.02 cm^{-1}	13.0002 cm^{-1}	-1.0882 cm^{-1}
$(1,0,1,0)$ $\leftarrow (1,0,0,0)$	18.0971 ± 0.02 cm^{-1}	17.1021 cm^{-1}	0.9950 cm^{-1}
$2B(v_2 = 0)$	4143.5196 ± 4.0 MHz	4150.3469 MHz	-6.8273 MHz
$2B(v_2 = 0) -$ $2B(v_2 = 1)$	229.3762 ± 4.0 MHz	414.3115 MHz	-184.9353 MHz
$-24D(v_2 = 0)$	-1.5222 ± 0.015 MHz	-2.4556 MHz	0.9334 MHz
$-24D(v_2 = 1)$	-1.1904 ± 0.03 MHz	-3.9372 MHz	2.7468 MHz

Table 2.7: Calculated energy level differences for the two parameter two-site dispersion potential, with $K_\rho = 3.134$, $\gamma = 8.538\ a_0^2$, $S = 2.132\ a_0$, $a = -0.690650$ and $S_1 = 0.559\ a_0$. Experimental values are quoted with the uncertainties used for the least squares fit.

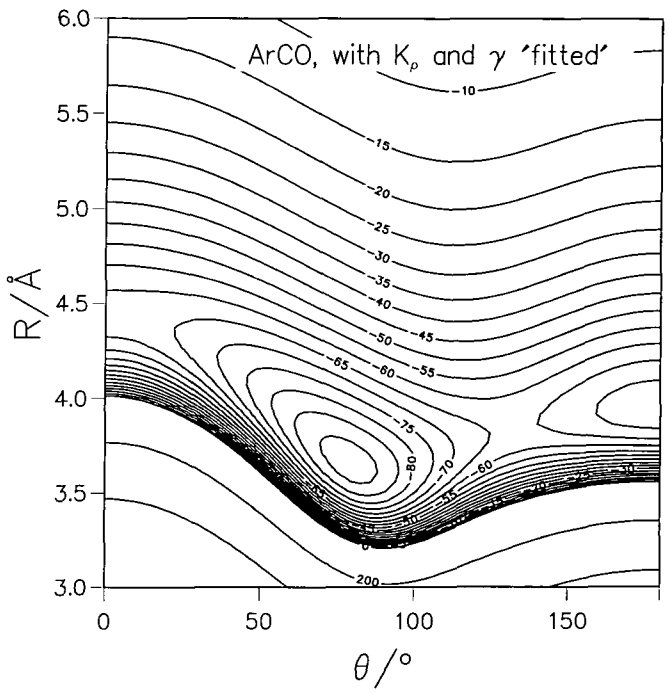

Figure 2.7: A two parameter fit of the ArCO two-site dispersion potential with $K_\rho = 3.134$, $\gamma = 8.538\ a_0^2$, $S = 2.132\ a_0$ and $a = -0.690650$. Contours are labeled in cm^{-1}.

the case. The initial values of the potential parameters were inappropriate. Improved parameter values, that could be used to calculate a potential that gave qualitative agreement with the *ab initio* potentials and did not have an artificial secondary minimum, were required.

To obtain improved initial potential parameters, a fit to the MP4 interaction energy data computed by Shin *et al.* [67] was attempted. Their potential was in qualitative agreement with experiment which meant that the shape of the potential was reasonably close to that of the 'true' surface. If the shape of the two-site potential was similar to that of the potential calculated by Shin *et al.* [67], it should be possible to obtain agreement with experiment. Secondly, by fitting to the *ab initio* data rather than experimental data all regions of the potential can be adjusted. Care was taken to ensure that the repulsive wall did not dominate the fit. Exact agreement was not possible. By adjusting a as well as S, K_ρ and γ the secondary minimum was not removed. The parameters which gave the smallest sum of squares were, $K_\rho = 4.939$, $\gamma = 19.033\ a_0^2$, $S = 2.305\ a_0$

and $a = -0.626230$ which meant the partitioned dispersion coefficients were, $C_6^{0,C} = 48.88\ E_h a_0^6$, $C_6^{0,O} = 22.78\ E_h a_0^6$, $C_6^{2,C} = 0.12\ E_h a_0^6$ and $C_6^{2,O} = 6.48\ E_h a_0^6$. The $K = 0$ bending and stretching frequencies calculated with this potential, differ significantly from experiment. The energy of the $(1,1,0,0)$ state and the $(1,0,1,0)$ state were $1.17\ \text{cm}^{-1}$ and $2.31\ \text{cm}^{-1}$ greater respectively, than experiment. The aim of fitting to the MP4 data was, to obtain a potential which had a single minimum and gave qualitative agreement with the potential features of Ref. 67 and that could be used as a starting point for a fit to experimental data. This was not possible, so a different approach to the problem of how to fit the two-site potential to the experimental data was required.

The sum of the C_6 coefficients is controlled by the dipole polarisabilities, α. The ratio of the C_6 coefficients is controlled by the dipole-quadrapole polarisabilities, $A_{||}$ and $A_{\perp}$. The values used for $A_{||}$ and $A_{\perp}$ were computed using *ab initio* theory [118]. Therefore they are subject to the errors associated with incomplete basis sets and limited correlation treatment. Furthermore, they are origin dependent. Maroulis calculated $A_{||}$ and $A_{\perp}$ relative to the centre of mass. Hence they may slightly underestimate the dispersion. To compensate for these minor errors the values of $A_{||}$ and $A_{\perp}$ were floated in the least squares fit. The initial values were taken as the *ab initio* values. As the errors were thought to be small, only minor adjustments to their values were thought to be required.

The data guided the fit such that $A_{||}$ and $A_{\perp}$ deviated from the *ab initio* values by up to 11 $e^2 a_0^3 E_h^{-1}$! Any potential resulting from such a fit of the potential parameters was unphysical.

In all the above fits to experiment there was a common problem which was impossible to solve. The 95% confidence limit on γ was always very high. Typically $\gamma \approx 15.0\ a_0^2$ but the 95% confidence limit ranged from $2 - 15$. This had two possible implications: the first was that γ was under-determined and the second was that the starting value for γ was so far from the true value that it was impossible to determine.

Given all the problems experienced in the fitting procedure perhaps the functional form used for the component parts of the potential was not appropriate for ArCO.

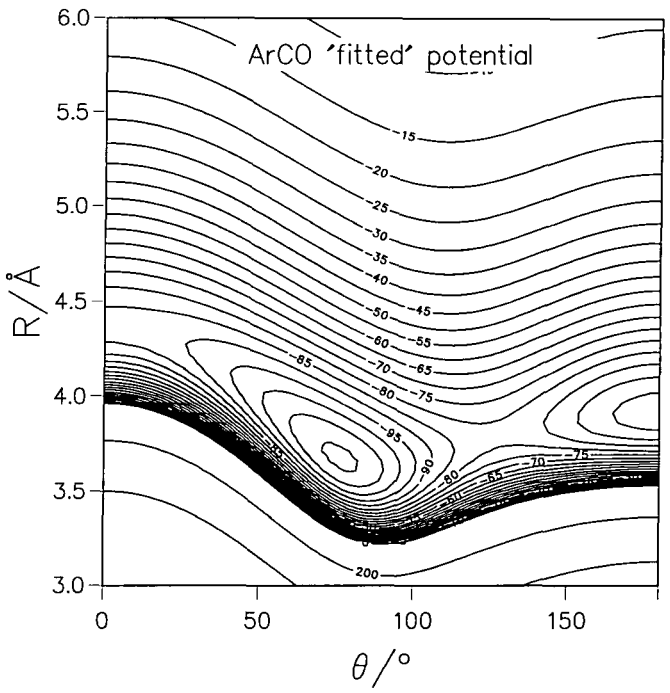

Figure 2.8: A 'fitted' ArCO two-site dispersion model potential with $K_\rho = 4.320714$, $S = 2.289438\ a_0$, $\gamma = 18.606908\ a_0^2$, $a = -0.626230$. Contours are labeled in cm^{-1}.

2.6.2 The 'fitted' potential

To give an indication of how poor the two-site potentials were, the potential that gave closest agreement with experiment (the one with the smallest sum of squares) is reported here. The fitted parameters are,

$$\begin{aligned} K_\rho &= 4.320714 \quad (0.416949), & S &= 2.289438 a_0 \quad (.034435), \\ \gamma &= 18.606908 a_0^2 \quad (2.050452) \quad \text{and} & a &= -0.626230 \quad (.011382), \end{aligned}$$

where the 95% confidence limits are given in parentheses. S_1 was held fixed at $0.559\ a_0$. The dispersion sites are located at $-0.875\ a_0$ and $1.414\ a_0$ along the z-axis, with $C_6^{0,\mathrm{C}} = 48.91\ E_h a_0^6$, $C_6^{0,\mathrm{O}} = 22.75\ E_h a_0^6$, $C_6^{2,\mathrm{C}} = 0.09\ E_h a_0^6$ and $C_6^{2,\mathrm{O}} = 6.51\ E_h a_0^6$. As can be seen from Figure 2.8, the potential has two minima. The key potential features are: the global minimum, located at

$$R = 3.67\text{Å}, \quad \theta = 76°, \quad \epsilon = -111.22\mathrm{cm}^{-1};$$

the saddle point at the carbon end, located at

$$R = 4.37\text{Å}, \quad \theta = 0°, \quad \epsilon = -87.17\mathrm{cm}^{-1};$$

the secondary minimum, located at

$$R = 3.91\text{Å}, \quad \theta = 180°, \quad \epsilon = -97.95\text{cm}^{-1}.$$

The features of the potential will now be considered individually below.

The global minimum. The position of the global minimum is in good agreement with the *ab initio* potentials at 2.6 cm^{-1} deeper and 0.01 Å closer to the OCS than the Jansen potential [104]. Compared to the unfitted potential described in Section 2.5.2 it is 17.9 cm^{-1} deeper and 0.06 Å closer in. The global minimum although located at an approximately T-shaped geometry is closer to the carbon end than the oxygen, the inverse of the *ab initio* surfaces.

The secondary minimum. None of the potentials in the literature have a secondary minimum at $\theta = 180°$. This suggests that the initial potential was unphysical. I thought the secondary minimum would be removed during the fit to experimental data. From the potential plot, Figure 2.8, it is clear that the minimum has not been removed. The dispersion site at the oxygen end has been brought in from the oxygen nucleus by 0.04 a_0 whereas the dispersion at the carbon end has been moved out along the positive z-axis by 0.20 a_0. The transition state between the two minima is approximately 81.28 cm^{-1} deep. The binding energy of the system is close in energy to the transition state at 82.66 cm^{-1}. This suggests that the centrifugal distortion constants calculated from the potential will be contaminated as the wave function will sample the artificial secondary minimum.

Barriers to rotation. The barrier to rotation around the carbon end is 24 cm^{-1} which is slightly lower than either the potential calculated by Shin *et al.*, 28 cm^{-1} [67], or by Jansen, 26 cm^{-1} [104]. The difference in energy between the global minimum and the minimum energy at 180° is 13.3 cm^{-1} which compares well with the 13.6 cm^{-1} from Ref. 67 and 19.9 cm^{-1} from Ref. 104. However, due to the secondary minimum, the barrier to rotation is actually 29.9 cm^{-1} greater than this. The difference in the value of

R corresponding to the minimum energy at 0° and 180° is 0.46 Å. This is reduced compared to the unfitted potential and literature surfaces.

Comparison with experiment. The experimental values of the energy differences used in the least-squares fit are listed in Table 2.8 along with those calculated from the 'fitted' two-site potential. Reasonably good agreement is seen for most energy differences. The largest deviation from experiment is 0.62 cm^{-1} for the difference between the $(1,1,0,0)$ and $(1,1,0,1)$ states. The $(1,0,1,1) \leftarrow (1,0,1,0)$ energy difference is also too large at -0.58 cm^{-1} which indicates that the radial behaviour of the potential higher up the well is not well reproduced. The difference between the observed and calculated value for the asymmetry splitting of the doubly excited stretching state was -630.35 MHz is also in poor agreement with experiment. The quantities used to approximate the rotational and centrifugal distortion constants are given in Table 2.9. The ground state rotational constant is in good agreement with experiment deviating by just 8.9395 MHz, but the $v_2 = 1, K = 0$ rotational constant is not. The difference between the experimental and calculated values for this constant was -229.37 MHz. That means the difference between the two rotational constants calculated from the two-site potential is almost double that from experiment. Both centrifugal distortion constants are excessively large indicating that they have indeed been contaminated by the wave function sampling the artificial secondary minimum. The calculated second virial coefficients, given in Table 2.10, are in close agreement with experiment indicating that the potential well depth is approximately correct.

2.7 Discussion and Conclusions

Given a comparison of the initial, unfitted potential and the potentials in the literature it is clear that the systematic model potential is unphysical. The secondary minimum, which no other ArCO potential in the literature has, is a problem which can not be overcome even when the potential parameters are

Energy difference	Experiment	'Fitted' 2-site surface	(Obs - Calc)
$(1,0,0,1^-)$ $\leftarrow (1,0,0,0)$	2.4640 ± 0.01 cm^{-1}	2.4950 cm^{-1}	$-.0310$ cm^{-1}
$(1,0,0,1^+)$ $\leftarrow (1,0,0,1^-)$	-129.9460 ± 6.00 MHz	-110.9626 MHz	-18.9834 MHz
$(1,0,0,2^-)$ $\leftarrow (1,0,0,1^-)$	6.7260 ± 0.02 cm^{-1}	6.8248 cm^{-1}	$-.0988$ cm^{-1}
$(1,0,0,2^+)$ $\leftarrow (1,0,0,2^-)$	-873.1530 ± 40.00 KHz	-285.8940 KHz	-587.2590 KHz
$(1,1,0,0)$ $\leftarrow (1,0,0,0)$	11.9120 ± 0.02 cm^{-1}	11.9212 cm^{-1}	$-.0092$ cm^{-1}
$(1,0,1,0)$ $\leftarrow (1,0,0,0)$	18.0971 ± 0.02 cm^{-1}	18.3952 cm^{-1}	$-.2981$ cm^{-1}
$(1,1,0,1)$ $\leftarrow (1,1,0,0)$	5.1830 ± 0.02 cm^{-1}	5.8068 cm^{-1}	$-.6238$ cm^{-1}
$(1,1,0,1^+)$ $\leftarrow (1,1,0,1^-)$	-995.2210 ± 15.00 MHz	-929.2213 MHz	-65.9997 MHz
$(1,0,1,1)$ $\leftarrow (1,0,1,0)$	8.1636 ± 0.03 cm^{-1}	8.7471 cm^{-1}	$-.5835$ cm^{-1}
$(1,0,1,1^+)$ $\leftarrow (1,0,1,1^-)$	-47.6130 ± 10 MHz	-582.7411 MHz	-630.3541 MHz

Table 2.8: Calculated energy level differences for the 'fitted' two-site dispersion potential, with $K_\rho = 4.320714$, $\gamma = 18.606908\ a_0^2$, $S = 2.289438\ a_0$, $a = -0.626230$.

Constant	Experiment	'Fitted' 2-site	(Obs−Calc)
$2B(v_2 = 0)$	4143.5196 ± 1.0	4134.5801	8.9395
$2B(v_2 = 0) - 2B(v_2 = 1)$	229.3762 ± 4.0	449.8101	−220.4339
$-24D(v_2 = 0)$	-1.5222 ± 0.015	−2.5242	1.0020
$-24D(v_2 = 1)$	-1.1904 ± 0.03	−2.5082	1.3178

Table 2.9: Calculated rotational and centrifugal distortion constants for the two-site potential, with $K_\rho = 4.320714$, $\gamma = 18.606908\ a_0^2$, $S = 2.289438\ a_0$, $a = -0.626230$. Experimental values are quoted with the uncertainties used for the least squares fit.

B(T/K)	Experiment	'Fitted' 2-site	(Obs−Calc)
$B(296.15$	-11.9000 ± 1.5	−13.0393	1.1393
$B(353.15)$	-2.1000 ± 2.0	−3.4247	1.3247
$B(413.15$	5.2000 ± 3.0	3.4315	1.7685
$B(463.15$	9.3000 ± 3.0	7.5917	1.7083

Table 2.10: Calculated second virial coefficients for the two-site potential, with $K_\rho = 4.320714$, $\gamma = 18.606908\ a_0^2$, $S = 2.289438\ a_0$, $a = -0.626230$. Experimental values are quoted with the uncertainties used for the least squares fit.

fitted to *ab initio* points. A surface of spectroscopic accuracy proved impossible to obtain because the initial surface was not in close enough agreement with experiment, or close enough to the 'true' potential.

Reasonable agreement with experiment was obtained for some of the energy level differences. However the discrepancy with the centrifugal distortion constants indicate that there is a problem with the shape of the potential.

The source of the problem must be due to the repulsion, dispersion or induction. The model of the repulsion is the same as used for HeHCN and $ArCO_2$, both of which were successful [43, 114]. Therefore the repulsion is unlikely to be in error. The problem is also unlikely to be due to the induction. The error in excluding an explicit induction term in the potential model is small compared to the errors with the surface.

I think the repulsion is reasonably well modelled. The *ab initio* computational method and the basis set used were the same as that used for $ArCO_2$ which worked well. The functional form adopted was successfully applied to HeHCN and so is unlikely to be the cause of the error. The difference arises with the dispersion. There are two problems, where to place the dispersion site(s) and how much dispersion should be placed there. Both the single-site and two-site models were centred at the centre of polarisability. A single-site dispersion model was found to be inadequate. Placing the dispersion site at the centre of polarisability simplifies the model, and odd-order coefficients are not required. The barriers to rotation however were too high and the relative depths of the saddle points were inversed relative to the *ab initio* surfaces. In addition $A_\perp$ and $A_{||}$ were calculated relative to the centre of mass and so may not pick up all the dispersion.

The potential appears to have insufficient dispersion between the carbon and oxygen nuclei and perhaps a little excess dispersion at the carbon end. This is indicated by the dispersion site at the carbon end being forced outside the molecule, whereas the dispersion site at the oxygen end is pulled into the molecule in the fit. This is also consistent with the study by Stone and Price [125] which found the carbon end of CO to be more polarisable than the oxygen end.

The other thing to consider is γ, the ratio of C_6 to C_8, which was very poorly

determined by the experimental data. This can not be attributed to the correlation of γ with any other parameter in the fit but is more probably due to either the potential being too far from the true picture or the experimental data not being of the correct form to determine γ. This parameter controls the amount of dispersion on each site without affecting the C_6 coefficients. The large 95% confidence limit also indicates that the dispersion is poorly described for the system. Maybe a third site is required but this increases the complexity of the problem. An alternative approach which may be beneficial would be to use a distributed dispersion expansion rather than a localised one [3].

I hoped the systematic approach would work well for ArCO but agreement with experiment was not obtained for the functional form used here. One constraint therefore to applying the systematic model to different systems is the choice of functional form for each contribution to the potential. A good functional form is necessary and is not necessarily transferable between similar systems.

In the next chapter the supermolecular approach is considered.

CHAPTER

3

The Ar–CO Potential: morphed surface

3.1 Introduction

Ab initio methods have been used to calculate many of the potentials that give qualitative agreement with experiment for the ArCO molecule. These calculations however are computationally expensive demanding many CPU hours and large amounts of memory. Typically, computation of the interaction energy using MP4 with an aug-cc-pVTZ basis would take 10 hours 20 minutes for one molecular configuration with the GAUSSIAN package [111] on a Silicon Graphics origin 2000 computer. To calculate an entire surface requires hundreds of such computations. Shin *et al.* [67] used 77 which equates to 33 days CPU time for the calculation described above. The basis set used for such a computation is large but not complete. Consequently the calculation is prone to basis set superposition error. The basis set centred on one of the monomers

borrows some of the basis set from the other monomer to complete the basis and vice versa. So in addition to the single point calculation at each point a further two calculations at each point are required to correct for the error due to basis set superposition. This results in 66 days CPU time to calculate the basis set superposition error corrected points. Despite the computational expense the surface obtained only approaches spectroscopic accuracy.

The systematic model procedure to obtain a potential is computationally inexpensive compared to supermolecular calculations. As shown in Chapter 2 however I was unable to obtain a potential energy surface for the Ar–CO system that gave good agreement with experiment, based upon the systematic model. Recently Meuwly and Hutson [83] developed the morphing procedure and applied it to *ab initio* potentials of the NeHF molecule. Morphing equates to scaling the energy and the co-ordinates in an angle dependent way in order to obtain agreement with the experimental data. The general shape of the potential obtained from the *ab initio* computations is thought to be good and so is retained but small adjustments to specific features of the potential which are not well determined by the *ab initio* computations are made based on the experimental data. Some groups who compute potential energy surfaces scale the energy [56, 104] and others the co-ordinates [126–128] but to my knowledge nobody scales both. By scaling both the energy and the co-ordinates the depth of the potential and the position of the key features can be altered if the experimental data demands.

Here the 77 MP4 points calculated by Shin *et al.* [67] are used to compute a surface which is then morphed to obtain agreement with experiment for the Ar–CO system. The points computed by Shin *et al.* [67] are chosen rather than those computed by Jansen [104] as Jansen did not publish his data points.

3.2 Obtaining the unmorphed potential

Shin *et al.* [67] used the Jacobi co-ordinate system, as discussed in Chapter 2. Interaction energies were calculated on a grid of seven equally spaced points in θ between $0°$ and $180°$ and nine equally spaced points in R between 3.00 and 5.00 Å, with two extra points at 5.50 and 6.00 Å. The CO bond length

was fixed at 1.128 Å. A contracted $[17s13p/8s6p]$ basis was employed for argon and $[14s10p/7s5p]$ for carbon and oxygen. Both basis sets were augmented with $3d$ functions. Bond functions, $[3sp, 2d]$, were placed half way along the R vector. Although these are large basis sets they are not complete and therefore to correct for the error due to basis set superposition, Shin *et al.* employed Boys and Bernardi's counterpoise correction method [62, 129].

3.2.1 Interpolation scheme

The potential was expanded in terms of Legendre polynomials

$$V(R,\theta) = \sum_{\lambda} C_{\lambda}(R) P_{\lambda}(\cos\theta). \tag{3.1}$$

The expansion coefficients $C_{\lambda}(R)$ however were unknown and therefore needed to be determined. Equation 3.1 can be written in matrix form for each value of R at which the potential is known,

$$\mathbf{V} = \mathbf{CP}, \tag{3.2}$$

where $\mathbf{V}$ is a vector of values of the potential, $\mathbf{C}$ is a vector of expansion coefficients at constant R and $\mathbf{P}$ is a $(\lambda + 1)$ by N_{θ} matrix. $\mathbf{P}$ consists of values of the Legendre polynomials up to order λ at the different values of θ. N_{θ} is the number of points in θ at which the potential is known. By inverting the matrix $\mathbf{P}$, which is only possible if $N_{\theta} = \lambda + 1$, the equation

$$\mathbf{VP^{-1}} = \mathbf{C} \tag{3.3}$$

is obtained. This was solved at each value of R where the potential was known and the expansion coefficients, $C_{\lambda}(R)$ determined.

The reproducing kernel Hilbert space interpolation scheme, RKHS, developed by Ho and Rabitz [79], was used to interpolate between the expansion coefficients at constant λ. The inner product over R',

$$C_{\lambda}(R) = \langle q(R,R'), C_{\lambda}(R') \rangle \tag{3.4}$$

defined over the interval $[0,\infty)$, was inverted and the unknown expansion coefficient, $C_{\lambda}(R')$ at constant λ determined. $q(R,R')$ is the reproducing function of the form,

$$q^{n,m}(R,R') = n^2 R_l^{-(m+1)} B(m+1,n)\,{}_2F_1(-n+1, m+1, n+m+1; \frac{R_s}{R_l}),$$

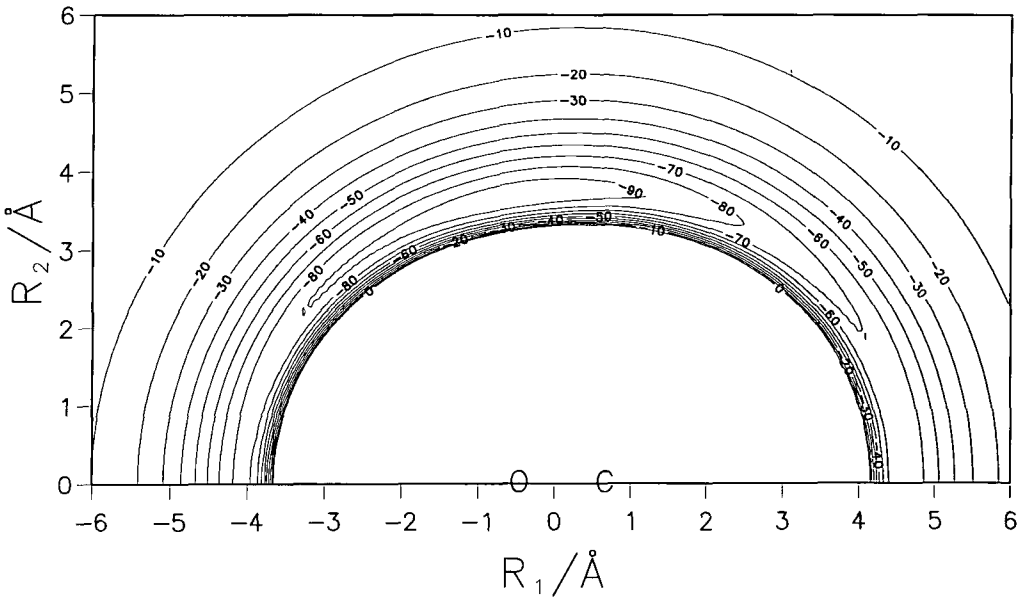

Figure 3.1: Plot of the unmorphed Ar–CO potential using MP4 points calculated by Shin *et al.* [67]. Contours are labeled in cm^{-1}.

where $B(a, b)$ is the beta function and ${}_2F_1(a, b, c, z)$ is a hypergeometric function. The subscripts l and s refer to the larger and smaller of R and R'. In this way a continuous potential is obtained.

Shin *et al.* [67] also expanded the potential in terms of Legendre polynomials in the angular co-ordinate. In the radial co-ordinate they used cubic splines in place of the RKHS method adopted here. The RKHS scheme however can build in the correct long-range behaviour [79] for the potential and so is favoured over cubic splines here.

3.2.2 Unmorphed potential

The potential obtained in the manner described above is plotted in Figure 3.1. The potential is characterised by a global minimum close to the T-shaped configuration at -96.49 cm^{-1}, 3.722 Å and 98°. There is no secondary minimum at either of the linear configurations. There is one saddle point at -68.32 cm^{-1},

4.583 Å, 0° and a second at -83.10 cm^{-1}, 4.054 Å, 180°. The potential is quite flat in the region of the global minimum. The argon atom can rotate from $\theta = 92°$ to 104° and the energy changes by just 0.5 cm^{-1}. The barrier to rotation around the carbon end, 28.2 cm^{-1}, which is greater than around the oxygen end, 13.4 cm^{-1}, but both are quite low.

The global minimum is 12 cm^{-1} shallower than either the Jansen potential [104] or the potential calculated by Chałasiński *et al.* [106]. This was attributed to the lack of f-type functions in the basis sets [67] but the potential should serve as a good starting potential for the morphing procedure.

3.3 The morphing function

The functional form used to morph the surface is the same as that used by Meuwly and Hutson [83],

$$V_{\text{morph}}(R,\theta) = v(\theta)V_{\text{orig}}(\rho(\theta)\cdot R,\theta) \tag{3.5}$$

where

$$\begin{aligned}\rho(\theta) &= \sum_{\lambda}\rho_\lambda P_\lambda(\cos\theta) \quad \text{and}\\ v(\theta) &= \sum_{\lambda k} v_\lambda P_\lambda(\cos\theta).\end{aligned} \tag{3.6}$$

The parameters, v_λ and ρ_λ, are determined by a least squares fit to the experimental data. The scaling is applied to the radial co-ordinate and then the energy is scaled. In this way the point at which the interaction energy is zero, which may not correspond to the same molecular configuration for both the unmorphed and morphed surfaces, can be moved. If the scaling were reversed a problem would arise where the interaction energy was equal to zero.

The first terms in $\rho(\theta)$ and $v(\theta)$ are isotropic scaling terms. They can be used to adjust the well depth and the corresponding radial distance. The second term in $v(\theta)$ allows the minimum energy at the carbon end to be adjusted relative to the energy at the oxygen end. The third term adjusts the minimum energies at the two ends relative to the global minimum. So the higher order terms in $\rho(\theta)$ and $v(\theta)$ introduce anisotropic scaling.

The morphing function allows the surface to be bent and stretched by small amounts based on the experimental data but the general shape of the potential is retained. The amount of morphing, measured by the size and number of morphing parameters required to obtain agreement with experiment, will depend on the quality of the initial surface.

The experimental data used for the least squares fit were the same as those used for the systematic model in Chapter 2 where they were discussed extensively.

3.4 The morphed potentials

A number of different least-squares fits were performed to try to obtain a potential that was in agreement with experiment. Two morphed potentials are reported here. The first, the M1 surface, achieves agreement with experiment for all states, except the $(1,0,1,1)$ state and the corresponding asymmetry splitting. Only three parameters, v_0, v_1 and ρ_0 are required. The second uses 6 parameters, is in agreement for the $(1,0,1,1)$ state and will be referred to as the M2 surface.

The M1 morphing parameters are,

$$\begin{aligned} v_0 &= 1.270734\ (0.018706), \quad \rho_0 = 1.010160\ (0.000659), \\ v_1 &= 0.077066\ (0.006014), \end{aligned} \tag{3.7}$$

where the 95% confidence limits have been given in parentheses. The small deviation from unity of the radial scaling parameter implies that the radial dependence of the potential was quite well determined by the *ab initio* calculations in the lower part of the well. A greater amount of morphing however was required for the energy with both an isotropic and an anisotropic scaling parameter being employed. The magnitude of these parameters suggested that the binding energy was underestimated by the MP4 computations.

A plot of the M1 surface is given in Figure 3.2. It is characterised by a single minimum at -121.82 cm^{-1}, 3.691 Å, 94° which is still close to a T-shaped geometry. Like the unmorphed surface there are no local minima at the linear configurations. The saddle points are located at -92.08 cm^{-1}, 4.537 Å, 0° and

-99.20 cm^{-1}, 4.013 Å, 180°.

The lack of a secondary minimum is also evident from the plot of the minimum energy pathway, Figure 3.3. Note how the values of R along the minimum energy pathway differ very little between the unmorphed and M1 potentials (ρ_0 is close to 1.00). Likewise, although the potential is made considerably deeper, the shape of the curve along the minimum energy pathway does not change greatly between the unmorphed and M1 potentials.

The global minimum of the M1 surface is 25.3 cm^{-1} deeper than the unmorphed potential and 14 cm^{-1} deeper than the global minimum of the surfaces in Refs. 67, 106. Compared with the unmorphed surface, the saddle points of the M1 potential have been made 23.8 cm^{-1} deeper at the carbon end and 16.1 cm^{-1} deeper at the oxygen end. The discrepancy in the depth of the global minimum between the M1 surface and the potentials of Refs. 67 and 106 suggest that the M1 surface may be a little deep and so v_0 may be a little large. While the M1 potential has been made globally deeper relative to the unmorphed potential, the difference in the depth of the saddle points at 0° and 180°, 7.1 cm^{-1}, has been halved. Interestingly, the barrier to rotation around the carbon end has only increased by 1.5 cm^{-1} after morphing whereas the barrier to rotation around the oxygen end has increased from -13.4 cm^{-1} for the unmorphed surface to -25.7 cm^{-1} for the M1 surface. This suggests that the discrepancy in the potential at the oxygen end was greater than at the carbon. This conclusion can only be drawn however if the data used in the least-squares fit sample both the carbon and oxygen ends of the potential.

The wavefunctions for the Van der Waals bending and stretching states sample from 0° to 180° and so are sensitive to the relative depths of the two saddle points. After just one step with v_1 in the least squares fit, all the states corresponding to the Van der Waals motions had improved agreement with experiment. Before the inclusion of the v_1 parameter, the greatest discrepancy was with the $(1,0,1,1)$ state. Although agreement was improved on inclusion of the v_1 parameter, this state still had the largest deviation from experiment. As can be seen from the calculated experimental quantities given in Tables 3.1, 3.2 and 3.3, the M1 surface is in good agreement with experiment for all energy differences except for $(1,0,1,1^-) \leftarrow (1,0,1,0)$ and $(1,0,1,1^-) \leftarrow$

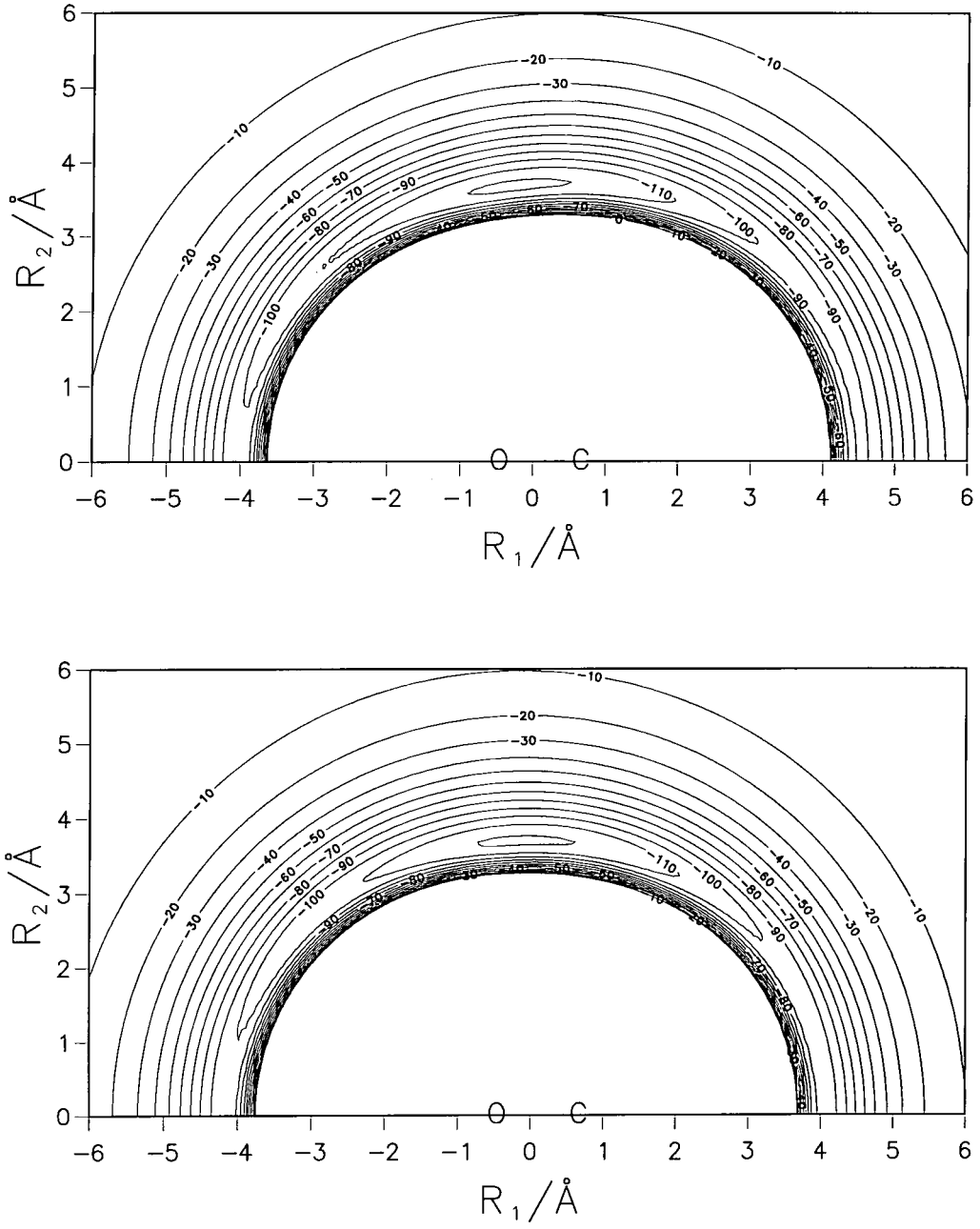

Figure 3.2: The top plot is of the M1 Ar–CO potential with $v_0 = 1.270734$, $v_1 = 0.077066$ and $\rho_0 = 1.010160$. The bottom plot is of the M2 Ar–CO potential with $v_0 = 1.275405$, $v_1 = 0.115892$, $v_2 = 0.011605$ and $\rho_0 = 1.025196$, $\rho_1 = 0.076428$, $\rho_2 = 0.026777$. Contours are labeled in cm^{-1}.

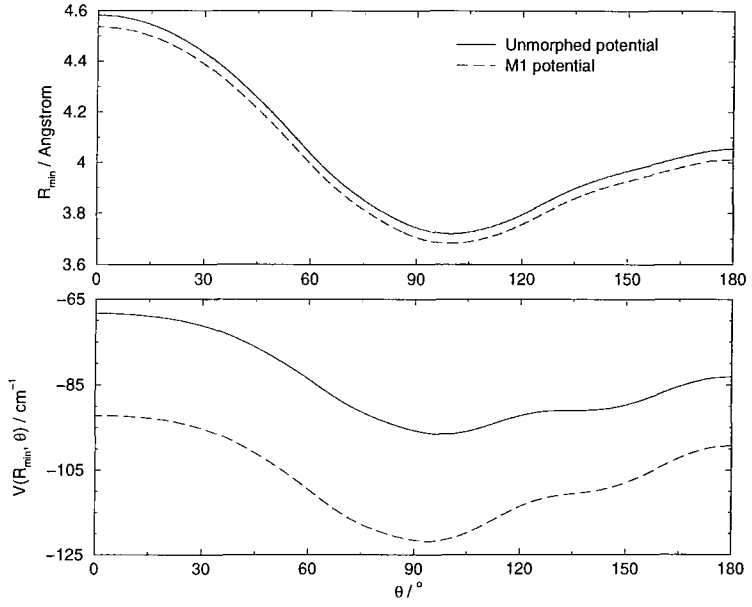

Figure 3.3: The bottom plot is of the minimum energy pathway along the Ar–CO unmorphed and M1 potentials. The top plot is of the values of R along the minimum energy pathway.

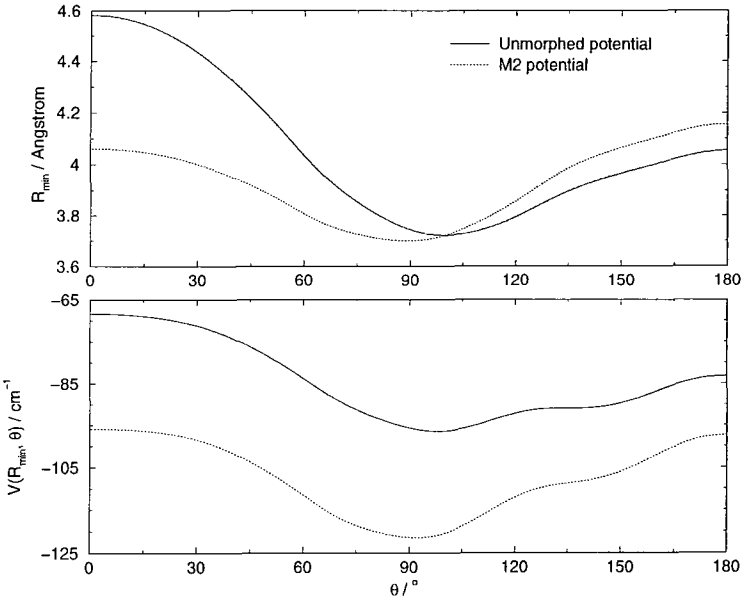

Figure 3.4: The bottom plot is of the minimum energy pathway along the Ar–CO unmorphed and M2 potentials. The top plot is of the values of R along the minimum energy pathway.

$(1,0,1,1^+)$. Compared to the unmorphed surface improved agreement is seen for all the states except the asymmetry splittings $(1,0,0,2^+) \leftarrow (1,0,0,2^-)$ and $(1,0,1,1^-) \leftarrow (1,0,1,1^+)$. The M1 surface is of comparable quality to the surface calculated by Jansen [104] which also had a 1.3 cm^{-1} discrepancy with the $(1,0,1,1)$ state. This state is the highest observed Van der Waals state and so gives information high up the potential well. If agreement with experiment is poor for this state it suggests that despite being in good agreement with experiment low in the potential well, the shape of the potential is less good higher up the potential. Interestingly there are two states 26.26 cm^{-1} above the $(1,0,0,0)$ state, one is the $(1,1,0,2)$ state and the other is the $(1,1,1,0)$ state. Therefore either, the potential has the wrong shape in this region or, the transition observed by König and Havenith [95] was misassigned. The first of these is the more likely.

A comparison of Figure 3.1 with Figure 3.2 shows that the general shape of the M1 and unmorphed surfaces are the same. While the potential has been made globally deeper, it has also become flatter.

From Table 3.2 one can see that the quantities approximately equal to the rotational constants for the M1 surface are in closer agreement with the experimental values than for the unmorphed surface. Therefore the curvature of the lower part of the potential well is good. This is confirmed by the good agreement with experiment of the $K = 0$ bending state and the $(1,0,0,1)$, $(1,0,0,2)$ states and corresponding asymmetry splittings. The second significant deviation of the M1 surface from experiment is in the centrifugal distortion constant of the $(1,1,0,0)$ state. Although improved agreement is achieved, it still deviates from experiment implying that the surface is not correct in this region.

Table 3.3 gives the second virial coefficients calculated from the unmorphed and M1 surfaces. For the unmorphed surface the second virial coefficients are larger than those measured by Schramm *et al.* [11] whereas for the M1 surface the second virial coefficients are smaller. The difference between the high and low temperature second virial coefficients give information about the well depth. The discrepancy between the calculated and measured coefficients suggest that the unmorphed potential is too shallow and the M1 potential is too deep. This is also implied by the ground state centrifugal distortion constant

Energy difference	Experiment	UM surface	M1 surface M2 surface
$(1,0,0,1^-)$	2.464 ± 0.01 cm^{-1}	3.002 cm^{-1}	2.519 cm^{-1}
$\leftarrow (1,0,0,0)$			2.438 cm^{-1}
$(1,0,0,1^+)$	-129.946 ± 6.0 MHz	-139.281 MHz	-129.087 MHz
$\leftarrow (1,0,0,1^-)$			-136.012 MHz
$(1,0,0,2^-)$	6.726 ± 0.02 cm^{-1}	7.129 cm^{-1}	6.778 cm^{-1}
$\leftarrow (1,0,0,1^-)$			6.728 cm^{-1}
$(1,0,0,2^+)$	-873.153 ± 40.0 KHz	-698.295 KHz	-559.891 KHz
$\leftarrow (1,0,0,2^-)$			-662.206 KHz
$(1,1,0,0)$	11.912 ± 0.02 cm^{-1}	9.795 cm^{-1}	11.984 cm^{-1}
$\leftarrow (1,0,0,0)$			11.638 cm^{-1}
$(1,0,1,0)$	18.097 ± 0.02 cm^{-1}	17.512 cm^{-1}	18.312 cm^{-1}
$\leftarrow (1,0,0,0)$			18.402 cm^{-1}
$(1,1,0,1^-)$	5.183 ± 0.02 cm^{-1}	6.708 cm^{-1}	5.314 cm^{-1}
$\leftarrow (1,1,0,0)$			5.264 cm^{-1}
$(1,1,0,1^+)$	-995.221 ± 6.0 MHz	-861.460 MHz	-1050.804 MHz
$\leftarrow (1,1,0,1^-)$			-1054.088 MHz
$(1,0,1,1^-)$	8.163 ± 0.03 cm^{-1}	5.985 cm^{-1}	6.695 cm^{-1}
$\leftarrow (1,0,1,0)$			7.387 cm^{-1}
$(1,0,1,1^-)$	-47.613 ± 6.0 MHz	-745.181 MHz	-1127.252 MHz
$\leftarrow (1,0,1,1^+)$			-1193.201 MHz

Table 3.1: Energy differences used in the least squares fit, experimental values and those calculated from the unmorphed (UM), M1 and M2 surfaces.

Transition	Experiment	UM surface	M1 surface
			M2 surface
$2B$	4143.520 ± 0.4 MHz	4016.052 MHz	4142.985 MHz
$v_2 = 0$			4143.432 MHz
$2B$	4327.896 ± 0.4 MHz	4185.549 MHz	4371.575 MHz
$v_2 = 1$			4372.407 MHz
$-24D$	-1.522 ± 0.03 MHz	-1.666 MHz	-1.347 MHz
$v_2 = 0$			-1.265 MHz
$-24D$	-1.190 ± 0.03 MHz	33.492 MHz	-0.898 MHz
$v_2 = 1$			-1.378 MHz

Table 3.2: Spectroscopic constants used in the least squares fit and those calculated using the unmorphed (UM), M1 and M2 morphed surfaces.

Virial coefficient	Experiment	UM surface	M1 surface
$B(T/K)$			M2 surface
B(296.15)	-11.900 ± 1.5	-6.867	-22.345
			-22.175
B(353.15)	-2.100 ± 2.0	1.993	-10.377
			-10.628
B(413.15)	5.200 ± 3.0	8.268	-1.895
			-2.445
B(463.15)	9.300 ± 3.0	12.042	3.227
			2.496

Table 3.3: The second virial coefficients [11] used in the least squares fit and those calculated from the unmorphed surface (UM), M1, M2 surfaces. Units are (cm^3 / mole).

which is too large for the unmorphed surface and too small for the M1 surface.

As expected the $K = 1$ stretching state was a challenge to determine accurately. The M1 potential achieved improved agreement with this state compared to the unmorphed but still has a large discrepancy between the experimental and calculated energy for the state. This suggests that higher order terms in the morphing function are required to improve agreement with experiment higher up the well. Therefore the second potential surface, M2, to be reported uses 3 energy scaling parameters and 3 co-ordinate scaling parameters,

$$\begin{aligned} v_0 &= 1.275405\ (0.132013), \quad \rho_0 = 1.025196\ (0.002636), \\ v_1 &= 0.115892\ (0.024030), \quad \rho_1 = 0.076428\ (0.017966), \\ v_2 &= 0.011605\ (0.024876), \quad \rho_2 = 0.026777\ (0.006919), \end{aligned}$$

where the 95% confidence limits are given in parentheses. The amount of morphing required for the radial co-ordinate is less than that required for the energy. Morphing the potential has altered the positions of the key features but not the general shape. The minimum is -121.52 cm^{-1} deep and located at, $R = 3.702$ Å, $\theta = 92°$. There are two saddle points at

$$\begin{aligned} R = 4.061\text{Å} \quad \theta &= 0° \quad \epsilon = -95.84\text{cm}^{-1} \text{ and} \\ R = 4.156\text{Å} \quad \theta &= 180° \quad \epsilon = -97.32\text{cm}^{-1}, \end{aligned} \tag{3.8}$$

but no local minima. The value of v_0 is similar for both the M1 and M2 surfaces. Likewise the well depth of the M2 surface is very close to that for the M1 surface. Table 3.3 shows that the second virial coefficients for the M1 and M2 surfaces also have similar magnitude. So by increasing the amount of morphing the depth of the global minimum has changed little and so remains a little deep.

The saddle point at the oxygen end of the M2 surface is 27.5 cm^{-1} deeper than the same saddle point of the unmorphed surface. The corresponding radial distance has been reduced by 0.52 Å. This compares to an increase of 14.2 cm^{-1} in the depth and a decrease of 0.10 Å in the corresponding radial distance of the saddle point at the oxygen end. This change in the potential results in a deeper saddle point at 180° than at 0° for the unmorphed surface which is the reverse of what is observed for either the unmorphed or the M1 potentials.

This difference is particularly apparent in the plot of the minimum energy pathway given in Figure 3.4. The lower plot shows that the barrier to rotation around the oxygen end of the M2 potential (25.7 cm^{-1}) is similar in magnitude to the barrier to rotation around the carbon end (24.2 cm^{-1}). These values compare to 13.4 cm^{-1} around oxygen and 28.2 cm^{-1} around carbon for the unmorphed surface. From the top plot of Figure 3.4 the dramatic difference in shape of the curves corresponding to the values of R along the minimum energy pathway can be seen. The range of values of R sampled along the minimum energy pathway is reduced for the M2 surface compared with the unmorphed surface. The difference in the curves of the R values corresponding to the minimum energy is quite large. This difference may in part be explained by insufficient data that determine the radial dependence of the well depth at the oxygen and carbon ends. Both the rotational constants and the centrifugal distortion constants are radially dependent. The wavefunction of the $K = 0$ bending state probes the 0 and 180° regions. So, the rotational constant and centrifugal distortion constant of this state should determine the radial dependence of the potential however the 95% confidence limit on ρ_1 is large. This high 95% confidence limit cannot be attributed to pairwise correlation matrix elements which suggests that the data was not as sensitive to the regions of the potential corresponding to the linear minima as initially thought.

3.5 Conclusions

All three potentials, the unmorphed, the M1 and the M2, have the same general shape. The potential is characterised by a single minimum and two saddle points corresponding to the linear configurations of the molecule. The well depth of the M1 and M2 potentials are very similar. The second virial coefficients however indicate that the well depth is not correct.

Compared to the unmorphed surface both the M1 and M2 potentials have improved agreement, excluding the second virial coefficients, with the experimental data. A significant difference between the M1 and M2 surfaces is in the agreement with experiment for the $(1, 0, 1, 1)$ state. The M1 surface is in error by 1.25 cm^{-1} for this state compared to the M2 surface which is in error by just

0.47 cm^{-1}. The asymmetry splitting for this state does not agree with experiment for either the M1 or the M2 surfaces. However the M2 surface obtained has closer agreement with experiment for the spectroscopic quantities used in the least squares fit than any other potential in the literature.

The amount of experimental data available for ArCO made it an excellent test case for the morphing procedure developed by Meuwly and Hutson [83]. Using this procedure, surfaces that have improved agreement with experiment have been obtained. However agreement with all the available experimental data was not possible even when the number of morphing parameters was doubled from three to six. This suggests that the quality of the unmorphed surface was too low to be able to achieve agreement with all experimental data. There are a number of possible reasons for the deficiencies in the unmorphed surface, perhaps the *ab initio* calculations required a higher level of correlation treatment or basis sets that included f-functions, or alternatively that more *ab initio* points should have been calculated in θ. The density of points required to obtain a high quality potential energy surface is discussed in the following chapter and appears to be the most likely cause of the deficiencies in the unmorphed surface.

CHAPTER

4

Obtaining potential energy surfaces: choosing a grid on which to do *ab initio* energy calculations.

4.1 Introduction

A significant constraint in adopting the supermolecular approach to obtaining potential energy surfaces that approach spectroscopic accuracy, is the number of single point electronic structure computations involved. The high level of correlation treatment and large basis sets required for each computation necessitate large amounts of memory and CPU time. It is shown here that by making a judicious choice of where in configuration space to perform *ab initio* computations, the number of these computations can be reduced, without sacrificing the quality of the potential, resulting in a large saving of overall CPU time.

At this time no comparative study of the optimum number and distribution of points has been published in the literature. Hence there appears to be no convention for choosing points for *ab initio* computations [56,67]. The main three things that guide the distribution of points are: the physics of the system; the method used to produce an analytical potential form and the properties that will be computed from the potential. Yet groups working on the same system continue to do electronic structure computations at different places in configuration space [73,74]. Consequently the number and distribution of points needs to be rationalized.

The aim of this work is to find a computationally affordable number of points from which a potential surface, useful for analysis of spectroscopic data, can be produced. $ArCO_2$ is chosen as the prototype system for this study. Hutson *et al.* [43] have calculated an analytical potential form for this system which will be used to 'simulate' the interaction energies, in place of electronic structure methods. The polar plot, Figure 4.1, of their surface reveals that the system is quite anisotropic which makes obtaining a potential energy surface from a discrete set of points difficult. A cut through the global minimum at a constant distance from the carbon atom, R, reveals a difference of almost 8000 cm^{-1} between the maximum and minimum energies. Using an analytical potential saves computational expense and allows for detailed analysis of discrepancies in the simulated potential.

The co-ordinate system and method of producing an analytical potential form are considered when trying to rationalize the distribution of points. The findings will be used for future potential computations.

This chapter is split into two sections dealing with the angular and radial co-ordinates respectively. The angular section looks first at the distribution of points, then the best interpolation scheme, and finally considers whether the co-ordinate system used is the most appropriate for this work. Having established the co-ordinate system, the radial section deals only with the distribution of points and the interpolation scheme. The quality of the surface resulting from a particular distribution is assessed by evaluating the deviation of the interpolated surface from the original at specific points in configuration space.

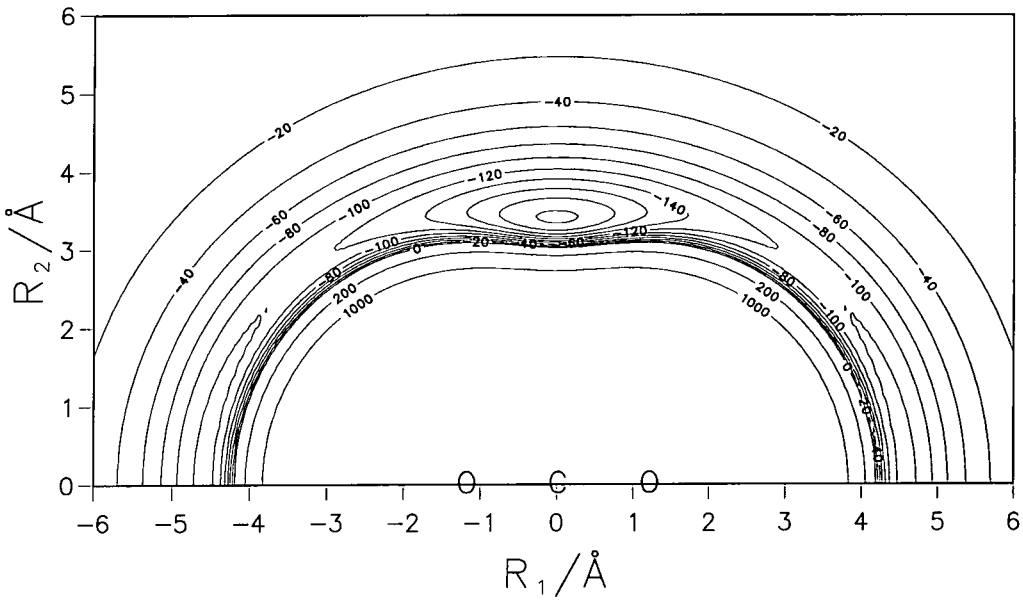

Figure 4.1: The $ArCO_2$ potential energy surface of Hutson *et al.* [43]. The origin is at the carbon atom. The oxygen atoms are at $(R_1, R_2) = (\pm 1.162\text{Å}, 0)$. Contours are labeled in cm^{-1}

4.2 Angular Co-ordinate

4.2.1 Initial Conditions

Jacobi co-ordinates, as shown in Figure 4.2, were used in the work of Hutson *et al.* on $ArCO_2$ and so are adopted here initially also. The length of the vector that points from the centre of mass of the CO_2 monomer (carbon) to the Ar atom is R and the angle formed by this vector and the z axis is θ.

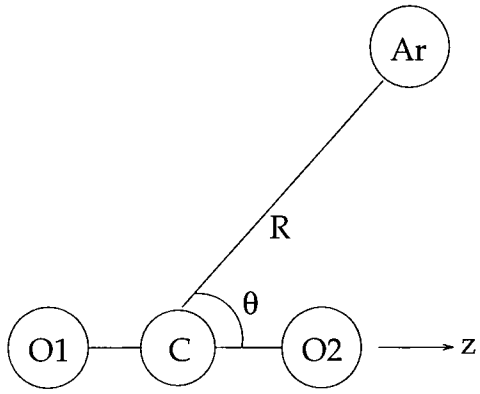

Figure 4.2: Jacobi coordinate system

The method used to obtain a continuous potential from the discrete interaction energy data can strongly influence the quality of the resulting potential. Interpolation methods reproduce all the data exactly and so are favoured over methods such as to fit a functional form to the energy data, which often requires many parameters to reproduce the data to within acceptable limits.

Initially, the reproducing kernel Hilbert space interpolation scheme of Ho and Rabitz [79] is used for the radial co-ordinate and Legendre polynomials are projected out in the angular co-ordinate. These methods worked well for the ArCO case in Chapter 3 and, it is hoped, will work equally well in this case.

Two distributions of points in the angular co-ordinate are considered, equally spaced and Gauss-Legendre quadrature points. The first is a popular choice in the literature and the second may be more appropriate for the angular projection than equally spaced points because they are good points at which to do integration. Hence fewer points may be required. Both these distributions demand similar computational effort and a choice cannot be made on these grounds alone.

When the points are placed at Gauss-Legendre quadrature points, the coefficients of the expansion do not need to be found by matrix inversion. Instead, at fixed values of R, both sides of Equation 3.1 are post multiplied by $P_\lambda(\cos\theta)$ and rearranged. So that the expansion coefficient is

$$C_\lambda = \frac{2\lambda+1}{2}\int_{-1}^{1} V(x)P_\lambda(x)\,dx \tag{4.1}$$

where $x = \cos\theta$. This integral is then solved using quadrature

$$\frac{2\lambda+1}{2}\int_{-1}^{1} V(x)P_\lambda(x)\,dx = \sum_{i=0}^{n} W_i V(x_i)P_\lambda(x_i) \tag{4.2}$$

where W_i are the weight factors.

4.2.2 Testing the quality of the surface

It is important that when assessing the quality of a surface, the deviations from the Hutson potential can be confidently attributed principly to the lack of points in the angular co-ordinate. To this end 30 radial points covering the key interaction region, 3 Å$\leq R \leq$ 6 Å are used for the RKHS interpolation. One cut at constant $R = 3.414$Å, is employed to assess the quality of the surface. This is the value of R that is closest to the global minimum when 30 points are used. The anisotropy in this region makes it difficult to project out an accurate potential. So if the potential is reproduced well here, one can be reasonably confident that it is reproduced well in regions where the anisotropy is smaller.

Each potential is evaluated at three points, $\theta = 90°, 70.0°, 64.1°$. These points are chosen as they span the full range of energy in the minimum region. They correspond to the energy at the minimum, close to -100 cm^{-1} and close to 0 cm^{-1} for this cut. So, the key points against which the potentials will be tested are:

$$\begin{aligned}
\theta &= 64.1°/115.9°, \quad R = 3.414\text{Å}, \quad \epsilon = -100.75\text{cm}^{-1};\\
\theta &= 70.0°/110.0°, \quad R = 3.414\text{Å}, \quad \epsilon = 0.23\text{cm}^{-1};\\
\theta &= 90.0°, \quad\quad\quad R = 3.414\text{Å}, \quad \epsilon = -204.16\text{cm}^{-1}.
\end{aligned} \tag{4.3}$$

This study is performed with a view to applying the findings to the computation of potentials that approach spectroscopic accuracy in the future. The

surfaces obtained from *ab initio* computations are not of spectroscopic accuracy. So to aim to reproduce the Hutson potential exactly is unnecessarily ambitious. The potential only needs to be a good starting point for the morphing procedure *i.e.*, free of unphysical oscillations. Consequently a deviation of 0.1 cm^{-1} will be accepted as an upper error bound. Additionally the potential is symmetric about 90°. This is a key feature that must be reproduced by the simulated potential.

Figure 4.3 shows the magnitude of the error in the projected potential, as the number of points in θ is varied, for both distributions. It is important to point out that with $\theta = 90.0°$ there is a point at the minimum and so the error in the projected potential with an odd number of points will be zero. When points are distributed equally, 17 are necessary to reproduce the key features. With Gauss-Legendre quadrature points the minimum number is 15, a difference of two. This is a small difference and significantly less than expected. If matrix inversion is used to determine the Legendre expansion coefficients, V_λ, then their value varies hugely as the number of points in θ is changed. When numerical quadrature is used the expansion coefficients are more stable, the coefficients vary little as the number of points is increased. Therefore Gauss-Legendre quadrature points will be adopted in the angular co-ordinate.

4.2.3 Interpolation Scheme

Ho and Rabitz have published a RKHS scheme for the angular co-ordinate as well as the radial. We chose however to use a Legendre projection (LP) instead as this worked well for ArCO. Here a comparison is made with the angular RKHS to verify that our choice is correct.

The methodology of the angular RKHS is much like that of the radial RKHS, as described in Chapter 3. The inner product, $V(x) = \langle q(x,x'), V(x') \rangle$, in this instance is defined over the interval $[0,1]$ rather than $[0,\infty)$ and taken over x'. The values of x at which the potential is known are then rescaled onto this interval. Here the reproducing function is:

$$q^n(x,x') = \sum_{i=0}^{n-1} x_l^i x_s^i + n x_l^n x_s^{n-1} {}_2F_1\Big(1, -n+1, n+1; \frac{x_s}{x_l}\Big). \tag{4.4}$$

The subscripts l and s refer to the larger and smaller of x and x'.

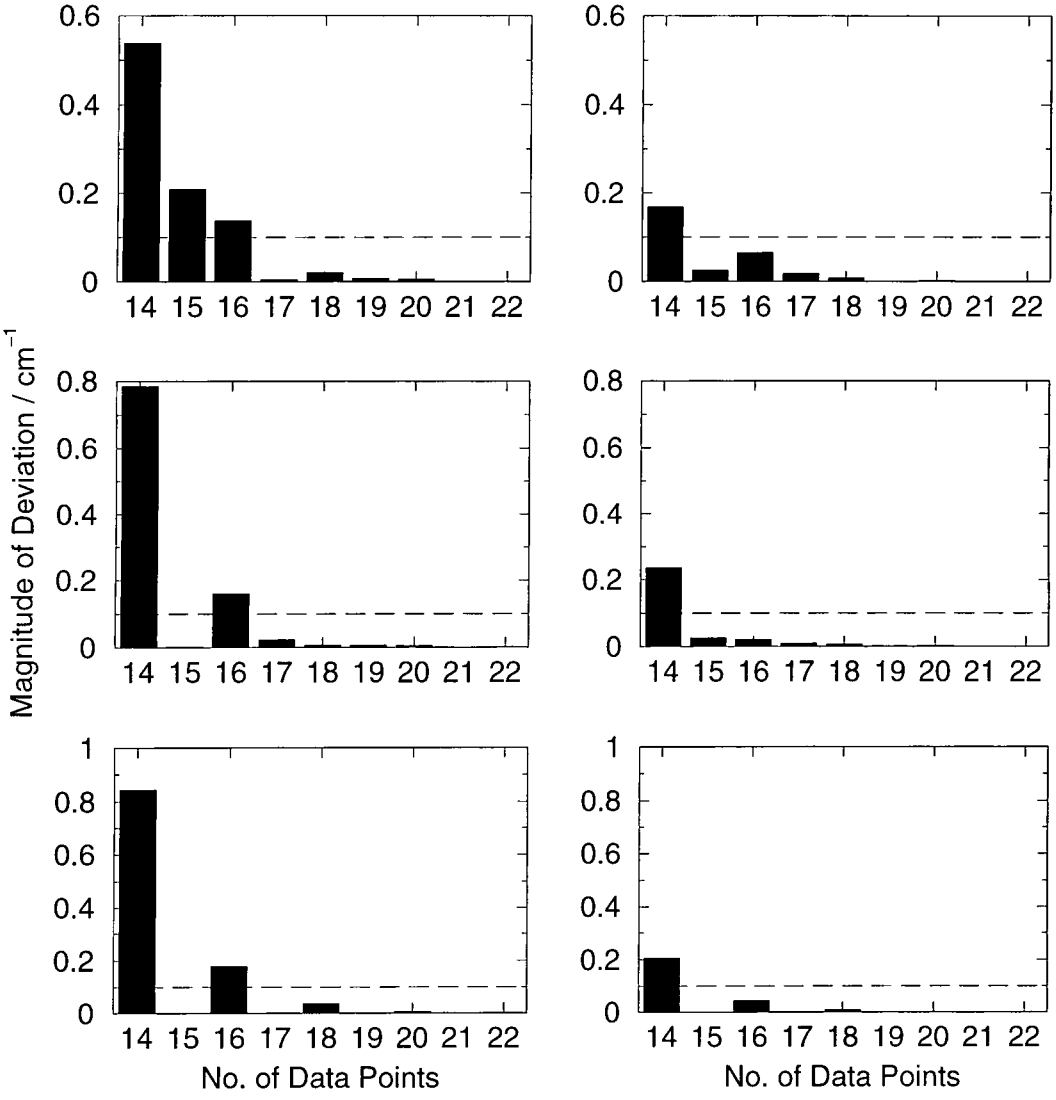

Figure 4.3: The magnitude of the deviation of the interpolated potential in Jacobi co-ordinates from the Hutson potential at (R, θ) = (3.414Å, 64.1°), (3.414Å, 70°), (3.414Å, 90°), top, middle and bottom graphs respectively. The left column uses equally spaced points and the right column uses Gauss-Legendre quadrature points.

As it is only the angular interpolation that is being tested, key features will be compared for $R = 3.414$ Å. It was found that 15 Gauss-Legendre quadrature points in θ reproduce the key potential features to an acceptable accuracy. With 15 points however there is a point at 90° which is coincident with one of the test features. Hence 16 points in θ, which has no points coincident with the test features, and 30 points in R are used to test the interpolation scheme. RKHS is used in both co-ordinates and compared with the RKHS, LP combination. Table 4.1 lists the key points for the three potentials. The symmetrically equivalent points are given to ensure that the symmetry of the system is retained. Two things are immediately obvious. Firstly, the RKHS potential does

R/ Å	θ/°	Hutson / cm^{-1}	RKHS / cm^{-1}	LP / cm^{-1}
3.414	90.0	-204.16	-204.32	-204.20
3.414	70.0	-100.75	-101.50	-100.80
3.414	110.0	-100.75	-101.44	-100.80
3.414	64.1	0.23	-0.41	0.26
3.414	115.9	0.23	0.33	0.26
4.552	0.0	-126.13	-126.37	-126.13
4.552	180.0	-126.13	-126.35	-126.13

Table 4.1: Comparison of the Hutson, RKHS interpolated and Legendre projection potentials at specific (R, θ) points. With 16 Gauss-Legendre quadrature points in θ and 30 equally spaced points in R between 3.0 Å and 6.0 Å.

not reproduce the key features as well as the LP potential; and secondly, the symmetry of the system is lost with the RKHS potential but retained with the LP potential.

The RKHS method is more susceptible to unphysical oscillations than the LP. This becomes very dramatic as the number of points is reduced. Figure 4.4 shows how with 7 points the RKHS oscillates unphysically. The LP potential also deviates from the Hutson potential but not in such an unphysical way. The loss of symmetry can be attributed to the scaling of $\cos\theta$ in the RKHS scheme from the interval $[-1, 1]$ onto the interval [0,1] which is inherent to the angular RKHS. The correct symmetry was not forced by only using points between

0° and 90°. Despite the reproducing function being symmetric with respect to the interchange of θ_s and θ_l *i.e.* $q(\theta_s, \theta_l) = q(\theta_l, \theta_s)$ the inner product is not symmetric.

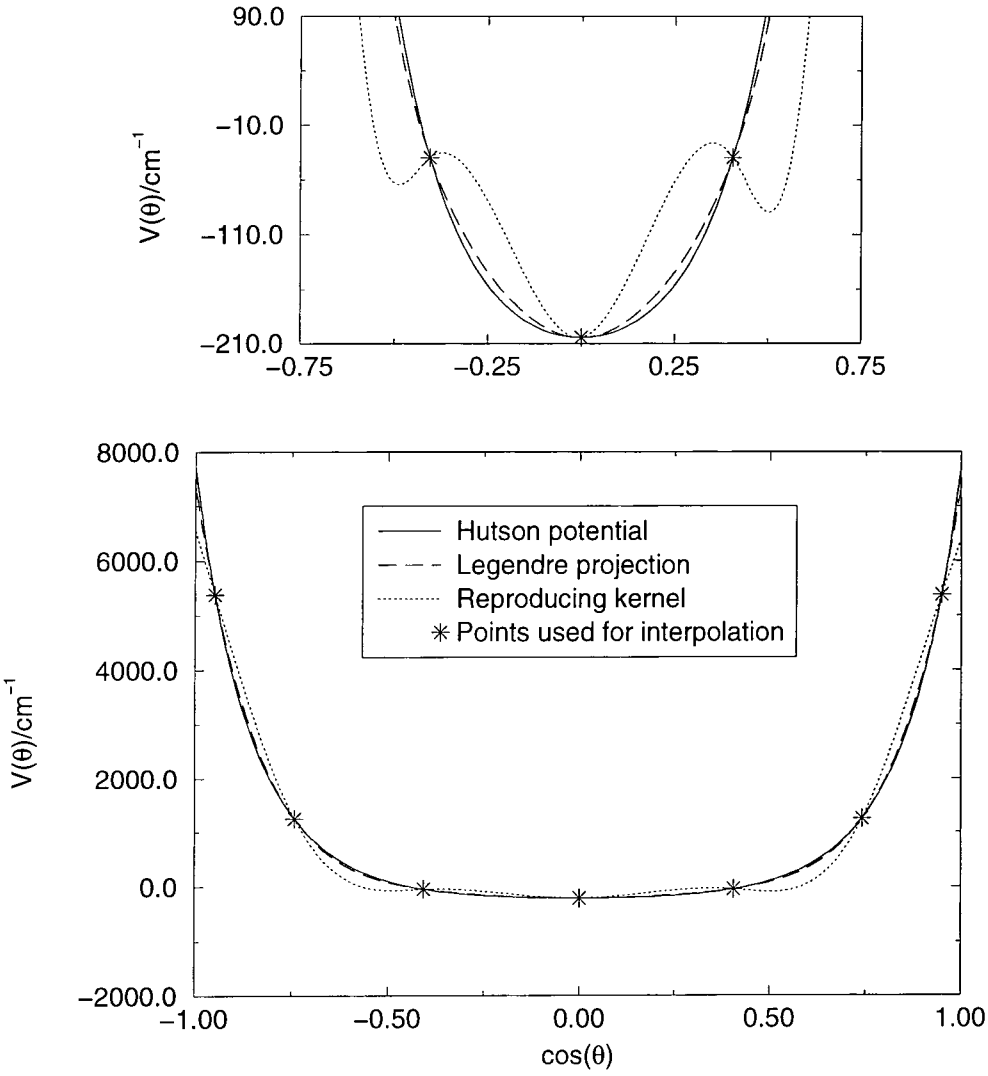

Figure 4.4: Comparison of cuts through the potentials obtained using different interpolation schemes at $R = 3.414$ Å.

The unphysical oscillations and the loss of symmetry that are present in the RKHS surfaces suggest the LP method should be used.

4.2.4 Co-ordinate System

The $ArCO_2$ potential when plotted in Jacobi co-ordinates is very anisotropic. However when plotted with a different co-ordinate system, in this case elliptic

co-ordinates, the anisotropy may be reduced and so too the number of points required. So, elliptic and Jacobi co-ordinates are compared in this work.

Elliptic co-ordinates are defined as:

$$\xi = \frac{R_1 + R_2}{r_1 + r_2}, \qquad \eta = \frac{R_1 - R_2}{r_1 + r_2}, \tag{4.5}$$

with ranges of

$$1 \leq \xi \leq \infty \qquad \text{and} \qquad -1 \leq \eta \leq 1 \tag{4.6}$$

for the general case of an atom, A, interacting with a linear molecule, BD, whose centre of mass is located at C, as illustrated in Figure 4.5. R_1 and R_2 are the distances from A to the ends of the molecule BD and r_1 and r_2 are the distances from B to C and C to D respectively.

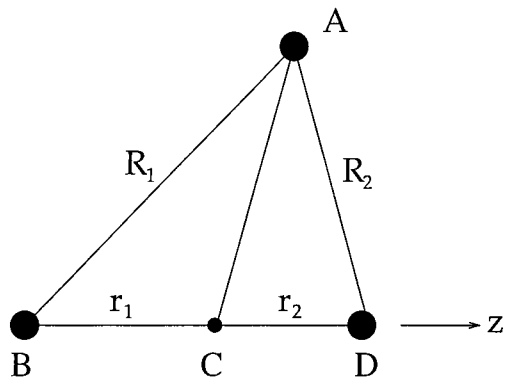

Figure 4.5: The elliptic co-ordinate system.

The ξ co-ordinate can be thought of as radial-like, and gives an indication of the distance of atom A from the principal axis of the BD molecule. If $\xi = 1$ then A is coincident with the principal axis; obviously not physically likely. This can be seen graphically in Figure 4.6, which plots ξ around the BD monomer. The η co-ordinate can be thought of as $\cos\theta$-like and gives an indication of the position of A along the BD monomer axis. If $\eta = 1$ then atom A is at the D end, if $\eta = -1$ it is at the B end and if $\eta = 0$ it is at the centre of mass. This is plotted in Figure 4.7.

Equations 4.7 and 4.8 are used to transform from elliptic co-ordinates back to Jacobi.

$$R = \left(R_2^2 + r_2^2 + \frac{r_2}{r}(R_1^2 - R_2^2 - r^2)\right)^{\frac{1}{2}}, \qquad r = r_1 + r_2 \tag{4.7}$$

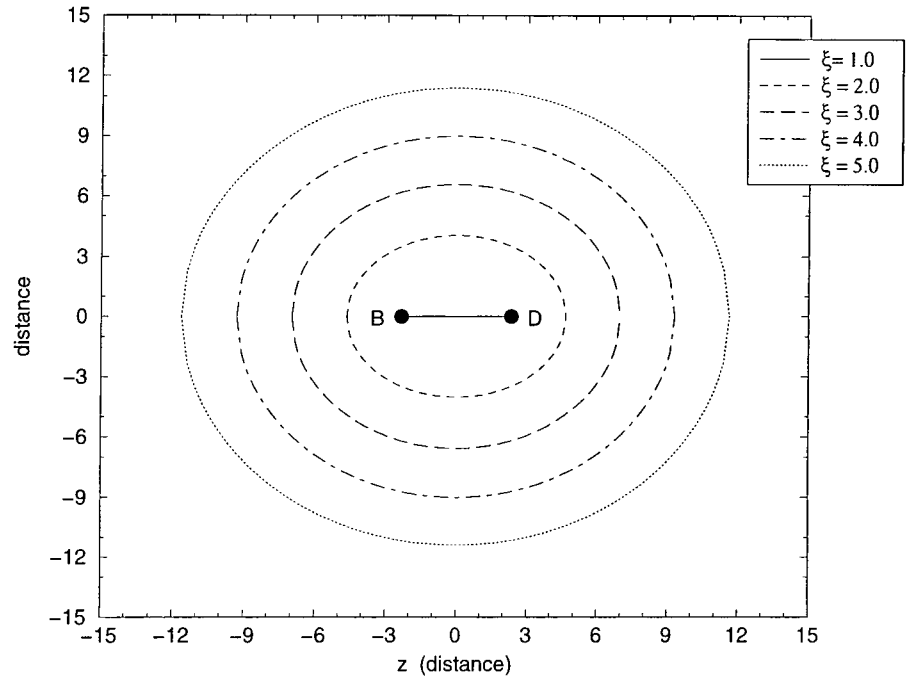

Figure 4.6: η is plotted at constant values of ξ.

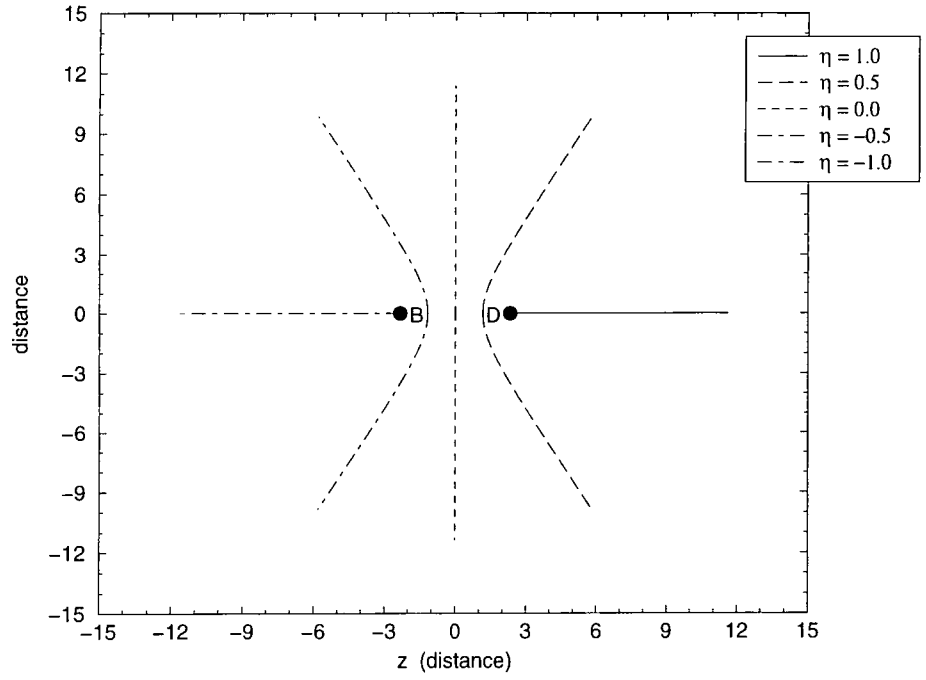

Figure 4.7: ξ is plotted at constant values of η.

$$\cos\theta = \frac{R^2 + r_2^2 - R_2^2}{2Rr_2} \tag{4.8}$$

In the case of $ArCO_2$, CO_2 is the ellipse. Above, the baseline, r, is equal to the BD bond length. This may not however be the most appropriate choice. The reason for using elliptic co-ordinates is to reduce the potential anisotropy, particularly in the repulsive wall region. Therefore the choice of baseline should be made so that, as far as possible,

$$V(R, 0°) \approx V(R, 90°) \approx V(R, 180°) = 0.0 \tag{4.9}$$

in the region of the repulsive wall. This would preclude the need to include large positive values of the potential coefficients in the interpolation.

With a baseline of $r_1 = r_{O1}$ and $r_2 = r_{O2}$, where r_{O1}, r_{O2} are the oxygen carbon bond lengths, Equation 4.9 is not satisfied. A plot of the potential with this choice of baseline, Figure 4.8 shows that although the anisotropy is reduced, compared to Figure 4.9, it is not sufficient to exclude higher values of the potential coefficients in the interpolation.

An alternative choice of baseline is: $r_1 = r_{O1} + r_{vdw}$, $r_2 = r_{O2} + r_{vdw}$ where $r_{vdw} = 1.4$ Å which is the Van der Waals radius of the oxygen atom. Figure 4.10 shows the potential plotted as a function of ξ and η. Comparing this with Figure 4.9 it is clear that the anisotropy has been reduced so that the range of the potential is smaller. This decrease in anisotropy may require a lower order Legendre polynomial expansion with a corresponding reduction in the number of quadrature points.

The cut at constant $\xi = 1.666$ will be used to assess the quality of the surface with a given number of points in η. Again this is the cut in ξ that is closest to the value of ξ at the global minimum. Points at the minimum, close to 0 cm^{-1} and 100 cm^{-1} will be used. It is found that as few as eleven points in η with 30 points in ξ over the range, [1.5, 2.3], are required to reproduce the potential features correctly in elliptic co-ordinates. This can be seen in Figure 4.11. The saving is large enough to justify the use of elliptic co-ordinates. The results of these investigations show that the least number of single points in the angular co-ordinate need to be used when a Gauss-Legendre expansion of the potential is used in elliptic co-ordinates.

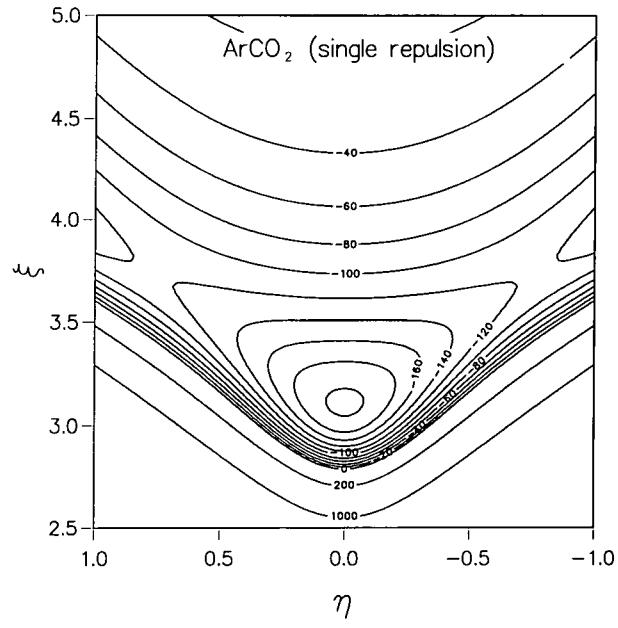

Figure 4.8: The $ArCO_2$ potential energy surface of Hutson *et al.* [43] plotted in elliptic co-ordinates with $r_1 = r_{O1}$ and $r_2 = r_{O2}$. Contours are labeled in cm^{-1}

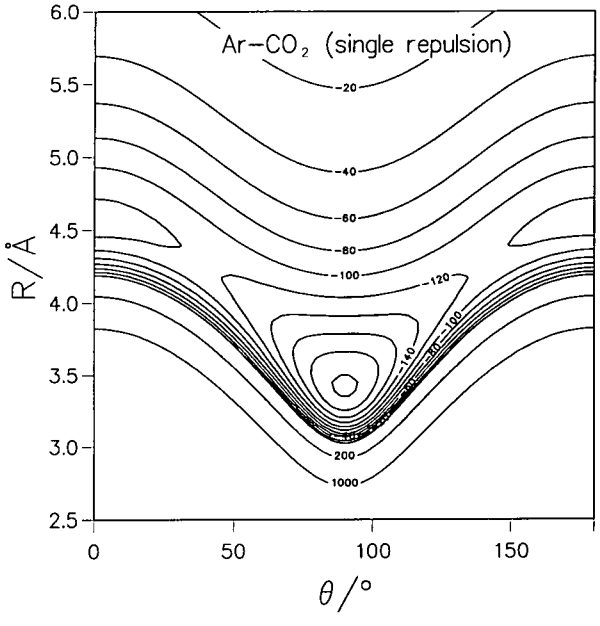

Figure 4.9: The $ArCO_2$ potential energy surface of Hutson *et al.* [43] plotted in Jacobian co-ordinates. Contours are labeled in cm^{-1}

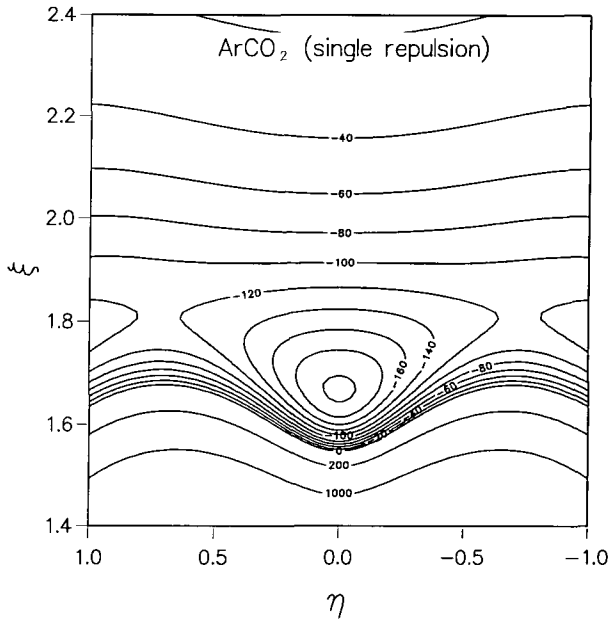

Figure 4.10: The $ArCO_2$ potential energy surface of Hutson *et al.* [43] plotted in elliptic co-ordinates with $r_1 = r_{O1} + r_{vdw}$ and $r_2 = r_{O2} + r_{vdw}$.

4.3 Radial Co-ordinate

4.3.1 Radial point distribution

Elliptic co-ordinates lead to a significant saving in the number of points required in the angular degree of freedom. Therefore elliptic co-ordinates are used here with 11 Gauss-Legendre quadrature points in η. Various arrangements of points in ξ are tested to determine the optimum choice.

The η co-ordinate is defined over a finite range such that the region of interest for systems involving a heteronuclear linear molecule and a rare gas atom is always $-1 \leq \eta \leq 1$. The ξ co-ordinate however is defined over an infinite range ($1 \leq \xi \leq \infty$) so the key interaction region (the well region) will change for different systems. This makes choosing an arrangement of points difficult if the region of interest is not known. Consequently, the aim of this work is to find a method of choosing a distribution that is easily transferable from system to system if the region of interest is known.

One advantage of using the Hutson potential for the $ArCO_2$ system is that the range of interest of ξ is known in advance. The range is chosen such that

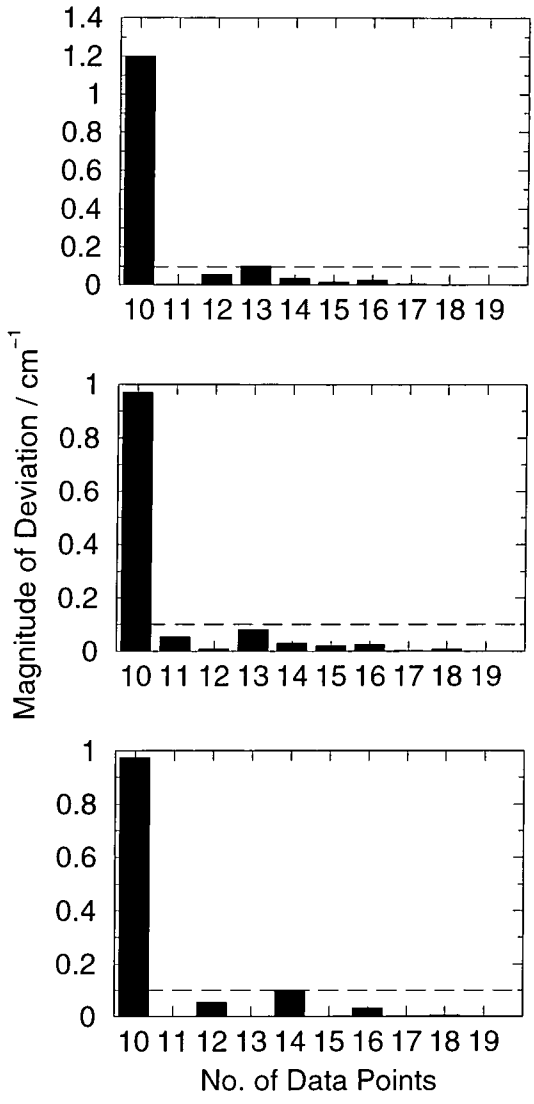

Figure 4.11: The magnitude of the deviation of the interpolated potential in elliptic co-ordinates from the Hutson potential at (ξ, η) = (1.666, 0.549), (1.666, 0.343), (1.666, 0.000), top, middle and bottom graphs respectively. The interpolation is done between points at Gauss-Legendre quadrature points in η.

the regions high up the repulsive wall and at long range where the potential is less than about 10% of the well depth are excluded as these regions were not probed by spectroscopy. Therefore the range of ξ for $ArCO_2$ is taken as [1.5, 2.3].

The quality of the interpolated surface is tested at:

$$\begin{aligned}
\xi = 1.668, \quad \eta = 0.000, \quad \epsilon &= -204.16\text{cm}^{-1}; \\
\xi = 1.914, \quad \eta = 0.000, \quad \epsilon &= -100.05\text{cm}^{-1}; \\
\xi = 2.150, \quad \eta = 0.000, \quad \epsilon &= -40.92\text{cm}^{-1}; \\
\xi = 1.785, \quad \eta = -1.000, \quad \epsilon &= -126.30\text{cm}^{-1}.
\end{aligned} \tag{4.10}$$

This corresponds to a single cut through the global minimum at $\eta = 0.0$, with an additional point at $\eta = -1.0$. The extra point tests both co-ordinates as neither have points at the linear minima.

Firstly an evenly spaced distribution of points is tested. In the previous section, 30 equally spaced points in ξ were used. The number can be reduced to 19 and still reproduce these test features to within 0.1 cm^{-}1:

$$\begin{aligned}
\xi = 1.667, \quad \eta = 0.000, \quad \epsilon &= -204.25\text{cm}^{-1}; \\
\xi = 1.914, \quad \eta = 0.000, \quad \epsilon &= -100.05\text{cm}^{-1}; \\
\xi = 2.150, \quad \eta = 0.000, \quad \epsilon &= -40.92\text{cm}^{-1}; \\
\xi = 1.785, \quad \eta = -1.000, \quad \epsilon &= -126.40\text{cm}^{-1}.
\end{aligned} \tag{4.11}$$

Reduce the number to 18 however and the global minimum is in error by 0.18 cm^{-1} which is unacceptable. Nineteen points in ξ is too many as this would require 209 *ab initio* computations. If each single point computation needs 6 CPU hours plus two extra computations to correct for basis set super position error, computation of the surface would demand almost 15 weeks CPU time.

The RKHS interpolation scheme involves integration in the ξ co-ordinate. So using quadrature points opposed to equally spaced points may result in fewer points being required for the potential surface. There are a number of different quadrature schemes that can be adapted for the radial integral and have been tried but only Gauss-Laguerre and Gauss-Legendre quadrature are discussed below.

Gauss-Legendre quadrature has inappropriate limits but can be mapped onto the region of interest using the mapping,

$$\xi' \rightarrow \xi'_{\min} + \frac{(\xi'_{\max} - \xi'_{\min})}{(\xi_{\max} - \xi_{\min})}(\xi - \xi_{\min}) \tag{4.12}$$

where ξ' corresponds to the quadrature points on the range $[-1, 1]$, $\xi'_{\max} = 1.0$ and $\xi'_{\min} = -1.0$; ξ corresponds to the quadrature point after the mapping with $\xi_{\max} = 2.3$ and $\xi_{\min} = 1.5$. This arrangement does not perform any better than equally spaced points. In fact more points are needed to reproduce the features correctly. With 21 points the test features are:

$$\begin{aligned}
&\xi = 1.667, \quad \eta = 0.000, \quad \epsilon = -204.18\text{cm}^{-1};\\
&\xi = 1.914, \quad \eta = 0.000, \quad \epsilon = -100.05\text{cm}^{-1};\\
&\xi = 2.150, \quad \eta = 0.000, \quad \epsilon = -40.92\text{cm}^{-1};\\
&\xi = 1.785, \quad \eta = -1.000, \quad \epsilon = -126.41\text{cm}^{-1}.
\end{aligned} \tag{4.13}$$

If the number of points is decreased to 20 then the linear minimum is in error by 0.11cm^{-1}. This arrangement is expected to be a little inappropriate as the points are closely spaced at the two ends but more widely spaced in the central region. For this reason the linear minimum is also the one that fails first because it is close to the centre of the integration range where there is not a point.

Fewer Gauss-Laguerre quadrature points may be required than equally spaced ones because the arrangement of points appears to be advantageous. The points are closely spaced at short range, and more disperse at long range. So more points will be used in the difficult to interpolate repulsive wall region where the gradient is steepest.

In practice there are insufficient points in the range of interest to make Gauss-Laguerre beneficial. Six points out of a ten point quadrature, (0.138, 0.729, 1.808, 3.401, 5.552, 8.330, 11.844, 16.279, 21.997, 29.921) are in the interval, $5 < \xi < 30$, which is far outside the region of interest. These points can however be mapped onto the region of interest with the mapping given in Equation 4.12.

Here ξ' corresponds to the quadrature points on the range $[0, \infty)$, with $\xi'_{\max} = \infty$ and $\xi'_{\min} = 0.0$). Using $\xi'_{\max} = \infty$ however is not practical and so the largest value of ξ' is used instead.

With this distribution and only 11 points in ξ the test features are:

$$\begin{aligned}
\xi = 1.667, \quad \eta = 0.000, \quad \epsilon &= -204.10\text{cm}^{-1}; \\
\xi = 1.914, \quad \eta = 0.000, \quad \epsilon &= -100.07\text{cm}^{-1}; \\
\xi = 2.150, \quad \eta = 0.000, \quad \epsilon &= -40.92\text{cm}^{-1}; \\
\xi = 1.785, \quad \eta = -1.000, \quad \epsilon &= -126.38\text{cm}^{-1}.
\end{aligned} \tag{4.14}$$

With 10 points in ξ the linear minimum becomes, -126.45 cm^{-1} and the global minimum, -203.99 cm^{-1} which is greater than acceptable error. Therefore 121 points are needed to obtain a potential that approaches spectroscopic accuracy. This is acceptable but it seems a little wasteful to compute so many points on the repulsive wall as this is a region of little importance when spectroscopic properties are of interest.

The main difficulty with obtaining these potentials is that the magnitude of the difference between any two consecutive data points is quite large. For example, consider a distribution with 11 points at Gauss-Legendre quadrature points in η and 18 equally spaced points in ξ in the interval [1.5, 2.3]. The magnitude of the difference in energy between $(\xi, \eta) = (1.5, -0.73)$ and $(1.55, -0.73)$ is 1118 cm^{-1}. By reducing this difference the interpolation problem becomes simpler and fewer points should be required. This can be achieved by dividing each potential point by a smooth positive function.

The two functions considered that satisfy this criteria are,

$$f(\xi) = Ae^{-\beta\xi} \quad \text{and} \tag{4.15}$$

$$f(\xi) = Ae^{-\beta\xi} + 1. \tag{4.16}$$

They are chosen as they are simple potential-like functions, a little like that used in the systematic model of Chapter 2. Assuming the repulsive wall is approximately exponential, these functions will have the correct behaviour. The constants A, β are found by setting $\frac{v(\xi)}{f(\xi)} = 1$ for the first two points on the repulsive wall in ξ and solving the two simultaneous equations.

Function 4.15 behaves like an exponential function. As ξ increases, $f(\xi) \to 0$, so that, $\frac{v(\xi)}{f(\xi)} \to \infty$. This will of course lead to large differences in consecutive energy points at large values of ξ. The interesting range of ξ is small here and so the limit should not be reached. In other systems, however, one cannot be

so confident as a larger range of ξ may be appropriate. It is found that with this function more than 20 equally spaced points are required to reproduce the test features. With this range the maximum value of $\frac{v(\xi)}{f(\xi)}$ is 1.0 cm^{-1} but the minimum is -11430 cm^{-1}.

With the second function, Equation 4.16, as ξ increases, $f(\xi) \rightarrow 1$ and $\frac{v(\xi)}{f(\xi)} \rightarrow v(\xi)$. With this function, 16 equally spaced points produce the key features:

$$\begin{aligned}
&\xi = 1.667, \quad \eta = 0.000, \quad \epsilon = -204.15 cm^{-1};\\
&\xi = 1.914, \quad \eta = 0.000, \quad \epsilon = -100.05 cm^{-1};\\
&\xi = 2.150, \quad \eta = 0.000, \quad \epsilon = -40.92 cm^{-1};\\
&\xi = 1.785, \quad \eta = -1.000, \quad \epsilon = -126.37 cm^{-1}.
\end{aligned} \tag{4.17}$$

Reduce the number to 15 and the linear minima are in error by 0.11 cm^{-1} and with 14 the global minimum is in error by 0.25 cm^{-1}. The extra computational effort required for this distribution is not justified given that this is only a saving of two points in the ξ co-ordinate over equally spaced points.

4.3.2 Radial interpolation scheme

Splines [130] are often used in the literature as a simple way of obtaining an analytical form for a potential surface. The RKHS method was favoured here as it forces the correct long range behaviour and is stable for both regular and scattered grids. Additionally the order of smoothness, the number of derivatives that are equal to zero, of the RKHS can be decided by the user. This is advantageous because, if the potential is to be smooth, continuous derivatives are compulsory. Cubic splines have smooth first derivatives and continuous second derivatives.

RKHS and cubic splines are compared here to verify that RKHS is better for this work. Again, if 11 Gauss-Legendre points in η are used with 19 equally spaced points in ξ, the RKHS method reproduces the potential features to within 0.01 cm^{-1}. With cubic splines the features are:

$$\begin{aligned}
&\xi = 1.667, \quad \eta = 0.000, \quad \epsilon = -204.36 cm^{-1};\\
&\xi = 1.914, \quad \eta = 0.000, \quad \epsilon = -100.05 cm^{-1};\\
&\xi = 2.150, \quad \eta = 0.000, \quad \epsilon = -40.92 cm^{-1};
\end{aligned}$$

$$\xi = 1.785, \quad \eta = -1.000, \quad \epsilon = -126.40\text{cm}^{-1}. \tag{4.18}$$

The global minimum is in error by 0.2 cm^{-1}, which is twice the acceptable error bound, suggesting that the cubic spline does not perform as well as the RKHS method.

Above, fewest points were required when Gauss-Laguerre quadrature points were mapped onto the region of interest. Recall that 11 reproduced the features to within the error limits. If cubic splines are used, 11 points in ξ produce:

$$\begin{aligned}
&\xi = 1.667, \quad \eta = 0.000, \quad \epsilon = -204.21\text{cm}^{-1};\\
&\xi = 1.914, \quad \eta = 0.000, \quad \epsilon = -100.10\text{cm}^{-1};\\
&\xi = 2.150, \quad \eta = 0.000, \quad \epsilon = -40.13\text{cm}^{-1};\\
&\xi = 1.785, \quad \eta = -1.000, \quad \epsilon = -126.50\text{cm}^{-1}.
\end{aligned} \tag{4.19}$$

Here the global minimum is within the error bounds, however the points at $\xi = 2.15$ and the linear minima are not, having errors of 0.79 cm^{-1} and 0.2 cm^{-1} respectively. In both instances the RKHS reproduces the test potential features more accurately than cubic splines, thus justifying the use of the RKHS method in the present work.

4.4 Conclusions

The minimum number of points with which it has been possible to compute the test potential features to within the desired error bounds in the present study has been 121. It has not been possible here to use a distribution in the radial-like co-ordinate that does not depend upon prior knowledge of the key interaction region of the potential. Investigation into the co-ordinate system revealed that elliptic co-ordinates lead to a reduction in the anisotropy and consequently the number of angular points required. Additionally, the number of points required has been shown to depend on the interpolation method adopted.

CHAPTER

5

The Intermolecular Potential of He–OCS.

5.1 Introduction

Over the past few years significant advances have been made in the study of atoms and molecules in liquid helium [131]. By performing these studies the hope is to gain a greater understanding of the properties of helium as well as make advances in the power of molecular spectroscopy. Small molecules such as SF_6 [132] and OCS [133] as well as large molecules like tryptophan [134] have been observed in liquid helium. Even reactions have been observed in liquid helium.

When measured in liquid helium the rotational constants of the OCS, SF_6 and the HCN dimer are all reduced by close to a factor of 3 compared with the gas phase [135]. This effect is not observed with lighter molecules such as the HCN monomer. The reason for the effect may be due to drag effects of the

helium although this is not clear [135].

The recent experiment by Toennies and co-workers [133], that measured the rotational spectrum of the OCS molecule in liquid helium clusters, has excited interest in the He-OCS system. The only spectroscopic experiments published for this dimer, are those by Higgins and Klemperer [56]. Other experimental work on this system includes the measurement of diffusion factors and thermal diffusion factors [136]. Rotational inelastic cross sections have been measured [137] as well as total differential cross sections (although these were not resolved into elastic and inelastic contributions) [138]. Therefore the most detailed information about the potential surface comes from high resolution microwave spectroscopy.

Prior to the publication of the OCS in liquid helium experiment, Keil *et al.* [36] used the Hartree Fock method to calculate the repulsive interaction between OCS and He at different places in configuration space. Sadlej and Edwards [139] performed MP4 computations to optimise the minimum energy configurations and found three potential minima geometries, for the He-OCS system.

Higgins and Klemperer obtained a potential energy surface, henceforth referred to as the HK potential, to help in the assignment of the measured rotational transitions [56]. They adopted the supermolecular approach, with full counterpoise correction [62], to calculate interaction energies. Using MP4, with the core electrons frozen and a basis set consisting of both atom-centred and bond functions, they computed an irregular grid of 98 points with 2.5 Å $\leq R \leq$ 10.0 Å. They fitted a functional form to the data at each angular cut in order to generate a regular grid of 175 points, between 2.5 Å $\leq R \leq$ 20.0 Å. By putting a bicubic spline through the points on this grid they obtained a potential surface with three minima. The smallest discrepancy between the rotational transitions computed using this surface and experiment was 35 MHz and the largest was 1317 MHz, both of which are well outside experimental uncertainty. Closer agreement with experiment can be obtained. They also compared the rotational constants and centrifugal distortion constants. Improved agreement with the centrifugal distortion constants was achieved if the MP4 potential is made 10% deeper.

The effect of the grid chosen for the *ab initio* computations on the final potential was illustrated in the previous chapter, suggesting that the Higgins and Klemperer grid was not optimal. Their work showed that HeOCS has a small potential minimum and a large zero point energy. Therefore the experimental data sampled a large part of the anisotropic potential making HeOCS a good case for the morphing proceedure. In this chapter a grid of points, chosen on the basis of the previous chapter's work, is used in combination with RKHS to produce a potential that can be morphed to achieve agreement with experiment for ^{4}He with $^{16}O^{12}C^{32}S$.

5.2 Experimental Data

Higgins and Klemperer have measured 10 rotational transitions for the ground state of the He-OCS system which are shown schematically in Figure 5.1. The inertial axes for the system are given in Figure 5.2.

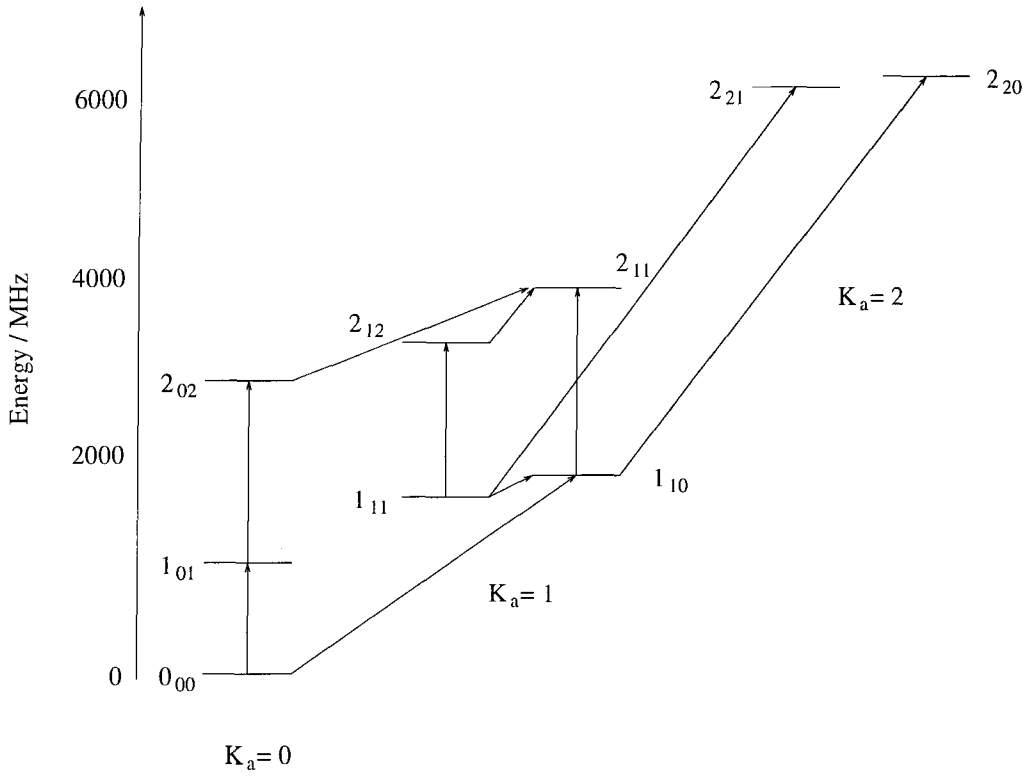

Figure 5.1: The rotational transitions measured by Higgins and Klemperer [56]. Energy levels are labeled $J_{K_a K_c}$.

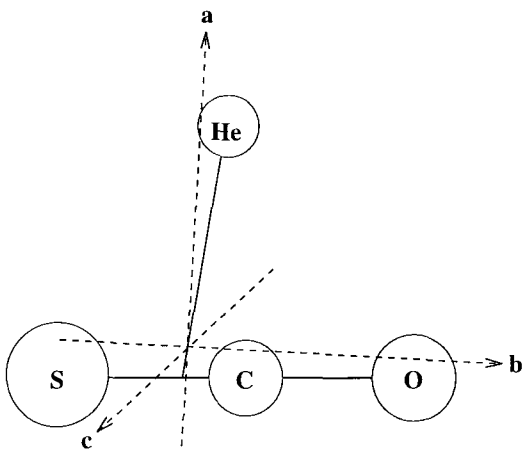

Figure 5.2: The HeOCS inertial axes.

By taking combination differences of these energy level transitions it is possible to obtain quantities that are approximately proportional to the rotational and centrifugal distortion constants for the system. The advantage of using these constants over the raw transition frequencies is that the constants tell us about specific features of the potential, so physical insight can be applied when fitting the morphing parameters. Secondly, using combination differences avoids duplication of information in the least squares fit, as some of the levels sample the same regions of the potential. Fitting to $x + y$ and $x - y$ is very different to fitting to x and y.

HeOCS is a prolate near-symmetric rotor molecule as the rotational constants are related $A > B \approx C$. If the molecule was T-shaped, the a-inertial axis would lie exactly along the intermolecular axis. The difference between the OCS rotational constant and the A rotational constant therefore is a measure of the deviation of θ_{min} from 90°. The quantity $2A \approx 1_{10} + 1_{11} - 1_{01} = 26321.613$ MHz is used in the least squares fit. This compares to the OCS rotational constant, b_{OCS}, of 6081.49 MHz. The large difference between the two rotational constants suggests that the molecule will be far from T-shaped. The B rotational constant gives information on the position of R_{min}. The quantity $2B \approx 1_{10} - 1_{11} + 1_{01} = 10962.705$ MHz is used in the least squares fit. The C rotational constant gives information on the radial and angular amplitude of motion. The quantity $2C \approx 1_{11} - 1_{10} + 1_{01} = 7360.919$ MHz is used in the least squares fit.

The combinations of levels required to isolate the effects of centrifugal distortion are more complicated. The combination $(2_0 \leftarrow 1_0) - 2 \times (1_0 \leftarrow 0_0)$ would give a quantity approximating D_J for a symmetric rotor. Due to asymmetry splittings the expression becomes

$$(2_{02} + (2_{20} - 2_{21}) - 1_{01}) - 2 \times (1_{01} - 0_{00}) \approx -24D_J$$

for HeOCS. This gives information on the shape of the potential in the region of the minimum and has magnitude 22.576 MHz.

In a symmetric rotor the combination $(2_1 \leftarrow 2_0) - (1_1 \leftarrow 1_0)$ approximates the D_{JK} constant. The expression becomes

$$(2_{11} - \frac{1}{2}(2_{12} - 2_{11}) - 2_{02} + (2_{20} - 2_{21})) - \frac{1}{2}(1_{11} + 1_{10} - 1_{01}) \approx -4D_{JK}$$

for HeOCS with magnitude 5.594 MHz. This gives an indication, as the molecule is bent by centrifugal distortion, of the force constant.

Finally the expression $(2_2 \leftarrow 2_1) - 3 \times (2_1 \leftarrow 2_0)$ is approximately proportional to D_K in the symmetric rotor. The equivalent expression for an asymmetric rotor is

$$(2_{20} - (2_{20} - 2_{21}) - \frac{1}{2}(2_{11} + 2_{12})) - 3 \times (\frac{1}{2}(2_{11} + 2_{12}) - 2_{02} + (2_{20} - 2_{21})) \approx -12D_K$$

with magnitude 516.850 MHz. This gives an indication of how, as the molecule is stretched by centrifugal distortion, the bending amplitude of motion alters.

For the purposes of the least squares fit, uncertainties of 10 MHZ, 5 MHz and 3.5 MHz were applied to the A, B and C rotational constants. These values were guided by experimental uncertainty but essentially correspond to the desired agreement between experiment and theory. Each of the centrifugal distortion constants had an uncertainty of 1 MHz.

5.3 Theoretical Methods

5.3.1 Co-ordinate System

In light of the work in Chapter 4, where using elliptic co-ordinates reduced the number of single point energy computations necessary to obtain a potential

energy surface, elliptic co-ordinates are adopted here. The baseline employed, $r_1 + r_2$, is in this case between the oxygen and sulphur nuclei.† To reproduce the key features for the $ArCO_2$ system, with elliptic co-ordinates centred on the nuclei, 13 Gauss-Legendre quadrature points in η and 19 equally-spaced points in ξ were required. Hence the same number and distribution of points are used here. The region of interest, $2.3 \leq \xi \leq 4.8$, is established from the HK potential.

Elliptic co-ordinates are described in Chapter 4; here R_1 corresponds to the helium-sulphur distance and R_2 corresponds to the helium-oxygen distance. Therefore when $\eta = -1.0$, helium is next to sulphur and when $\eta = 1.0$, helium is next to oxygen.

The work of HK is in Jacobi co-ordinates so, comparisons are made with their work in Jacobi co-ordinates. The Jacobi system is set up such that at 0° helium is at the oxygen end and at 180° helium is at the sulphur end.

5.3.2 Obtaining the Unmorphed Potential

As the number of points required (246) to be computed is so large, and the CPU time available is limited, the level of *ab initio* theory and size of basis set is restricted. The relative interaction energies and CPU time involved in a single point calculation with Dunning's aug-cc-pVDZ, aug-cc-pVTZ and aug-cc-pVQZ basis sets [140–143] and the CCSD(T) method, was investigated close to the minimum at the oxygen end. The resulting energies are tabulated for the aug-cc-pVTZ and aug-cc-pVQZ basis sets in Table 5.1. The aug-cc-pVTZ basis was found to provide the best compromise between time and basis set size. Further, both full correlation and frozen core CCSD(T) methods were investigated. The Dunning basis sets were designed for frozen core computations although a more complete treatment of electron correlation is the full correlation method. The difference in energy at the single point, calculated with both methods, was 0.07 cm^{-1} following correction for BSSE, while the saving in CPU time was almost a factor of four. Hence, frozen core CCSD(T) was

†At the time the present work was performed, the development of placing the ends of the ellipse away from the nuclei had not been made.

Basis set	Method	Energy	CPU Time
aug-cc-pVTZ	CCSD(T)	-18.15 cm^{-1}	42hrs36mins
aug-cc-pVTZ	CCSD(T,FC)	-18.08 cm^{-1}	10hrs45mins
aug-cc-pVQZ	CCSD(T)	-21.21 cm^{-1}	2weeks
aug-cc-pVQZ	CCSD(T,FC)	-21.16 cm^{-1}	6days

Table 5.1: Comparison of aug-cc-pVTZ and aug-cc-pVQZ basis sets for full BSSE corrected energies. Calculations were carried out on a silicon graphics origin 2000.

employed.

Boys and Bernardi's [62] full counterpoise correction for BSSE was employed. This involves evaluating the equation,

$$\epsilon(\xi,\eta) = \epsilon_{\mathrm{HeOCS}}(\xi,\eta) - \epsilon_{\mathrm{He}}(\xi,\eta) - \epsilon_{\mathrm{OCS}}(\xi,\eta), \tag{5.1}$$

where $\epsilon_{\mathrm{He}}(\xi,\eta)$ is the energy of the helium atom evaluated using the supermolecular basis and $\epsilon_{\mathrm{OCS}}(\xi,\eta)$ is the energy of the OCS monomer calculated using the supermolecular basis. This is necessary because the basis set centred on He is incomplete and so uses the basis sets centred on OCS as well, and vice versa, causing an artificial lowering of the interaction energy. All the *ab initio* computations were carried out using GAUSSIAN94 [111]. The OC and CS bond lengths were held fixed at 1.156 Å and 1.561 Å respectively.

At each cut in ξ the potential is projected out in Legendre polynomials. At each cut in η, RKHS is used to interpolate between the coefficients from the projection. This is described fully in Chapters 3 and 4. The resulting potential is plotted in Figure 5.3.

The potential has a global minimum of -43.27 cm^{-1} at $\eta = 0.241, \xi = 2.618$, and two linear minima at each end of the OCS molecule. The minimum at the oxygen end is -25.21 cm^{-1} with $\xi = 3.314$. This is shallower than the minimum at the sulphur end which is -27.90cm^{-1} with $\xi = 3.565$. The two linear minima are separated from the global minimum by transition states found at $(\xi,\eta) = (3.421, -0.524)$ and $(\xi,\eta) = (3.193, 0.839)$ with magnitudes, -15.81 cm^{-1} and -23.84 cm^{-1} respectively. Hence the potential in the region of the oxygen molecule is quite flat. This agrees qualitatively with the HK potential.

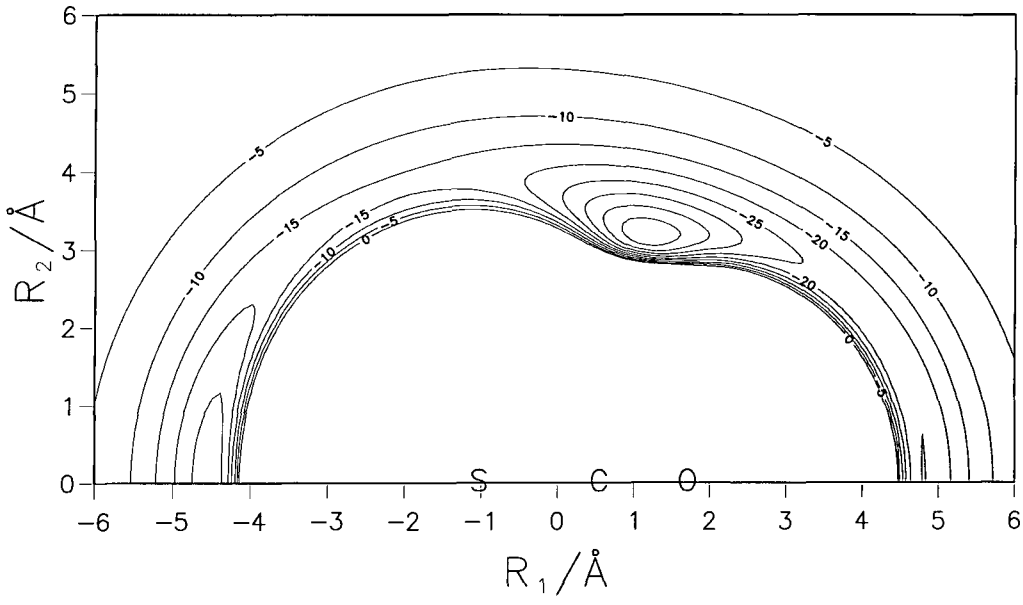

Figure 5.3: The unmorphed potential obtained from CCSD(T) calculations with aug-cc-pVTZ basis sets. Contours are labeled in cm^{-1}

A detailed comparison with the HK potential will be made in the next section.

Given that CCSD(T) computations usually underestimate the well depth, and usually have a small error in the radial co-ordinate, it is reasonable to expect that isotropic scaling in the energy, v_0 and in ξ, ρ_0 will be required. It is important to note here that sulphur has more core electrons than the other atoms in the system and therefore one would expect the greatest deficiencies in the potential to be at the sulphur end. The experimental data however samples the full range of the potential in the angular co-ordinate and so morphing will be able to correct for this deficiency.

5.4 Bound state calculations

In order to compare the rotational levels for this potential with those from experiment, coupled channel equations were solved using the BOUND program [121]. The rotational constant was taken as $b_{\mathrm{OCS}} = 0.2028567414\ \mathrm{cm}^{-1}$ [122] for $v_{\mathrm{OCS}} = 0$, with basis functions up to $j = 30$. The reduced mass of the complex was taken as $3.752158723 m_u$ and the coupled equations propagated from $R_{\mathrm{min}} = 2.2$ to $R_{\mathrm{max}} = 6.5$ Å. This gives convergence to better than 1×10^{-4} MHz for the eigenvalues and considerably better (1×10^{-9} MHz) for the rotational constants.

The BOUND program operates in Jacobi co-ordinates but this work uses elliptic co-ordinates. It is however unnecessary to alter BOUND itself to deal with elliptic co-ordinates; instead when the potential routine is called by BOUND, it calculates the equivalent position in elliptic co-ordinates before calculating the value of the potential at that point.

5.5 The Morphed Potential

A number of least-squares fits to the spectroscopic data, using the I-NoLLS program [123,124], were carried out. Recall the form of the morphing function is,

$$V_{\mathrm{morph}}(\xi,\eta) = v(\xi,\eta) V_{\mathrm{orig}}(\rho(\eta)\cdot\xi,\eta), \tag{5.2}$$

where

$$\begin{aligned} \rho(\eta) &= \sum_{\lambda} \rho_\lambda P_\lambda(\eta) \quad \text{and} \\ v(\xi,\eta) &= \sum_{\lambda} v_\lambda P_\lambda(\eta). \end{aligned} \tag{5.3}$$

Initially a two-parameter isotropic morphing with v_0 and ρ_0 was performed. While agreement with experiment was improved, see Table 5.2, the anisotropy is not accurately described. The morphed parameters are:

$$v_0 = 1.249935(.0820) \quad \rho_0 = 1.008330(.0093).$$

where the 95% confidence limits are given in parentheses. The isotropically morphed potential is plotted in Figure 5.4. Agreement with experiment in fact deteriorated, in comparison to the unmorphed potential, for transitions into the $J_{K_aK_c} = 1_{10}$ state as well as the $2_{11} \leftarrow 2_{12}$ asymmetry splitting. This was manifested in the least-squares fit as errors in D_{JK}, D_K and, to a lesser extent, in the B and C rotational constants; this implies that there was insufficient flexibility in the isotropic morphing to correctly reproduce the anisotropy. Consequently, anisotropic morphing was needed.

With the addition of just one anisotropic scaling parameter, sufficient flexibility is introduced into the morphing function that the observed rotational transitions, calculated from the potential, agree with experiment to within 7MHZ as shown in Table 5.2. The morphing parameters are:

$$\begin{aligned} v_0 &= 1.203287(.0017) \quad , \quad \rho_0 = 1.019042(.0001), \\ v_1 &= -.123042(.0006) \quad , \end{aligned}$$

with 95% confidence limits given in parentheses. From the morphing parameters alone it can be seen that the potential is approximately 16% deeper in the region of the global minimum, 8% deeper at the oxygen end and 33% deeper at the sulphur end. Globally, ξ has been decreased by approximately 2%. The potential required least adjustment at the oxygen end and greatest at the sulphur end, as was expected. A plot of the morphed potential is given in Figure 5.5.

Comparison of Figures 5.4 and 5.5, the two-parameter and three-parameter morphed surfaces, shows the effect the v_1 parameter has on the potential.

Transition	Frequency / MHz				
$J_{K_aK_c} \leftarrow J_{K_aK_c}$	Experiment	Unmorphed	Morph1	Morph2	HK Surface
$1_{10} \leftarrow 1_{11}$	1800.893	1806.301	1748.883	1799.537	1835.760
$1_{01} \leftarrow 0_{00}$	9161.812	8947.092	9068.527	9161.965	9053.461
$1_{10} \leftarrow 1_{01}$	9480.347	9445.878	9553.651	9479.605	9201.803
$2_{11} \leftarrow 2_{12}$	5386.524	5388.751	5232.120	5381.620	5485.638
$2_{11} \leftarrow 2_{02}$	11539.327	11518.781	11546.370	11537.919	11317.873
$2_{12} \leftarrow 1_{11}$	16502.643	16076.106	16371.760	16505.646	16252.516
$2_{02} \leftarrow 1_{01}$	18029.284	17585.653	17862.277	18029.415	17786.324
$2_{11} \leftarrow 1_{10}$	20088.265	19658.556	19854.997	20087.729	19902.394
$2_{21} \leftarrow 1_{10}$	42601.077	41561.181	42755.953	42607.523	41284.255
$2_{20} \leftarrow 1_{11}$	44673.734	43634.786	44759.387	44678.332	43409.832

Table 5.2: Comparison of the experimental transitions with those calculated from the unmorphed potential; the two parameter morphed surface labeled morph1; the three parameter morphed surface labeled morph2 and the HK potential.

5.5.1 Comparison of the morphed and unmorphed potentials

The general shape of the potential has been retained following the morphing procedure as can be seen from Figures 5.3 and 5.5 of the unmorphed and morphed potentials respectively. This is a fundamental feature of morphing that is also visible in the plot of the minimum energy pathway, Figure 5.6. The top graph in Figure 5.6 clearly shows the isotropic nature of the scaling in the ξ co-ordinate, as the shape of the two curves is the same.

The position and magnitude of the stationary points of both the morphed and unmorphed potentials are given in Table 5.3. The greatest difference is seen at the sulphur end where the linear minimum of the morphed potential is 9.1 cm^{-1} deeper and reduced by 0.07 in ξ compared to the unmorphed potential. The global minimum is made 7.5 cm^{-1} deeper with a reduction in the helium–OCS distance of 0.05 in ξ and 0.01 in η. The change in the transition states is less dramatic. The one closest to the oxygen end is made 2.34 cm^{-1} deeper while the one closest to the sulphur end is made 4.20 cm^{-1} deeper. At the oxygen end the smallest adjustment is seen with the morphed potential

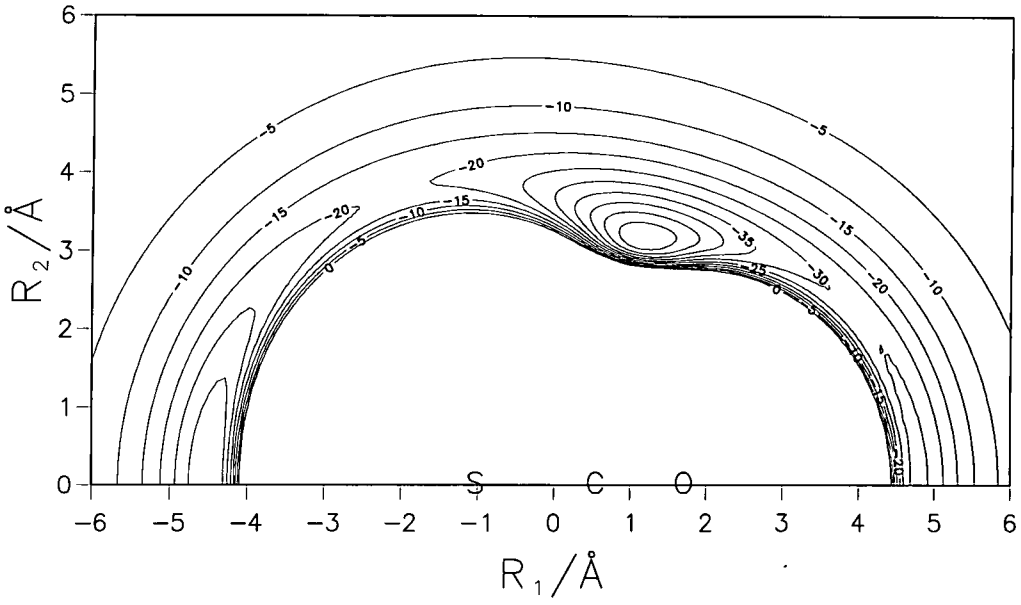

Figure 5.4: The morphed potential with $v_0 = 1.249935$ and $\rho_0 = 1.008330$. Contours are labeled in cm^{-1}

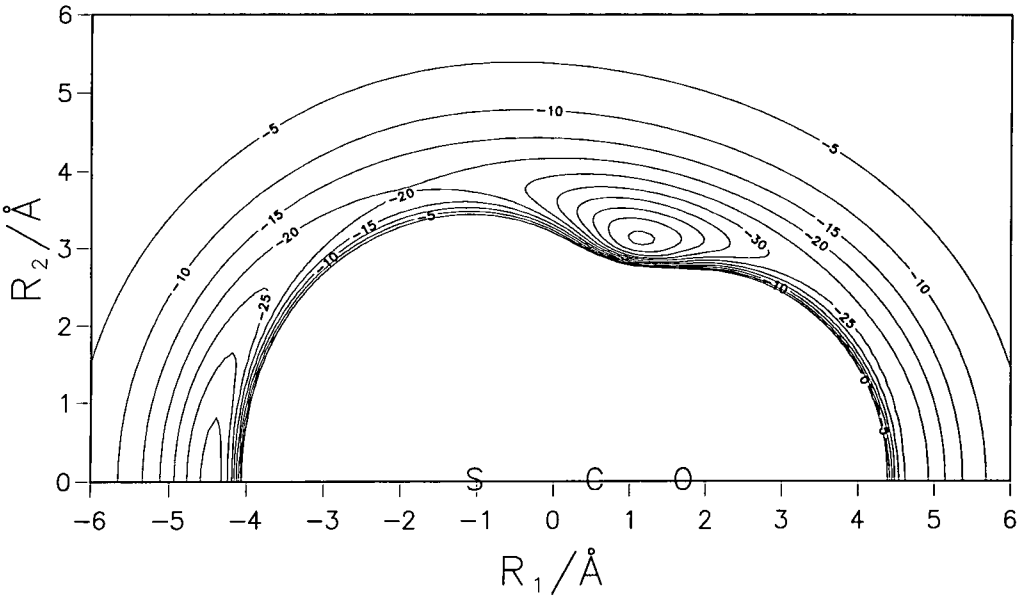

Figure 5.5: The morphed potential with $v_0 = 1.203287, v_1 = -0.123042$ and $\rho_0 = 1.019042$. Contours are labeled in cm^{-1}

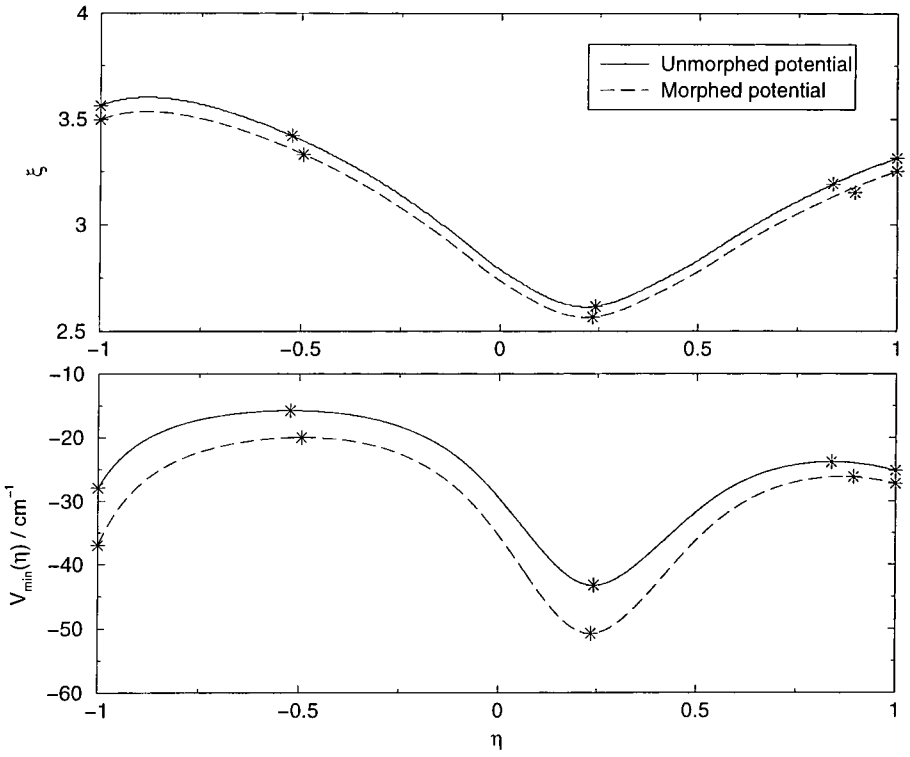

Figure 5.6: The lower graph plots the minimum energy pathway against η. The upper graph plots the values of ξ along the minimum energy pathway. The stationary points are denoted with stars.

being 2.00 cm^{-1} deeper than the unmorphed and the position of this linear minimum having been reduced by 0.06 in ξ. The potential at the oxygen end is quite flat. The difference in energy between the saddle point, separating the minimum at the oxygen end and the global minimum, and the minimum at the oxygen end of the unmorphed potential is 1.37 cm^{-1}, a feature which changes little with morphing, when the barrier became 1.05 cm^{-1}. At the sulphur end the difference is greater, 12.09 cm^{-1} prior to morphing and 17.00 cm^{-1} after.

Feature	Unmorphed potential	Morphed potential
$\epsilon(\eta = 1)$	-25.21 $(3.314, 1.000)$	-27.23 $(3.252, 1.000)$
$\epsilon(TS)$	-23.84 $(3.193, 0.839)$	-26.18 $(3.153, 0.864)$
$\epsilon(GM)$	-43.27 $(2.618, 0.241)$	-50.80 $(2.568, 0.234)$
$\epsilon(TS)$	-15.81 $(3.421, 0.524)$	-20.01 $(3.331, -0.495)$
$\epsilon(\eta = -1)$	-27.90 $(3.565, -1.000)$	-37.01 $(3.498, -1.000)$

Table 5.3: Comparison of the magnitude and position of the stationary points of the morphed potential, with $v_0 = 1.203287, v_1 = -.123042$ and $\rho_0 = 1.019042$, and the unmorphed potentials. Energies are given in cm^{-1} and the position is given in parentheses, (ξ, η). (TS = Transition state and GM = Global minimum.)

5.5.2 Comparison of the HK and morphed surfaces.

The HK surface is shallower than the morphed potential in the well region with a global minimum of -45.39 cm^{-1} at $R = 3.379$ Å, $\theta = 71.6°$, compared to -50.80 cm^{-1} at $R = 3.325$ Å, $\theta = 70.0°$. The deviation in energy is significantly larger than in the position. The discrepancy at the oxygen end is smaller with the HK potential only 0.9 cm^{-1} shallower than the morphed potential. The difference in position however is only 0.09 Å, which is a greater difference than the difference between the morphed and unmorphed potentials. The sulphur end is where the greatest discrepancy lies, with the HK having a minimum at -28.69 cm^{-1} compared to the -37.01 cm^{-1} of the morphed potential. The difference in the position of this minimum is however similar to that at the oxygen end, with $R = 4.525$ Å for the HK potential and $R = 4.432$ Å for the morphed potential. Thus the major inconsistency between the two potentials

is at the sulphur end of the molecule. Higgins and Klemperer also kept the core electrons frozen in their *ab initio* computations, which could account in part for the large difference at the sulphur end between the two potentials.

The unmorphed potential agrees more closely with six of the ten rotational transitions than the HK potential. As can be seen from Table 5.2 the morphed potential agrees more closely for all transitions than the HK potential. The greatest difference in the observed and calculated transitions for both potentials is in the $2_{21} \leftarrow 1_{10}$ transition where the difference is 6.4 MHz for the morphed potential and 1316.8 MHz for the HK potential.

5.6 Conclusions

The morphing procedure has been successfully applied to the potential energy surface of HeOCS. The unmorphed potential has closer agreement with the majority of experimentally observed transitions than the HK surface therefore the grid of points used for the *ab initio* computations appears to have been appropriate. The amount of morphing required was small compared to previously published applications of morphing [83,144] because of the high quality of the initial surface. The morphed potential reproduced the measured rotational transitions to within 7 MHz.

5.7 Additional material

A FORTRAN77 subroutine and data file are available to evaluate the HeOCS morphed potential. These can be obtained via anonymous ftp from krypton.dur.ac.uk.

CHAPTER

6

Conclusions

Potential energy surfaces were obtained for ArCO and HeOCS. The HeOCS surface was in close agreement with the available experimental data.

Two different approaches were adopted to calculating the ArCO potential. The first was the systematic model which was thought to be applicable to many systems with only small adjustments in the functional form [108]. When applied to ArCO with the functional form detailed in Chapter 2 the approach failed. The cause of the failure, although not clear, may have been an inadequate model of the dispersion energy. Therefore an alternative approach was applied, the morphing procedure developed by Meuwly and Hutson [83]. This involved calculating a supermolecular potential and then scaling it in an angle dependent way.

An initial potential energy surface for ArCO was obtained from MP4 interaction energies calculated at 77 different configurations by Shin *et al.* [67]. The surface was morphed so that improved agreement was obtained with experiment for all but the virial coefficients and the asymmetry splitting of the

$K = 1$ stretching state. The discrepancy between experimental second virial coefficients and those calculated from the morphed surface, combined with the discrepancy in the asymmetry splitting of the $(1, 0, 1, 1)$ state indicated that the unmorphed surface was of too low quality and that extra points in the θ co-ordinate were required.

The application of the morphing procedure to ArCO highlighted a key problem with the supermolecular approach to calculating potential energy surfaces. Despite supermolecular computations being used widely in the literature to calculate potentials, there is no consistently used method of distributing points in configuration space. Additionally, no systematic study into the optimum distribution of points has been performed. Therefore, in Chapter 4, the effect of the distribution of points in configuration space on the accuracy of the surface obtained was investigated. In addition to the distribution of points, it was found that both the interpolation scheme and the co-ordinate system could affect the surface obtained substantially. By employing elliptic co-ordinates the anisotropy of the potential to be interpolated could be reduced, which significantly decreased the number of points required. Expanding the potential in Legendre polynomials and interpolating between the expansion coefficients in the radial co-ordinate with RKHS required the fewest points to produce a surface of the desired accuracy.

So, when the initial HeOCS surface was calculated, the points were distributed on a regular grid in elliptic co-ordinates. The potential was then expanded in Legendre polynomials in the angular co-ordinate, while the reproducing kernel Hilbert space interpolation scheme was used for the radial. The surface only required three morphing parameters to achieve agreement with experiment. The small amount of morphing required was due to the quality of the initial surface.

The results obtained show that the morphing procedure provides a promising approach to improving *ab initio* potentials in order to obtain agreement with experiment without changing the general shape of the surface. The approach can also be used, in part, to assess the quality of the initial unmorphed surface and identify regions which are not well determined by *ab initio* computations. As long as the *ab initio* points provide satisfactory coverage of config-

uration space, the morphing procedure should be easily extendible to higher dimensions. This is a promising direction for future research.

BIBLIOGRAPHY

[1] J. M. Hutson, Ann. Rev. Phys. Chem. **41**, 123 (1990).

[2] G. Chałasiński and M. M. Szczęśniak, Chem. Rev. **94**, 1723 (1994).

[3] A. J. Stone, *The Theory of Intermolecular Forces.*, Oxford University Press, Oxford, 1996.

[4] Y. Kwon, D. M. Ceperley, and K. B. Whaley, J. Chem. Phys. **104**, 2341 (1996).

[5] G. C. Maitland, M. Rigby, E. B. Smith, and W. A. Wakeham, *Intermolecular Forces*, Clarendon Press, Oxford, 1981.

[6] R. B. Bernstein, editor, *Atom-Molecule Collision Theory*, Plenum Press, 1979.

[7] G. Scoles, editor, *Atomic and Molecular Beam Methods*, Oxford University Press, Oxford, 1988.

[8] D. J. Nesbitt, Chem. Rev. **88**, 843 (1988).

[9] K. R. Leopold, G. T. Fraser, S. E. Novick, and W. Klemperer, Chem. Rev. **94**, 1807 (1994).

[10] M. Rigby, E. B. Smith, W. A. Wakeham, and G. C. Maitland, *The forces between molecules*, Clarendon Press, Oxford, 1986.

[11] K. Vatter, H. J. Schmidt, E. Elias, and B. Schramm, Ber. Bunsenges. Phys. Chem. **100**, 73 (1996).

[12] B. Schramm, E. Elias, L. Kern, G. Natour, A. Schmitt, and C. Weber, Ber. Bunsenges. Phys. Chem. **95**, 615 (1991).

[13] H. Meyer, U. Buck, R. Schinke, and G. H. F. Diercksen, J. Chem. Phys. **84**, 4976 (1986).

[14] L. Beneventi, P. Casavecchia, F. Vecchiocattivi, G. G. Volpi, U. Buck, Ch. Lauenstein, and R. Schinke, J. Chem. Phys. **89**, 4671 (1988).

[15] L. Beneventi, P. Casavecchia, G. G. Volpi, D. Lemoine, and M. H. Alexander, J. Chem. Phys. **89**, 3505 (1988).

[16] G. D. Billing, Chem. Phys. **91**, 327 (1984).

[17] G. C. Corey, F. R. W. McCourt, and G. C. Maitland, Mol. Phys. **62**, 875 (1987).

[18] C. F. Roche, A. S. Dickinson, A. Ernesti, and J. M. Hutson, J. Chem. Phys. **107**, 1842 (1997).

[19] A. K. Dham, F. R. W. McCourt, and W. J. Meath, J. Chem. Phys. **103**, 8477 (1995).

[20] P. Casavecchia, A. Laganà, and G. G. Volpi, Chem. Phys. Lett. **112**, 445 (1984).

[21] U. Buck, I. Ettischer, S. Schlemmer, M. Yang, P. Vohralik, and R. o. Watts, J. Chem. Phys. **99**, 3494 (1993).

[22] R. Schinke, H. Meyer, U. Buck, and G. H. F. Diercksen, J. Chem. Phys. **80**, 5518 (1984).

[23] G. Ebel, R. Krohne, H. Meyer, U. Buck, R. Schinke, T. Seelemann, P. Andresen, J. Schleipen, J. J. ter Meulen, and G. H. F. Diercksen, J. Chem. Phys. **93**, 6419 (1990).

[24] G. Dharmasena, T. R. Phillips, K. N. Shokhirev, G. A. Parker, and M. Keil, J. Chem. Phys. **106**, 9950 (1997).

[25] M. Alagia, N. Balucani, L. Cartechini, P. Casavecchia, G. G. Volpi, L. A. Pederson, G. C. Schatz, G. Lendvay, L. B. Harding, T. Hollebeek, T. S. Ho, and H. Rabitz, J. Chem. Phys. **110**, 8857 (1999).

[26] W. H. Miller, Ann. Rev. Phys. Chem. **41**, 245 (1990).

[27] M. Alagia, N. Balucani, P. Casavecchia, D. Stranges, G. G. Volpi, D. C. Clary, A. Kliesch, and H. J. Werner, Chem. Phys. **207**, 389 (1996).

[28] U. Buck, Adv. Chem. Phys. **30**, 313 (1975).

[29] U. Buck, Rev. Mod. Phys. **46**, 369 (1974).

[30] M. Keil, L. J. Danielson, and P. J. Dunlop, J. Chem. Phys. **94**, 296 (1991).

[31] A. P. Kalinin, V. N. Khromov, and V. B. Leonas, Mol. Phys. **47**, 811 (1982).

[32] R. T Pack, Chem. Phys. Lett. **55**, 197 (1978).

[33] L. Beneventi, P. Casavecchia, G. G. Volpi, C. C. K. Wong, and F. R. W. McCourt, J. Chem. Phys. **98**, 7926 (1993).

[34] U. Buck, Comments At. Mol. Phys. **17**, 143 (1986).

[35] M. J. Weida, J. M. Sperhac, D. J. Nesbitt, and J. M. Hutson, J. Chem. Phys. **101**, 8351 (1994).

[36] M. Keil, L. J. Rawluk, and T. W. Dingle, J. Chem. Phys. **96**, 6621 (1992).

[37] T. G. A. Heijmen, R. Moszynski, P. E. S. Wormer, A. van der Avoird, A. D. Rudert, J. B. Halpern, J. Martin, W. B. Gao, and H. Zacharias, J. Chem. Phys. **111**, 2519 (1999).

[38] W. B. Chapman, M. J. Weida, and D. J. Nesbitt, J. Chem. Phys. **106**, 2248 (1997).

[39] R. Düren, H. Hasselbrink, and G. Hillrichs, Chem. Phys. Lett. **112**, 441 (1984).

[40] D. J. Nesbitt, J. W. Nibler, A. Schiffman, W. B. Chapman, and J. M. Hutson, J. Chem. Phys. **98**, 9513 (1993).

[41] A. Schiffman and D. W. Chandler, Int. Rev. Phys. Chem. **14**, 371 (1995).

[42] J. N. Murrell and S. D. Bosanac, *Introduction to the theory of atomic and molecular collisions*, John Wiley, Chichester, 1989.

[43] J. M. Hutson, A. Ernesti, M. M. Law, C. F. Roche, and R. J. Wheatley, J. Chem. Phys. **105**, 9130 (1996).

[44] C. F. Roche, A. S. Dickinson, A. Ernesti, and J. M. Hutson, J. Chem. Phys. **107**, 1824 (1997).

[45] T. G. A. Heijmen, T. Korona, R. Moszynski, P. E. S. Wormer, and A. van der Avoird, J. Chem. Phys. **107**, 902 (1997).

[46] T. G. A. Heijmen, R. Moszynski, P. E. S. Wormer, A. van der Avoird, U. Buck, C. Steinbach, and J. M. Hutson, J. Chem. Phys. **108**, 4849 (1998).

[47] T. G. A. Heijmen, P. E. S. Wormer, A. van der Avoird, R. E. Miller, and R. Moszynski, J. Chem. Phys. **110**, 5639 (1999).

[48] R. E. Miller, T. G. A. Heijmen, P. E. S. Wormer, A. van der Avoird, and R. Moszynski, J. Chem. Phys. **110**, 5651 (1999).

[49] S. Green, L. Monchick, R. Goldflam, and D. J. Kouri, J. Chem. Phys. **66**, 1409 (1977).

[50] S. Green, J. Chem. Phys. **88**, 7331 (1988).

[51] C. Roche, A. Ernesti, J. M. Hutson, and A. S. Dickinson, J. Chem. Phys. **104**, 2156 (1996).

[52] C. Bissonnette, C. E. Chuaqui, K. G. Crowell, R. J. LeRoy, R. J. Wheatley, and W. J. Meath, J. Chem. Phys. **105**, 2639 (1996).

[53] S. Kita, K. Noda, and H. Inouye, J. Chem. Phys. **64**, 3446 (1976).

[54] A. Kumar and W. J. Meath, Chem. Phys. **91**, 411 (1984).

[55] A. Koide, W. J. Meath, and A. R. Allnatt, J. Chem. Phys. **86**, 1222 (1982).

[56] K. Higgins and W. Klemperer, J. Chem. Phys. **110**, 1383 (1999).

[57] J. M. Hutson, J. Phys. Chem. **96**, 4237 (1992).

[58] J. M. Hutson, J. Chem. Phys. **96**, 6752 (1992).

[59] R. J. LeRoy, C. Bissonnette, T. H. Wu, A. K. Dham, and W. J. Meath, Faraday Disc. Chem. Soc. **97**, 81 (1994).

[60] A. van der Avoird, P. E. S. Wormer, and R. Moszynski, Chem. Rev. **94**, 1931 (1994).

[61] B. Jeziorski, R. Moszynski, and K. Szalewicz, Chem. Rev. **94**, 1887 (1994).

[62] S. F. Boys and F. Bernardi, Mol. Phys. **19**, 553 (1970).

[63] C. M. Lovejoy and D. J. Nesbitt, J. Chem. Phys. **93**, 5387 (1990).

[64] C. Douketis, J. M. Hutson, B. J. Orr, and G. Scoles, Mol. Phys. **52**, 763 (1984).

[65] G. D. Purvis and R. J. Bartlett, J. Chem. Phys. **76**, 1910 (1982).

[66] J. Noga and R. J. Bartlett, J. Chem. Phys. **86**, 7041 (1987).

[67] S. Shin, S. K. Shin, and F.-M. Tao, J. Chem. Phys. **104**, 183 (1996).

[68] B. K. Taylor and R. J. Hinde, J. Chem. Phys. **111**, 973 (1999).

[69] K. W. Chan, T. D. Power, J. Jai-nhuknan, and S. M. Cybulski, J. Chem. Phys. **110**, 860 (1999).

[70] K. Higgins, F.-M. Tao, and W. Klemperer, J. Chem. Phys. **109**, 3048 (1998).

[71] F. Negri, F. Ancilotto, G. Mistura, and F. Toigo, J. Chem. Phys. **111**, 6439 (1999).

[72] S. M. Cybulski, R. A. Kendall, G. Chalasinski, M. W. Severson, and M. M. Szczesniak, J. Chem. Phys. **106**, 7731 (1997).

[73] G. C. McBane and S. M. Cybulski, J. Chem. Phys. **110**, 11734 (1999).

[74] R. Moszynski, T. Korona, P. E. Wormer, and A. van der Avoird, J. Phys. Chem. A **101**, 4690 (1997).

[75] R. Moszynski, T. Korona, P. E. Wormer, and A. van der Avoird, J. Chem. Phys. **103**, 321 (1995).

[76] R. Moszynski, P. E. Wormer, B. Jeziorski, and A. van der Avoird, J. Chem. Phys. **101**, 2811 (1994).

[77] R. Moszynski, P. E. S. Wormer, and A. van der Avoird, J. Chem. Phys. **102**, 8385 (1995).

[78] S. M. Cybulski, J. Couvillion, J. Kłos, and G. Chałasiński, J. Chem. Phys. **110**, 1416 (1999).

[79] T.-S. Ho and H. Rabitz, J. Chem. Phys. **104**, 2584 (1996).

[80] D. E. Makarov and H. Metiu, J. Chem. Phys. **108**, 590 (1998).

[81] R. P. A. Bettens and M. A. Collins, J. Chem. Phys. **111**, 816 (1999).

[82] G. Yan, M. Yang, and D. Xie, Chem. Phys. Lett. **275**, 494 (1997).

[83] M. Meuwly and J. M. Hutson, J. Chem. Phys. **110**, 8388 (1999).

[84] A. De Piante, E. J. Campbell, and S. J. Buelow, Rev. Sci. Instrum. **60**, 858 (1989).

[85] T. Ogata, W. Jäger, I. Ozier, and M. C. L. Gerry, J. Chem. Phys. **98**, 9399 (1993).

[86] W. Jäger and M. C. L. Gerry, J. Chem. Phys. **102**, 3587 (1995).

[87] M. Hepp, W. Jäger, I. Pak, and G. Winnewisser, J. Mol. Spectrosc. **176**, 58 (1996).

[88] M. Hepp, R. Gendriesch, I. Pak, F. Lewen, and G. Winnewisser, J. Mol. Spectrosc. **183**, 295 (1997).

[89] M. Hepp, R. Gendriesch, I. Pak, F. Lewen, G. Winnewisser, M. Brookes, A. R. W. McKellar, J. K. G. Watson, and T. Amano, Mol. Phys. **92**, 229 (1997).

[90] A. R. W. McKellar, Y. P. Zeng, S. W. Sharpe, C. Wittig, and R. A. Beaudet, J. Mol. Spectrosc. **153**, 475 (1992).

[91] M. Havenith, G. Hilpert, M. Petri, and W. Urban, Mol. Phys. **81**, 1003 (1994).

[92] S. König, G. Hilpert, and M. Havenith, Mol. Phys. **86**, 1233 (1995).

[93] Y. Xu, S. Civis, A. R. W. McKellar, S. König, M. Haverlag, G. Hilpert, and M. Havenith, Mol. Phys. **87**, 1071 (1996).

[94] Y. Xu and A. R. W. McKellar, Mol. Phys. **88**, 859 (1996).

[95] S. König and M. Havenith, Mol. Phys. **91**, 265 (1997).

[96] J. E. Jordan, S. O. Colgate, I. Amdur, and E. A. Mason, J. Chem. Phys. **52**, 1143 (1970).

[97] P. Duggan, P. M. Sinclair, R. Berman, A. D. May, and J. R. Drummond, J. Mol. Spectrosc. **186**, 90 (1997).

[98] P. M. Sinclair, P. Duggan, R. Berman, J. R. Drummond, and A. D. May, J. Mol. Spectrosc. **191**, 258 (1998).

[99] A. E. Belikov and M. A. Smith, J. Chem. Phys. **110**, 8513 (1999).

[100] G. A. Parker and R. T Pack, J. Chem. Phys. **69**, 3268 (1978).

[101] K. Mirsky, Chem. Phys. **46**, 445 (1980).

[102] V. Castells, N. Halberstadt, S. K. Shin, R. A. Beaudet, and C. Wittig, J. Chem. Phys. **101**, 1006 (1994).

[103] G. Jansen, Chem. Phys. Lett. **223**, 377 (1994).

[104] G. Jansen, J. Chem. Phys. **223**, 377 (1994).

[105] F. A. Gianturco, F. Paesani, M. F. Laranjeira, V. Vassilenko, and M. A. Cunha, J. Chem. Phys. **110**, 7832 (1999).

[106] B. Kukawska-Tarnawska, G. Chałasinski, and K. Olszewski, J. Chem. Phys. **101**, 4964 (1994).

[107] R. J. Wheatley and S. L. Price, Mol. Phys. **71**, 1381 (1990).

[108] R. J. Wheatley, Mol. Phys. **87**, 1083 (1996).

[109] R. D. Amos, I. l. Alberts, S. J. Andrews, S. M. Colwell, N. C. Handy, D. Jayatilaka, P. J. Knowles, R. Kobayashi, N. Koga, K. E. Laidig, P. E. Maslen, C. W. Murray, J. E. Rice, J. Sanz, E. D. Simandiras, A. J. Stone, and M.-D. Su, CADPAC: Cambridge Analytical Derivatives Package, Issue 6.1,1996 .

[110] G. Chałasiński, D. J. Funk, J. Simons, and W. H. Breckenridge, J. Chem. Phys. **87**, 3569 (1987).

[111] M. J. Frisch, G. W. Trucks, H. B. Schlegel, P. M. W. Gill, B. G. Johnson, M. A. Robb, J. R. Cheeseman, T. Keith, G. A. Petersson, J. A. Montgomery, K. Raghavachari, M. A. Al-Laham, V. G. Zakrzewski, J. V. Ortiz, J. B. Foresman, J. Cioslowski, B. B. Stefanov, A. Nanayakkara, M. Challacombe, C. Y. Peng, P. Y. Ayala, W. Chen, M. W. Wong, J. L. Andres, E. S. Replogle, R. Gomperts, R. L. Martin, D. J. Fox, J. S. Binkley, D. J. Defrees, J. Baker, J. P. Stewart, M. Head-Gordon, C. Gonzalez, and J. A. Pople, *Gaussian94, Revision C.3*, Gaussian Inc., Pittsburgh PA, 1995.

[112] R. J. Wheatley, GMUL computer program, version3.0 (1995).

[113] R. J. Wheatley and J. B. O. Mitchell, J. Comput. Phys. **15**, 1187 (1994).

[114] K. M. Atkins and J. M. Hutson, J. Chem. Phys. **105**, 440 (1996).

[115] G. Maroulis, Theor. Chim. Acta **84**, 245 (1992).

[116] A. D. Buckingham, Adv. Chem. Phys. **12**, 107.

[117] K. C. Ng and W. J. Meath, Chem. Phys. **32**, 175 (1978).

[118] G. Maroulis, J. Phys. Chem. **100**, 13466 (1996).

[119] A. J. Thakkar and V. H. Smith, J. Phys. B **7**, 1321 (1974).

[120] W. J. Meath and M. Koulis, J. Mol. Spectrosc. **226**, 1 (1991).

[121] J. M. Hutson, BOUND computer program, version 6, distributed by Collaborative Computational Project No.6 of the UK Science and Engineering Research Council (1993).

[122] E. Rbaihi, A. Belafhal, J. V. Auwera, S. Naïm, and A. Fayt, J. Mol. Spectrosc. **191**, 32 (1998).

[123] M. M. Law and J. M. Hutson, I-NoLLS computer program version 1.0 (1996).

[124] M. M. Law and J. M. Hutson, Comput. Phys. Comm. **102**, 252 (1997).

[125] A. J. Stone and S. L. Price, J. Phys. Chem. **92**, 3325 (1988).

[126] J. M. Bowman and B. Gazdy, J. Chem. Phys. **94**, 816 (1991).

[127] B. Gazdy and J. M. Bowman, J. Chem. Phys. **95**, 6309 (1991).

[128] J. M. Bowman and B. Gazdy, Chem. Phys. Lett. **200**, 311 (1992).

[129] F. B. van Duijneveldt, J. G. C. M. van Duijneveldt-van de Rijdt, and J. H. van Lenthe, Chem. Rev. **94**, 1873 (1994).

[130] W. H. Press, B. P. Flannery, S. A. Teukolsky, and W. T. Vetterling, *Numerical Recipes*, Cambridge University Press, Cambridge, 1988.

[131] J. P. Toennies and A. F. Vilesov, Ann. Rev. Phys. Chem. **49**, 1 (1998).

[132] M. Hartmann, N. Prtner, B. Sartakov, J. P. Toennies, and A. F. Vilesov, J. Chem. Phys. **110**, 5109 (1999).

[133] S. Grebenev, J. P. Toennies, and A. F. Vilesov, Science **279**, 2083 (1998).

[134] A. Lindinger, J. P. Toennies, and A. F. Vilesov, J. Chem. Phys. **110**, 1429 (1999).

[135] K. Nauta and R. E. Miller, J. Chem. Phys. **111**, 3426 (1999).

[136] P. J. Dunlop and C. M. Bignell, Ber. Bunsenges. Phys. Chem. **99**, 77 (1995).

[137] M. Broquier, A. Picard-Berselini, B. J. Whitaker, and S. Green, J. Chem. Phys. **84**, 2104 (1986).

[138] L. J. Danielson, K. M. Mcleod, and M. Keil, J. Chem. Phys. **87**, 239 (1987).

[139] J. Sadlej and W. D. Edwards, International Journal of Quantum Chemistry **46**, 623 (1993).

[140] D. E. Woon and T. H. Dunning Jr., J. Chem. Phys. **100**, 2975 (1994).

[141] T. H. Dunning Jr., J. Chem. Phys. **90**, 1007 (1989).

[142] D. E. Woon and T. H. Dunning Jr., J. Chem. Phys. **98**, 1358 (1993).

[143] Basis sets were obtained from the Extensible Computational Chemistry Environment Basis Set Database, Version 1.0, as developed and distributed by the Molecular Science Computing Facility, Environmental and Molecular Sciences Laboratory which is part of the Pacific Northwest Laboratory, P.O. Box 999, Richland, Washington 99352, USA, and funded by the U.S. Department of Energy. The Pacific Northwest Laboratory is a multi-program laboratory operated by Battelle Memorial Institue for the U.S. Department of Energy under contract DE-AC06-76RLO 1830. Contact David Feller or Karen Schuchardt for further information.

[144] M. Meuwly, J. Chem. Phys. **111**, 2633 (1999).

APPENDIX

A

Conferences, Courses and Seminars Attended

Photoionisation Dynamics, Rydberg States and Large Amplitude Motion.
University of York 3rd-5th November 1996.

Optical, Electric and Magnetic properties of molecules: A conference to celebrate the career of Prof. A. D. Buckingham.
University of Cambridge. 4th-8th July 1997.

The Dynamics of Electronically-Excited States in Gaseous, Cluster and condensed media. Faraday Discussion 108.
University of Sussex. 15th-17th December 1997.

Royal Society of Chemistry High Resolution Spectroscopy Group. Conference on High Resolution Spectroscopy (Annual meeting of the HRSG).
Exeter University, 17th-19th December 1997.

Fashioning a model: Optimisation methods in chemical physics.
University of Durham. 24th-27th March 1998.

Royal Society of Chemistry 1998 National Congress and Young Researchers Meeting.
University of Durham. 6th-9th April 1998.

Spectroscopy of Radicals in Ions.
St John's College, Oxford. 7th-9th January 1999.

Rovibrational Bound States in Polyatomic Molecules.
University of Aberdeen. 11th-14th April 1999.

.....

The following is a list of the seminars in the chemistry department from 1996-1999. The ones marked with an asterisk were attended.

1996 - 1997

1996

October 9 Professor G. Bowmaker, University Aukland, NZ
Coordination and Materials Chemistry of the Group 11 and Group 12 Metals: Some Recent Vibrational and Solid State NMR Studies

October 14 Professor A. R. Katritzky, University of Gainesville, University of Florida, USA
Recent Advances in Benzotriazole Mediated Synthetic Methodology

October 16 Professor Ojima, Guggenheim Fellow, State University of New York at Stony Brook
Silylformylation and Silylcarbocyclisations in Organic Synthesis

October 22 Professor Lutz Gade, Univ. Wurzburg, Germany
Organic transformations with Early-Late Heterobimetallics: Synergism and Selectivity

October 22 * Professor B. J. Tighe, Department of Molecular Sciences and Chemistry, University of Aston
Making Polymers for Biomedical Application - can we meet Nature's Challenge?
Joint lecture with the Institute of Materials

October 23 Professor H. Ringsdorf (Perkin Centenary Lecture)
Johannes Gutenberg-Universitat, Mainz, Germany
Function Based on Organisation

October 29 * Professor D. M. Knight, Department of Philosophy, University of Durham.
The Purpose of Experiment - A Look at Davy and Faraday

October 30 Dr Phillip Mountford, Nottingham University
Recent Developments in Group IV Imido Chemistry

November 6 Dr Melinda Duer, Chemistry Department, Cambridge
Solid-state NMR Studies of Organic Solid to Liquid-crystalline Phase Transitions

November 12 * Professor R. J. Young, Manchester Materials Centre, UMIST
New Materials - Fact or Fantasy?
Joint Lecture with Zeneca & RSC

November 13 Dr G. Resnati, Milan
Perfluorinated Oxaziridines: Mild Yet Powerful Oxidising Agents

November 18 Professor G. A. Olah, University of Southern California, USA
Crossing Conventional Lines in my Chemistry of the Elements

November 19 Professor R. E. Grigg, University of Leeds
Assembly of Complex Molecules by Palladium-Catalysed Queueing Processes

November 20 Professor J. Earnshaw, Department of Physics, Belfast
Surface Light Scattering: Ripples and Relaxation

November 27 Dr Richard Templer, Imperial College, London
Molecular Tubes and Sponges

December 3 * Professor D. Phillips, Imperial College, London
"A Little Light Relief"

December 4 * Professor K. Muller-Dethlefs, York University
Chemical Applications of Very High Resolution ZEKE Photoelectron Spectroscopy

December 11 Dr Chris Richards, Cardiff University
Stereochemical Games with Metallocenes

1997

January 15 Dr V. K. Aggarwal, University of Sheffield
Sulfur Mediated Asymmetric Synthesis

January 16 Dr Sally Brooker, University of Otago, NZ
Macrocycles: Exciting yet Controlled Thiolate Coordination Chemistry

January 21 Mr D. Rudge, Zeneca Pharmaceuticals
High Speed Automation of Chemical Reactions

January 22 Dr Neil Cooley, BP Chemicals, Sunbury
Synthesis and Properties of Alternating Polyketones

January 29 Dr Julian Clarke, UMIST
What can we learn about polymers and biopolymers from computer-generated nanosecond movie-clips?

February 4 Dr A. J. Banister, University of Durham
From Runways to Non-metallic Metals - A New Chemistry Based on Sulphur

February 5 Dr A. Haynes, University of Sheffield
Mechanism in Homogeneous Catalytic Carbonylation

February 12 Dr Geert-Jan Boons, University of Birmingham
New Developments in Carbohydrate Chemistry

February 18 * Professor Sir James Black, Foundation/King's College London
My Dialogues with Medicinal Chemists

February 19 Professor Brian Hayden, University of Southampton
The Dynamics of Dissociation at Surfaces and Fuel Cell Catalysts

February 25 Professor A. G. Sykes, University of Newcastle
The Synthesis, Structures and Properties of Blue Copper Proteins

February 26 Dr Tony Ryan, UMIST
Making Hairpins from Rings and Chains

March 4 Professor C. W. Rees, Imperial College
Some Very Heterocyclic Chemistry

March 5 Dr J. Staunton FRS, Cambridge University
Tinkering with biosynthesis: towards a new generation of antibiotics

March 11 * Dr A. D. Taylor, ISIS Facility, Rutherford Appleton Laboratory
Expanding the Frontiers of Neutron Scattering

March 19 * Dr Katharine Reid, University of Nottingham
Probing Dynamical Processes with Photoelectrons

1997 - 1998

1997

October 8 Prof. E. Atkins, Department of Physics, University of Bristol
Advances in the control of architecture for polyamides: from nylons to genetically engineered silks to monodisperse oligoamides

October 15 Dr. R. Mark Ormerod, Department of Chemistry, Keele University
Studying catalysts in action

October 21 Prof. A. F. Johnson, IRC, Leeds
Reactive processing of polymers: science and technology

October 22 Prof. R.J. Puddephatt (RSC Endowed Lecture),
University of Western Ontario
Organoplatinum chemistry and catalysis

October 23 Prof. M.R. Bryce, University of Durham, Inaugural Lecture
New Tetrathiafulvalene Derivatives in Molecular, Supramolecular and Macromolecular Chemistry: controlling the electronic properties of organic solids

October 29 Prof. Bob Peacock, University of Glasgow
Probing chirality with circular dichroism

October 28 Prof. A P de Silva, The Queen's University, Belfast
Luminescent signalling systems

November 5 * Dr Mimi Hii, Oxford University
Studies of the Heck reaction

November 11 Prof. V Gibson, Imperial College, London
Metallocene polymerisation

November 12 * Dr Jeremy Frey, Department of Chemistry, Southampton University
Spectroscopy of liquid interfaces: from bio-organic chemistry to atmospheric chemistry

November 19 Dr Gareth Morris, Department of Chemistry, Manchester Univ.
Pulsed field gradient NMR techniques: Good news for the Lazy and DOSY

November 20 Dr Leone Spiccia, Monash University, Melbourne, Australia
Polynuclear metal complexes

November 25 Dr R. Withnall, University of Greenwich
Illuminated molecules and manuscripts

November 26 * Prof. R.W. Richards, University of Durham, Inaugural Lecture
A random walk in polymer science

December 2 Dr C.J. Ludman, University of Durham
Explosions

December 3 Prof. A.P. Davis, Department. of Chemistry,
Trinity College Dublin.
Steroid-based frameworks for supramolecular chemistry

December 10 * Sir Gordon Higginson, former Professor of Engineering in Durham and retired Vice-Chancellor of Southampton Univ.
1981 and all that.

December 10 Prof. Mike Page, Department of Chemistry, University of Huddersfield
The mechanism and inhibition of beta-lactamases

1998

January 14 * Prof. David Andrews, University of East Anglia
Energy transfer and optical harmonics in molecular systems

January 20 Prof. J. Brooke, University of Lancaster
What's in a formula? Some chemical controversies of the 19th century

January 21 Prof. David Cardin, University of Reading

January 27 Prof. Richard Jordan, Dept. of Chemistry, Univ. of Iowa, USA.
Cationic transition metal and main group metal alkyl complexes in olefin polymerisation

January 28 * Dr Steve Rannard, Courtaulds Coatings (Coventry)
The synthesis of dendrimers using highly selective chemical reactions

February 3 Dr J. Beacham, ICI Technology
The chemical industry in the 21st century

February 4 * Prof. P. Fowler, Department of Chemistry, Exeter University
Classical and non-classical fullerenes

February 11 Prof. J. Murphy, Dept of Chemistry, Strathclyde University

February 17 Dr S. Topham, ICI Chemicals and Polymers
Perception of environmental risk; The River Tees, two different rivers

February 18 * Prof. Gus Hancock, Oxford University
Surprises in the photochemistry of tropospheric ozone

February 24 Prof. R. Ramage, University of Edinburgh
The synthesis and folding of proteins

February 25 Dr C. Jones, Swansea University
Low coordination arsenic and antimony chemistry

March 4 Prof. T.C.B. McLeish, IRC of Polymer Science Technology, Leeds University

The polymer physics of pyjama bottoms (or the novel rheological characterisation of long branching in entangled macromolecules)

March 11 Prof. M.J. Cook, Dept of Chemistry, UEA

How to make phthalocyanine films and what to do with them.

March 17 Prof. V. Rotello, University of Massachusetts, Amherst

The interplay of recognition & redox processes - from flavoenzymes to devices

March 18 Dr John Evans, Oxford University

Materials which contract on heating (from shrinking ceramics to bullet proof vests).

1998 - 1999

1998

October 7 Dr S Rimmer, Ctr Polymer, University of Lancaster

New Polymer Colloids

October 9 * Professor M F Hawthorne, Department Chemistry & Biochemistry, UCLA, USA

RSC Endowed Lecture

October 21 * Professor P Unwin, Department of Chemistry, Warwick University

Dynamic Electrochemistry: Small is Beautiful

October 23 * Professor J C Scaiano, Department of Chemistry, University of Ottawa, Canada

In Search of Hypervalent Free Radicals, RSC Endowed Lecture

October 26 Dr W Peirs, University of Calgary, Alberta, Canada

Reactions of the Highly Electrophilic Boranes HB(C6F5)2 and B(C6F5)3 with Zirconium and Tantalum Based Metallocenes

October 27 Professor A Unsworth, University of Durham
What's a joint like this doing in a nice girl like you? In association with The North East Polymer Association

October 28 * Professor J P S Badyal, Department of Chemistry, University of Durham
Tailoring Solid Surfaces, Inaugural Lecture

November 4 * Dr N Kaltscoyannis, Department of Chemistry, UCL, London
Computational Adventures in d & f Element Chemistry

November 3 Dr C J Ludman, Chemistry Department, University of Durham
Bonfire night Lecture

November 10 Dr J S O Evans, Chemistry Department, University of Durham
Shrinking Materials

November 11 Dr M Wills, Department of Chemistry, University of Warwick
New Methodology for the Asymmetric Transfer Hydrogen of Ketones

November 12 Professor S Loeb, University of Windsor, Ontario, Canada
From Macrocycles to Metallo-Supramolecular Chemistry

November 17 Dr J McFarlane UNIVERSITY ??
Nothing but Sex and Sudden Death!

November 18 * Dr R Cameron, Department of Materials Science & Metallurgy, Cambridge University
Biodegradable Polymers

November 24 Dr B G Davis, Department of Chemistry, University of Durham
Sugars and Enzymes

December 1 Professor N Billingham, University of Sussex
Plastics in the Environment - Boon or Bane In association with The North East Polymer Association.

December 2 * Dr M Jaspers, Department of Chemistry, University of Aberdeen
Bioactive Compounds Isolated from Marine Inverterates and Cyanobacteria

December 9 * Dr M Smith Department. of Chemistry, Warwick University
Multinuclear solid-state magnetic resonance studies of nanocrystalline oxides and glasses

1999

January 19 Dr J Mann, University of Reading
The Elusive Magic Bullet and Attempts to find it?

January 20 Dr A Jones, Department of Chemistry, University of Edinburgh
Luminescence of Large Molecules: from Conducting Polymers to Coral Reefs

January 27 Professor K Wade, Department of Chemistry, University of Durham
Foresight or Hindsight? Some Borane Lessons and Loose Ends

February 3 Dr C Schofield, University of Oxford
Studies on the Stereoelectronics of Enzyme Catalysis

February 9 Professor D J Cole-Hamilton, St. Andrews University
Chemistry and the Future of life on Earth

February 10 Dr C Bain, University of Oxford
Surfactant Adsorption and Marangoni Flow at Expanding Liquid Surfaces

February 17 Dr B Horrocks, Department of Chemistry, Newcastle University
Microelectrode techniques for the Study of Enzymes and Nucleic Acids at Interfaces

February 23 Dr C Viney, Heriot-Watt
Spiders, Slugs And Mutant Bugs

February 24 Dr. A-K Duhme, University of York
Bioinorganic Aspects of Molybdenum Transport in Nitrogen-Fixing Bacteria

March 3 Professor B Gilbert, Department of Chemistry, University of York
Biomolecular Damage by Free Radicals: New Insights through ESR Spectroscopy

March 9 Dr Michael Warhurst, Chemical Policy issues, Friends of the Earth
Is the Chemical Industry Sustainable?

March 10 Dr A Harrison, Department of Chemistry, The University of Edinburgh

Designing model magnetic materials

March 17 Dr J Robertson, University of Oxford

Recent Developments in the Synthesis of Heterocyclic Natural Products

May 11 Dr John Sodeau, University of East Anglia

Ozone Holes and Ozone Hills

May 12 Dr Duncan Bruce, Exeter University

The Synthesis and Characterisation of Liquid-Crystalline Transition Metal Complexes